Transceive Phase Corrected Contrast Source Inversion-Electrical Properties Tomography

Peter R.S. Stijnman

20^{th} of July 2017


TU Delft


UMC Utrecht

Abstract

Electrical properties tomography is the quantification of the conductivity and permittivity of different materials. In an MRI setting this can be used to map the electrical properties of tissue. These values can be used as a different contrast mechanism, for hyperthermia treatment or the improvement of antenna design for specific applications. There are different methods used to obtain these electrical properties, however these often use differential operators on measured data. This leads to reconstructions corrupted by noise, thus in this thesis the work on contrast source inversion based electrical properties tomography is continued. This method uses an integral approach and is therefore more robust with respect to noise.

The work presented continues from the two-dimensional Matlab based simulations and extends these to a more realistic measurement setup. The RF-shield is numerically implemented and an extension is made to the existing algorithm to handle the transceive phase based on Maxwell's equations. This is done by implementing a forward problem into the inverse problem of getting the contrast from the measured radiofrequency field. After this the algorithm was tested with three-dimensional FDTD simulations and finally a phantom study was done to test with an MRI scanner.

From the results of the two-dimensional simulations it was seen that this method is indeed very robust when it comes to a realistic measurement setup. In the three-dimensional simulations it was observed that the electrical properties are underestimated. Nonetheless CSI-EPT is more precise than the standard Helmholtz based methods. Plus the improvement made to the algorithm makes it possible to map all the RF fields inside the scanner which has not been done before. The same underestimation was seen with the reconstruction of the measured data from the phantom study.

Preface

This master thesis ,titled "Transceive Phase Corrected Contrast Source Inversion-Electrical Properties Tomography", is an extension of the research done on Contrast Source Inversion-Electrical Properties Tomography. In this work a realistic eye is kept on the implementation of this algorithm. It tries to identify the problems at hand and solve them accordingly. The thesis has been written to fulfill the master graduation requirements of the TU Delft. I worked on this thesis from October 2016 till July 2017.
The project was a collaboration between TU Delft and the UMC in Utrecht under the supervision of R.F. Remis and C.A.T. van den Berg. With the before mentioned supervisors we set the goal for this project to show the first experimental results of the CSI-EPT algorithm. Which was a difficult goal but was managed to be accomplished.
For this work I have a lot of people to thank, starting with R.F. Remis for giving me the chance to work on this interesting subject and for excellent guidance along the way. Next I would like to thank C.A.T. van den Berg for allowing me to work in the UMC in Utrecht, for always taking to time to give feedback on my ideas and to push my understanding of the subject.
Further I would like to thank S.Mandija who helped a tremendous amount by always being there as a sparring partner for ideas and for helping me make scanning on the MRI possible. Next a big thanks to P. Fuchs for helping me get started on the project in the best possible way and for always having his door open to ask for advice.
I would like to thank all the people in the EPT-community in Utrecht and Leiden as well for exchanging ideas and giving insight on the subject, and my colleagues at TU Delft and UMC Utrecht for keeping a fun working environment. A final thanks goes out to my family and friends for also keeping my mind of work sometimes and for their kind and inspiring words, you kept me motivated to complete this work.

Hopefully you will enjoy reading this.

Peter Stijnman.

Delft, June 16, 2017.

Contents

Nomenclature

- $\bar{E}$ denotes the mean of $\vec{E}$
- $\tilde{E}$ is a corrupted version of $\vec{E}$
- E^* is the complex conjugate of $\vec{E}$
- $G^\dagger\{\cdot\}$ is the adjoint of $G\{\cdot\}$
- μ is the magnetic permeability given by $\mu_0\mu_r$. For biological tissue $\mu_r \approx 1$.
- ϵ is the permittivity given by $\epsilon_0\epsilon_r$
- σ is the conductivity
- c_0 is the speed of light in vacuum
- $< u, v >_V = \Re \int u \cdot v^* dV$ is the definition of the inner product.
- The time convention is defined as $\vec{E}(\vec{r}, t) = \Re(\vec{E}(\vec{r})e^{j\omega t})$

1 Introduction

This work is started with a small introduction to magnetic resonance imaging (MRI). An MRI scanner consists of a strong superconducting magnet which is in the order of a few tesla. The most common strength types right now are 1.5T, 3T and 7T. The first two are most often used for diagnostic purposes whereas 7T is mostly used for research right now [1].
When an object is not in presence of a magnet the orientation of the magnetic moment of the protons is random. When this same object is put inside the scanner the magnetic moments are subject to a torque which is dependent on the strength of the magnet and the magnetic moment [2]. This torque will orient the magnetic moments to align with the static magnetic field. If the strength of the magnet increases more protons will align with the magnetic field. Now the orientation of these magnetic moments have a certain expected value (i.e. the direction of the static magnetic field), this is called the net magnetic vector (NMV).
Further it is known that protons have a spin angular momentum as well, the torque that is applied by the magnet will make the protons precess around the direction of the static magnetic field. This precession is done at a certain frequency called the Larmor frequency, this frequency is defined as

$$f_{Larmor} = \gamma B_0, \tag{1.0.1}$$

where γ is the gyromagnetic ratio and B_0 is the magnetic field strength. This ratio depends on the type of atom for which the proton is in. Since most of the signal in biological tissue comes from the hydrogen atoms, γ is taken to be 42.58 MHzT^{-1}. However, there are also other atoms used for imaging purposes in MRI, an example of this is phosphorous which has a gyromagnetic ratio of 17.235MHzT^{-1} [1].
Before the next part is discussed a distinction has to be made between the magnetization in the direction of the static magnetic field and that perpendicular to it. Magnetization in the direction of the static magnetic field is called the longitudinal magnetization whereas the magnetization perpendicular to it is called the transverse magnetization. Creating transverse magnetization is done by applying energy to the protons by means of a magnetic field which is perpendicular to the static magnetic field. This results in the NMV to move out of its equilibrium. When this perpendicular magnetic field is turned off the NMV returns to its equilibrium state again. The time it takes for the NMV to return to its equilibrium is characterized by the T1 and T2 time, where the T1 time is called the spin-lattice relaxation time and characterizes the time it takes for the NMV to return to its equilibrium longitudinal magnetization. The T2 time is the spin-spin relaxation time and characterizes the decay in transverse magnetization to zero. Different tissue types have different T1 and T2 times, this can be used to make T1 and T2 weighted images. Note that it says weighted images because the measured T1 times will always be affected by T2 and vice versa.
As mentioned before, in order to create transverse magnetization energy has to be applied to the protons. This is done by applying another magnetic field which is perpendicular to the static magnetic field, this is also called the radio frequency (RF) field. The component that is used for this is a coil. These coils come in a multitude of different shapes, sizes, and topologies [3]. Most common for whole body MRI scanners is the birdcage coil. An example of such a coil is shown in Figure 1.

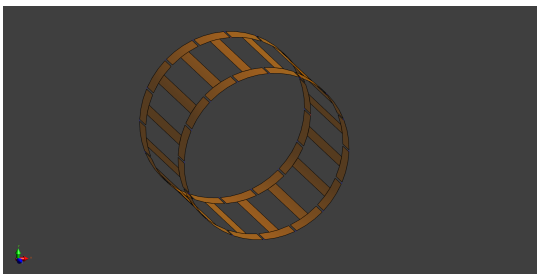

Figure 1: A highpass birdcage coil

This type of coil consists of 2 rings or endrings and a certain amount of legs or rungs. The most common birdcage coil has 16 legs/rungs. Since this is a coil it has a certain distributed inductance, which results in a certain frequency response. This frequency response shows that the coil has certain resonant modes, at these points the transfer function peaks. One of these resonant modes has a favorable characteristic, the current that runs through the legs is phase shifted by $\frac{360^\circ}{n_{legs}}$, where n_{legs} is the number of legs/rungs. This creates a circularly polarized RF-field (i.e. the magnitude of the real and imaginary components of the field are equal and the inproduct between them is zero), more on this will be discussed in Section 2.1.
Turning the birdcage coil on and off is done by the use of an RF-pulse. In order to excite the protons (i.e. get the energy from the coil to the protons) this pulse must have the same frequency as the precession of the protons, the Larmor frequency. To get this combined with the correct resonant mode of the coil, the frequency

response of the coil must be changed. This desired resonant mode must also be at the Larmor frequency. This is done by tuning the coil with capacitors to get a different frequency response. When this is accomplished the protons are excited by the RF-pulse and the precession of the transverse magnetization can be measured. The signal that is measured in MRI is an induced voltage. This voltage is induced in the measuring coil by the changing magnetization. This can either be the same birdcage coil or a separate coil used for receiving only.

1.1 Electrical Properties Tomography

In 1991 Haacke proposed a way to get electrical properties of tissue by measuring the B_1^+ field (i.e. this is part of the RF-field) [4]. This gave rise to magnetic resonance based Electrical Properties Tomography (EPT). EPT is a collective name for multiple methods involving the reconstruction of the conductivity (σ) and the permittivity (ϵ) of biological tissues. This was the first non-invasive way of measuring them. Before this the only way to measure the conductivity and permittivity was by means of electrodes and probes, which can be destructive for the tissue especially at higher frequencies. Since this publication a lot of research has been done on the subject with new methods arising constantly.
There are multiple reasons why these two characteristics of tissue are very important. The first would be the Specific Absorption Rate (SAR) which is the amount of energy absorbed by a mass, its unit is Wkg^{-1}. The higher the quantity of energy absorbed by tissue the warmer it gets. There are safety regulations on the SAR limit, which is 10 Wkg^{-1}. It is therefore important to be able to measure the SAR distribution during an MRI scan, for both the safety of the patient and the efficiency of the scan. Because if more power can used for a scan the quality of the scan increases.
Another application of knowing the SAR distribution can be hyperthermia treatment planning. Hyperthermia treatment is the heating of tissues in order to destroy it. The temperatures can range anywhere from 40 to 43 °C [5]. With knowing the electrical properties of tissue, both for healthy and unhealthy, a better treatment can be given to patients (i.e. more healthy tissue can be saved or unhealthy tissue can be heated more for more effect). Furthermore the RF-fields produced during a scan are of importance to the insight of the MRI scanner. Knowing the RF fields enables for better design of the coils and antennas used for scanning.

1.2 Current EPT methods

There are multiple methods developed to reconstruct these electrical properties. The most well known method is taking a double derivative of the of the measured B_1^+ (also known as Helmholtz based EPT). More recently methods were introduced that only use a first order derivative, gradient EPT [6] and first order induced current EPT [7]. And even certain workarounds that showed good results have been proposed. These include water EPT and sodium EPT, where the respectively water and sodium concentrations are measured and linked to conductivity values.
The advantage of these approaches is the simplicity of the calculations that are done in order to get a reconstruction. However, the derivative operators that are used in these methods are not robust with respect to noise. The signal-to-noise ratio (SNR) needed to get good results is not feasible with the MRI. Furthermore Helmholtz based EPT assumes a piece-wise homogeneous contrast [8]. Of course this is definitely not the case when scanning patients, sadly these tend to be very inhomogeneous. And then there is the problem that the derivative has to be implemented with a certain kernel which only increases the amount of errors within the reconstruction. These different problems have been addressed in [9].
For this work the method that is used is called Contrast Source Inversion (CSI). This method was shown by Van Den Berg and Kleinman in [10], later a multiplicative regularization was added to this method to handle noisy input data better [11]. Instead of a derivative approach this is an integral approach. This generalized method was rewritten for MRI data by Balidemaj *et al* in [12]. This method is discussed in detail on how it works and all the equations related to it in Section 3. The reason to choose this method over others is that it is more robust with handling noisy input data. Plus this method does not assume piece-wise homogeneous contrast. A disadvantage however is that the reconstruction process is more complex considering the calculations needed.

1.3 Challenges with CSI-EPT

One of the biggest problems with all of these methods is still not discussed. This is that they are based on having the complex B_1^+ field, this includes both amplitude and phase. Now the amplitude is not a problem, this part of the field can be measured by the MRI with a multitude of sequences these include Actual Flip-Angle Imaging (AFI) [13], Bloch-Siegert shift [14], double-angle and Dual Refocusing Echo Acquisition Mode (DREAM)[15] just to name a few. The problem here is that the phase cannot explicitly be measured, what is

actually measured is what is called the transceive phase. This is explained in Section 2.5. This problem is of key importance before these methods can be implemented in vivo, especially for higher magnetic field strengths. Further CSI-EPT has only been tested with simulations in Matlab for noisy input data and not yet been demonstrated in vivo [12]. The RF-shield present in the MRI scanner has not been taken into account in the CSI-EPT method. A finite element method to implement the RF-shield is presented in [16]. However, the approach that is used increases the computation time drastically. Therefore a numerical implementation of the RF-shield is looked into.

1.4 Research question

The main purpose of this work is to investigate if CSI-EPT can be used for in vivo measured data.
To achieve this first the effect of a numerically implemented RF-shield needs to be tested. Afterwards the CSI-EPT scheme needs to be rewritten to include the transceive phase. Further the algorithm should be tested on 3D data to get the most realistic simulation possible. Finally a phantom study should be done to get the in vivo data.
The second purpose of this work is to see if CSI-EPT shows improvement compared to the standard EPT methods.
In chapter 2 the background knowledge needed for understanding the MRI and algorithm better is given. Afterwards all the details on the CSI-EPT algorithm are given as well as the improvement made to it for MRI data. Then results are shown for different scenarios and different simulation programs. This is done to identify where certain errors come from. The next logical part is of course the measurements done with the MRI scanner and their outcomes. This is followed by a conclusion in chapter 7. Finally there is the proposed future research topics.

2 Background Knowledge

In this chapter of the thesis some information that is needed for the rest of the work is given. First the RF-fields present inside the MRI are defined. After this the groundwork for the algorithm is presented, followed by a numerical implementation for the RF-shield. Further, the SNR in an MRI experiment is discussed and the transceive phase assumption is explained.

2.1 Electromagnetics in MRI

As mentioned in the subsection above, the protons precess around the static magnetic field. When defining this in a static frame the components of the magnetization are rotating. This frame is called the laboratory frame [2]. The magnetic field given in this frame within an MRI is given by

$$\vec{B}(r,t) = B_1(r,t) \cdot \vec{X} + B_1(r,t) \cdot \vec{Y} + B_0(r) \cdot \vec{Z}. \tag{2.1.1}$$

A frame that is used more often is the rotating reference frame. When this frame is defined to rotate at the Larmor frequency the precession of the protons are static in the frame. The unit vectors from the laboratory frame, $\vec{X}$ and $\vec{Y}$, become

$$\begin{aligned} \vec{X}' &= \cos(\omega_{Larmor} t) \cdot \vec{X} + \sin(\omega_{Larmor} t) \cdot \vec{Y}, \\ \vec{Y}' &= -\sin(\omega_{Larmor} t) \cdot \vec{X} + \cos(\omega_{Larmor} t) \cdot \vec{Y}. \end{aligned} \tag{2.1.2}$$

This makes the vector calculus easier, Equation (2.1.1) can now be rewritten as

$$\vec{B}(r) = B_1(r) \cdot \vec{X}' + B_1(r) \cdot \vec{Y}' + B_0(r) \cdot \vec{Z}, \tag{2.1.3}$$

here $B_0(r)$ defines the static magnetic field and $B_1(r,t)$ is the magnetic field due to the RF-pulse. The B_1 component of the magnetic field can be disentangled into a field that rotates in clockwise and counterclockwise direction. One of these fields excites the proton spins, this field is called the B_1^+ field. The other field does not excite the spins and is called the B_1^- field. The B_1^+ field is also called the transmit field and dictates the transmit efficiency whereas the B_1^- field is called the receive field and dictates the receive sensitivity.
When transmitting in quadrature mode in a birdcage coil the two sources/ports are set to have a phase shift of 90° with respect to each other [3]. This is done to maximize the B_1^+ field and thus maximize the amount of proton spins that are flipped.
When receiving in quadrature mode the phase shift is set to $-90°$ to maximize the B_1^- field. This results in two sets of fields

$$\begin{aligned} Transmitting &= \{B_1^{+TR}, B_1^{-TR}, E^{TR}\}, \\ Receiving &= \{B_1^{+RE}, B_1^{-RE}, E^{RE}\}. \end{aligned} \tag{2.1.4}$$

For both the B_1^+ fields

$$B_1^+ = \frac{B_1(r,t) \cdot \vec{X} + jB_1(r,t) \cdot \vec{Y}}{2} = \frac{B_x + jB_y}{2}, \tag{2.1.5}$$

holds. Here $B_x = B_1(r) \cdot \vec{X}'$ and $B_y = B_1(r) \cdot \vec{Y}'$. For both the B_1^- fields

$$B_1^- = \frac{(B_1(r,t) \cdot \vec{X} - jB_1(r,t) \cdot \vec{Y})^*}{2} = \frac{(B_x - jB_y)^*}{2}, \tag{2.1.6}$$

holds.

2.2 2D scattering formalism

Most of the background information is a summary from [17].
Naturally the electromagnetic fields inside the MRI are three-dimensional, however if the midplane is taken of the birdcage coil the field can be seen as two-dimensional and E-polarized in the z-direction. This means that

$$\begin{aligned} \{B_z, E_x, E_y\} &= 0, \\ \{B_x, B_y, E_z\} &\neq 0, \end{aligned} \tag{2.2.1}$$

is true. This assumption does not hold anymore when the region of interest is not in the midplane anymore. Then a fully 3D scattering problem needs to be solved. But since in the scanner the region of interest can be placed in the middle of the birdcage coil automatically this should not pose a problem.
The two-dimensional formalism starts with the Maxwell equations

$$\begin{aligned} -\partial_x B_y + \partial_y B_x + \mu_0 J_z^{ind} &= 0, \\ \partial_y E_z + j\omega B_x &= 0, \\ -\partial_x E_z + j\omega B_y &= 0, \end{aligned} \tag{2.2.2}$$

where J_z^{ind}, the induced electric current density, is given by

$$J_z^{ind} = (\sigma + j\omega\epsilon)E_z. \tag{2.2.3}$$

The scattering formalism starts with the idea that one can write the total field as an incident field plus a scattered field due to an object. For two-dimensional electromagnetic waves this results in

$$\begin{aligned} E_z &= E_z^i + E_z^{sc}, \\ B_1^+ &= B_1^{+i} + B_1^{+sc}, \\ B_1^- &= B_1^{-i} + B_1^{-sc}, \end{aligned} \tag{2.2.4}$$

here the incident fields are the fields present due to the source when there is no object in the MRI. The scattered fields are a result of the interaction between the incident fields and the object in the MRI. This means that for a certain type of scanner the incident fields will always be the same, but the scattered fields will not.
Now combining Equation (2.2.2) and Equation (2.2.4) results in a set of Maxwell equations for the incident fields

$$\begin{aligned} -\partial_x B_y^i + \partial_y B_x^i + j\omega\epsilon_0\mu_0 E_z^i &= -\mu_0 J_z^{ext}, \\ \partial_y E_z^i + j\omega B_x^i &= 0, \\ -\partial_x E_z^i + j\omega B_y^i &= 0. \end{aligned} \tag{2.2.5}$$

The first step now is to multiply the first equation of (2.2.5) with $j\omega$ and substitute in the other two equations to obtain

$$\begin{aligned} -\partial_x(j\omega B_y^i) + \partial_y(j\omega B_x^i) - \omega^2\epsilon_0\mu_0 E_z^i &= -j\omega\mu_0 J_z^{ext}, \\ -\partial_x^2(E_z^i) - \partial_y^2(E_z^i) - \omega^2\epsilon_0\mu_0 E_z^i &= -j\omega\mu_0 J_z^{ext}, \\ (\partial_x^2 + \partial_y^2 + k_0^2)E_z^i &= j\omega\mu_0 J_z^{ext}, \end{aligned} \tag{2.2.6}$$

here k_0 is the wavenumber of the background given by

$$k_0 = \frac{\omega}{c_0} = \omega\sqrt{\epsilon_0\mu_0}. \tag{2.2.7}$$

To solve the result of Equation (2.2.6) the Green's function, $\hat{G}$, is needed. This function is the impulse response of a differential equation introduced as

$$(\partial_x^2 + \partial_y^2 + k_0^2)\hat{G} = -\delta(\rho), \tag{2.2.8}$$

here ρ is the position vector in the transverse xy-plane. In two-dimensional wave equations the Green's function is given by

$$\hat{G}(\rho) = -\frac{j}{4}H_0^{(2)}(k_0|\rho|), \tag{2.2.9}$$

where $H_0^{(2)}(\cdot)$ is the zero ordered Hankel function of the second kind. Now the incident field is given by

$$E_z^i = -j\omega\mu_0 \int_{\rho' \in \mathbb{D}^{src}} \hat{G}(\rho - \rho')J_z^{ext}(\rho')dV, \tag{2.2.10}$$

here ρ' is the location of the source and $\mathbb{D}^{src}$ is the source domain. The incident fields for an MRI will be discussed further on in this chapter. First the scattered fields will be given to complete the set of equations for

the two-dimensional fields.
The field distributions inside the object are given by the following set of equations

$$\begin{aligned} -\partial_x B_y + \partial_y B_x + \mu_0(\sigma + j\omega\epsilon)E_z &= 0, \\ \partial_y E_z + j\omega B_x &= 0, \\ -\partial_x E_z + j\omega B_y &= 0. \end{aligned} \tag{2.2.11}$$

The first of Equation (2.2.11) can be rewritten as

$$-\partial_x B_y + \partial_y B_x + j\omega\epsilon_0\mu_0 E_z = -\mu_0(\sigma + j\omega\epsilon - j\omega\epsilon_0)E_z. \tag{2.2.12}$$

From this the contrast function can be introduced

$$\chi(\rho) = \sigma(\rho) + j\omega\epsilon(\rho) - j\omega\epsilon_0 = \epsilon_r(\rho) - 1 + \frac{\sigma(\rho)}{j\omega\epsilon_0}, \quad \rho \in \mathbb{D}. \tag{2.2.13}$$

Further there are the field distributions outside the object, the contrast outside the object is air which is characterized by $\sigma = 0$ and $\epsilon = \epsilon_0$, which are given by

$$\begin{aligned} -\partial_x B_y + \partial_y B_x + j\omega\epsilon_0\mu_0 E_z &= -J_z^{ext}, \\ \partial_y E_z + j\omega B_x &= 0, \\ -\partial_x E_z + j\omega B_y &= 0. \end{aligned} \tag{2.2.14}$$

To get the scattered fields from Equation (2.2.11) and Equation (2.2.14) all that needs to be done is subtracting the incident fields given in Equation (2.2.5). This results in a set of equations for the scattered fields inside and outside the object

$$\begin{aligned} -\partial_x B_y^{sc} + \partial_y B_x^{sc} + j\omega\epsilon_0\mu_0 E_z^{sc} &= -j\omega\epsilon_0\mu_0\chi E_z, \\ \partial_y E_z^{sc} + j\omega B_x^{sc} &= 0, \\ -\partial_x E_z^{sc} + j\omega B_y^{sc} &= 0, \end{aligned} \tag{2.2.15}$$

and

$$\begin{aligned} -\partial_x B_y^{sc} + \partial_y B_x^{sc} + j\omega\epsilon_0\mu_0 E_z^{sc} &= 0, \\ \partial_y E_z^{sc} + j\omega B_x^{sc} &= 0, \\ -\partial_x E_z^{sc} + j\omega B_y^{sc} &= 0. \end{aligned} \tag{2.2.16}$$

These two sets of equations can be combined into one

$$\begin{aligned} -\partial_x B_y^{sc} + \partial_y B_x^{sc} + j\omega\epsilon_0\mu_0 E_z^{sc} &= -\mu_0 J_z^{sc}, \\ \partial_y E_z^{sc} + j\omega B_x^{sc} &= 0, \\ -\partial_x E_z^{sc} + j\omega B_y^{sc} &= 0, \end{aligned} \tag{2.2.17}$$

where J_z^{sc}, called the scattering source, is given by

$$J_z^{sc} = \begin{cases} j\omega\epsilon_0\chi E_z, & \text{if } \rho \in \mathbb{D} \\ 0, & \text{otherwise} \end{cases} \tag{2.2.18}$$

From this the contrast source is defined as

$$w = \chi E_z. \tag{2.2.19}$$

Now all the ingredients are there to get an explicit expression for E_z^{sc}. Using the set of equations given by Equation (2.2.17) the following equation is found

$$\begin{aligned} -\partial_x B_y^{sc} + \partial_y B_x^{sc} + j\omega\epsilon_0\mu_0 E_z^{sc} &= -\mu_0 J_z^{sc}, \\ -\frac{1}{j\omega}\partial_x^2 E_z^{sc} - \frac{1}{j\omega}\partial_y^2 E_z^{sc} + j\omega\epsilon_0\mu_0 E_z^{sc} &= -\mu_0 J_z^{sc}, \\ (\partial_x^2 + \partial_y^2 + k_0^2)E_z^{sc} &= j\omega\mu_0 J_z^{sc}. \end{aligned} \tag{2.2.20}$$

Filling in Equation (2.2.18) results in

$$(\partial_x^2 + \partial_y^2 + k_0^2)E_z^{sc} = j\omega\mu_0 \cdot j\omega\epsilon_0\chi E_z. \tag{2.2.21}$$

Finally applying Equation (2.2.8) provides an explicit equation for E_z^{sc}

$$\begin{aligned} E_z^{sc}(\rho) &= -j\omega\mu_0 \cdot j\omega\epsilon_0 \int_{\rho\in\mathbb{D}} \hat{G}(\rho-\rho')\chi(\rho')E_z(\rho')dV, \\ &= k_0^2 \int_{\rho\in\mathbb{D}} \hat{G}(\rho-\rho')\chi(\rho')E_z(\rho')dV, \\ &= G_D\{\chi(\rho')E_z(\rho')\}, \end{aligned} \tag{2.2.22}$$

where $G_D\{\cdot\}$ is an operator that will be used later on in the algorithm.
The last thing that is left now is giving the explicit formulas for B_1^{+sc} and B_1^{-sc}. These can easily be obtained by using the last two equations from (2.2.17) and the definitions given in Equation (2.1.5) and Equation (2.1.6) and then filling in Equation (2.2.22) for E_z^{sc}. For B_1^{+sc} this comes down to

$$\begin{aligned} B_1^{+sc} &= \frac{B_x^{sc} + jB_y^{sc}}{2}, \\ &= \frac{-\partial_y E_z^{sc} + j\partial_x E_z^{sc}}{2j\omega}, \\ &= \frac{(\partial_x + j\partial_y)E_z^{sc}}{2\omega}, \\ &= \frac{k_0^2}{2\omega}(\partial_x + j\partial_y)\int_{\rho\in\mathbb{D}} \hat{G}(\rho-\rho')\chi(\rho')E_z(\rho')dV, \\ &= \frac{\omega}{2c_0^2}(\partial_x + j\partial_y)\int_{\rho\in\mathbb{D}} \hat{G}(\rho-\rho')\chi(\rho')E_z(\rho')dV, \\ &= G_S^+\{\chi(\rho')E_z(\rho')\}. \end{aligned} \tag{2.2.23}$$

Doing the same for B_1^{-sc} gives

$$\begin{aligned} B_1^{-sc^*} &= \frac{B_x^{sc} - jB_y^{sc}}{2}, \\ &= \frac{-\partial_y E_z^{sc} - j\partial_x E_z^{sc}}{2j\omega}, \\ &= \frac{(-\partial_x + j\partial_y)E_z^{sc}}{2\omega}, \\ &= -\frac{(\partial_x - j\partial_y)E_z^{sc}}{2\omega}, \\ &= -\frac{k_0^2}{2\omega}(\partial_x - j\partial_y)\int_{\rho\in\mathbb{D}} \hat{G}(\rho-\rho')\chi(\rho')E_z(\rho')dV, \\ &= -\frac{\omega}{2c_0^2}(\partial_x - j\partial_y)\int_{\rho\in\mathbb{D}} \hat{G}(\rho-\rho')\chi(\rho')E_z(\rho')dV, \\ &= G_S^-\{\chi(\rho')E_z(\rho')\}, \end{aligned} \tag{2.2.24}$$

here the operators $G_S^+\{\cdot\}$ and $G_S^-\{\cdot\}$ are introduced which again are used in the algorithm further on.
This concludes the scattering formalism. All the fields now have an explicit formula and can be computed. In the next part the incident fields are given for line sources.

2.3 The incident fields due to line sources

When assuming the fields are two-dimensional the legs of the birdcage coil can be seen as infinite line sources through which equal current flows. These line sources provide a way to calculate the incident fields for the 2D antenna setup.
So given that the external current density in Equation (2.2.10) is the line source. Which is characterized by

$$J_z^{ext} = \hat{I}(j\omega)\delta(\rho - \rho_s), \tag{2.3.1}$$

here ρ_s is the position vector of the source and $\hat{I}(j\omega)$ is the current flowing through the line. Now filling in Equation (2.3.1) in Equation (2.2.10) results in

$$E_z^i = -j\omega\mu_0 \int_{\rho' \in \mathbb{D}^{src}} \hat{G}(\rho - \rho')\hat{I}(j\omega)\delta(\rho - \rho_s)dV. \tag{2.3.2}$$

Using the property of the dirac delta function defined as

$$\int_{-\infty}^{\infty} f(x)\delta(x-a)dx = f(a). \tag{2.3.3}$$

Plus substituting Equation (2.2.9). The expression for the incident electric field condenses to

$$\begin{aligned} E_z^i(\rho) &= -j\omega\mu_0\hat{I}(j\omega)\hat{G}(\rho - \rho_s), \\ &= -j\omega\mu_0\hat{I}(j\omega) \cdot -\frac{j}{4}H_0^{(2)}(k_0|\rho - \rho_s|), \\ &= -\frac{\omega\mu_0}{4}\hat{I}(j\omega)H_0^{(2)}(k_0|\rho - \rho_s|). \end{aligned} \tag{2.3.4}$$

From the incident electric field the incident magnetic fields can be solved for. This goes analogous to the scattered fields. It starts with finding the expression for B_x^i

$$\begin{aligned} B_x^i(\rho) &= -\frac{1}{j\omega}\partial_y E_z^i, \\ &= \frac{1}{j\omega} \cdot \frac{\omega\mu_0}{4}\hat{I}(j\omega)\partial_y H_0^{(2)}(k_0|\rho - \rho_s|), \\ &= -\frac{j\mu_0}{4}\hat{I}(j\omega)\partial_y H_0^{(2)}(k_0|\rho - \rho_s|), \end{aligned} \tag{2.3.5}$$

here only the Hankel function is dependant on the spacial coordinates, the rest can be seen as a constant when taking the derivative. Using the following identity of the Hankel function [18]

$$\frac{\partial H_0^{(2)}(z)}{\partial z} = -H_1^{(2)}(z), \tag{2.3.6}$$

the derivative of the Hankel function in Equation (2.3.5) with respect to x and y is given by

$$\frac{\partial}{\partial x}H_0^{(2)}(k_0|\rho - \rho_s|) = -k_0\frac{x - x_s}{|\rho - \rho_s|}H_1^{(2)}(k_0|\rho - \rho_s|), \tag{2.3.7}$$

and

$$\frac{\partial}{\partial y}H_0^{(2)}(k_0|\rho - \rho_s|) = -k_0\frac{y - y_s}{|\rho - \rho_s|}H_1^{(2)}(k_0|\rho - \rho_s|). \tag{2.3.8}$$

Substituting Equation (2.3.8) in Equation (2.3.5) gives

$$\begin{aligned} B_x^i(\rho) &= -\frac{j\mu_0}{4}\hat{I}(j\omega) \cdot -k_0\frac{y - y_s}{|\rho - \rho_s|}H_1^{(2)}(k_0|\rho - \rho_s|), \\ &= \frac{j\mu_0 k_0}{4}\hat{I}(j\omega)\frac{y - y_s}{|\rho - \rho_s|}H_1^{(2)}(k_0|\rho - \rho_s|). \end{aligned} \tag{2.3.9}$$

Doing the same for B_y^i shows that

$$\begin{aligned} B_y^i &= \frac{1}{j\omega}\partial_x E_z^i, \\ &= \frac{1}{j\omega} \cdot -\frac{\omega\mu_0}{4}\hat{I}(j\omega)\partial_x H_0^{(2)}(k_0|\rho - \rho_s|), \\ &= \frac{j\mu_0}{4}\hat{I}(j\omega)\partial_x H_0^{(2)}(k_0|\rho - \rho_s|), \\ &= \frac{j\mu_0}{4}\hat{I}(j\omega) \cdot -k_0\frac{x - x_s}{|\rho - \rho_s|}H_1^{(2)}(k_0|\rho - \rho_s|), \\ &= -\frac{j\mu_0 k_0}{4}\hat{I}(j\omega)\frac{x - x_s}{|\rho - \rho_s|}H_1^{(2)}(k_0|\rho - \rho_s|). \end{aligned} \tag{2.3.10}$$

Now the last step is to substitute Equation (2.3.9) and Equation (2.3.10) into the definitions of B_1^+ and B_1^- given by Equation (2.1.5) and Equation (2.1.6) respectively. This results in

$$\begin{aligned} B_1^{+i} &= \frac{B_x^i + jB_y^i}{2}, \\ &= \frac{1}{2}\left(\frac{j\mu_0 k_0}{4}\hat{I}(j\omega)\frac{y-y_s}{|\rho-\rho_s|}H_1^{(2)}(k_0|\rho-\rho_s|) + j\cdot -\frac{j\mu_0 k_0}{4}\hat{I}(j\omega)\frac{x-x_s}{|\rho-\rho_s|}H_1^{(2)}(k_0|\rho-\rho_s|)\right), \\ &= \frac{\mu_0 k_0}{8}\hat{I}(j\omega)\frac{(x-x_s)+j(y-y_s)}{|\rho-\rho_s|}H_1^{(2)}(k_0|\rho-\rho_s|), \end{aligned} \tag{2.3.11}$$

and

$$\begin{aligned} B_1^{-i} &= \frac{B_x^{i^*} + jB_y^{i^*}}{2}, \\ &= \frac{1}{2}\left(-\frac{j\mu_0 k_0}{4}\hat{I}^*(j\omega)\frac{y-y_s}{|\rho-\rho_s|}H_1^{(2)^*}(k_0|\rho-\rho_s|) + j\cdot\frac{j\mu_0 k_0}{4}\hat{I}^*(j\omega)\frac{x-x_s}{|\rho-\rho_s|}H_1^{(2)^*}(k_0|\rho-\rho_s|)\right), \\ &= -\frac{\mu_0 k_0}{8}\hat{I}^*(j\omega)\frac{(x-x_s)+j(y-y_s)}{|\rho-\rho_s|}H_1^{(2)^*}(k_0|\rho-\rho_s|). \end{aligned} \tag{2.3.12}$$

Now all the equations are there to express the field created by a line source. In an MRI, however, there are multiple legs in the coil, thus multiple line sources. The total field can easily be obtained by summing all the fields from all the line sources through the use of superposition. The only thing that changes is the phase shift in each line source and the place of that line source assuming that there is no coupling from the load to the source.

2.4 Mirror sources method

The mirror source method is used to implement equipotential surfaces in models by the use of a mirror source [19]. Lets assume that there is a source at location ρ_s with a charge Q. Further there is an infinite grounded Perfect Electrical Conductor (PEC) plate at a location $x = a$ that extends to $y = \pm\infty$. Then the corresponding potential on the plate should be 0. Now the mirror source method says that by mirroring the original source in the plate and changing the sign of the charge (i.e. charge Q becomes $-Q$) this half plane can be modeled. This is visualized in Figure 2a. This works because the distance between the original source and the half plane is equal to the distance between the mirror source and the half plane. Therefor the opposing charges cancel each other out. The problem can also be described by the Dirichlet boundary conditions as

$$E_z(\rho) = \begin{cases} (\partial_x^2 + \partial_y^2 + k_0^2)E_z(\rho) = j\omega\mu_0 J_z^{ext}, & \rho > a \\ 0, & \rho = a \end{cases} \tag{2.4.1}$$

The resulting normalized potential distribution is shown in Figure 2b.
Now the same problem can be posed for a birdcage coil in an MRI because around the coil is an RF-shield. The RF-shield is there to minimize the field outside of the scanner and to keep external source outside of the scanner, this is done to minimize interference. The RF-shield can be seen as a Perfect Electrical Conductor (PEC) which encircles a certain domain $\mathbb{D}^{PEC}$. For such a shield the Dirichlet boundary condition transforms into

$$E_z(\rho) = \begin{cases} (\partial_x^2 + \partial_y^2 + k_0^2)E_z(\rho) = j\omega\mu_0 J_z^{ext}, & \rho \in \mathbb{D}^{PEC} \\ 0, & \rho \in \partial\mathbb{D}^{PEC} \end{cases} \tag{2.4.2}$$

What this means is that the fields should be 0 on the boundary of $\mathbb{D}^{PEC}$. However since simply mirroring the original source into the RF-shield does not make the distance between the shield and the original source equal to the distance between the shield and the mirror source. In [19] an improvement for the location of the mirror source is given by

$$d = \frac{R_{PEC}^2}{r_{coil}}, \tag{2.4.3}$$

where d is the distance at which the mirrored source needs to be placed with respect to the center of the coil. R_{PEC} and r_{coil} are the radii of the PEC and the coil respectively. This is a first order approximation of the shield. To get the second order approximation the mirror sources have to be mirrored into the shield again. This

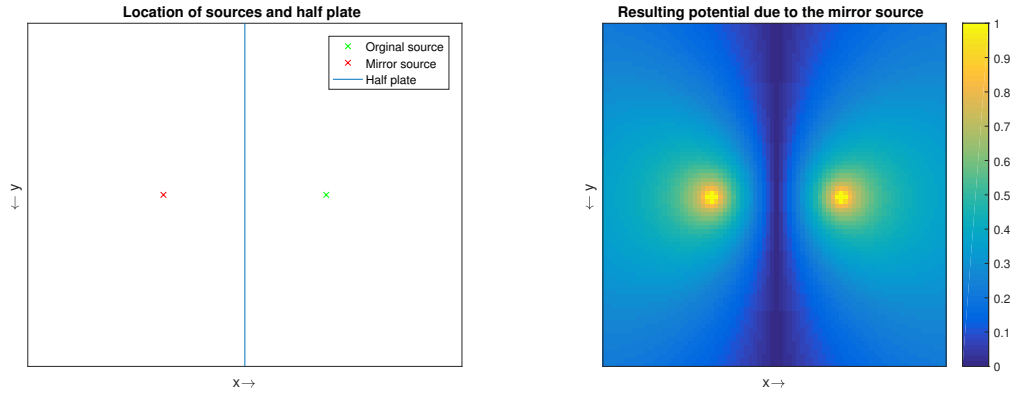

(a) The locations of the original source (green), the mirror source (red) and the half plate (blue) can be seen.

(b) The resulting normalized potential distribution due to both the sources. The value at the location of the source is set to 1.

Figure 2: A demonstration of the mirror source method. On the left is the setup of the sources and half plane. On the right is the resulting field distribution.

can be done infinitely many times to get a higher order approximation. However as will be shown in Section 4 a first order approximation is good enough to get a good quantitatively and qualitatively approximation of the incident fields of the MRI.

2.5 The transceive phase

Most of the existing MR-EPT schemes need either the complex B_1^+ field or the at least the true B_1^+ phase. Now the problem with this is that this phase cannot be measured by the scanner. The signal that is measured by the scanner for low flip angles is given by [20],[21],[22].

$$S(r) \approx \rho(r) \cdot B_1^{*-RE}(r) \frac{B_1^{+TR}(r)}{|B_1^{+TR}(r)|} f, \tag{2.5.1}$$

where ρ is the proton density of the object and f is a function that includes scaling of the amplitude and phase contributions due to relaxation and B_0 effects. From this equation it is seen that the measured phase of the signal depends on the B_1^+ in transmit and the complex conjugate of B_1^- in receive. The measured phase is thus given by

$$\phi_\pm = \phi_+ + \phi_-, \tag{2.5.2}$$

where ϕ_+ is the phase due to B_1^{+TR} and ϕ_- is the phase due to B_1^{*-RE}. It is now obvious that this poses a problem for the existing methods, since the separate phase contributions cannot be measured. A way to get around this problem is to use what is called the transceive phase assumption (TPA).
This assumption states that ϕ_+ and ϕ_- are equal and thus taking half of the measured phase results in the transmit phase, as seen by

$$\begin{aligned} \frac{\phi_\pm}{2} &= \frac{\phi_+ + \phi_-}{2}, \\ &= \frac{2\phi_+}{2}, \\ &= \phi_+. \end{aligned} \tag{2.5.3}$$

This assumption holds for a homogeneous cylinder or if the scattered fields due to the two ports cancel each other. This is shown in [20]. In the next chapter a way to get the transmit phase which is incorporated in the CSI-EPT scheme is given.

2.6 Signal-to-Noise Ratio

In the past there have been misunderstandings about how the SNR is defined in MRI experiments. And more importantly what scale to use. In the world of electrical engineering it is accustomed to use decibels (dB) for the scale of the SNR. However, in the bio-imaging world the SNR is seen as a factor. To avoid any confusion

further on, the definition of the SNR is stated below.
For this thesis the SNR is seen as a factor. Meaning an SNR of 20 states that the amplitude of the signal is 20 times larger than the amplitude of the noise.
As for how it is incorporated into the simulations in MATLAB and Sim4Life is shown below. This is also described in [2].
First the complex B_1^+ map is split into its real and imaginary parts

$$\begin{aligned} R &= \Re\{B_1^+\} = |B_1^+| \cdot cos(\phi), \\ I &= \Im\{B_1^+\} = |B_1^+| \cdot sin(\phi), \end{aligned} \tag{2.6.1}$$

where ϕ is the phase of the complex B_1^+.
Both R and I are duplicated to obtain two sets, R_1,R_2,I_1 and I_2. The first set of the real and imaginary part is used to obtain the amplitude of the complex B_1^+ map and the second set is used to obtain the phase.
This is done because in an MRI measurement the magnitude and phase are measured separately and both with a different SNR. The phase is measured with two spin echo sequences and the magnitude is measured with two repeated gradient echos.
The noise in an MRI measurement comes from black body radiation, a typical curve can be seen in Figure 3.

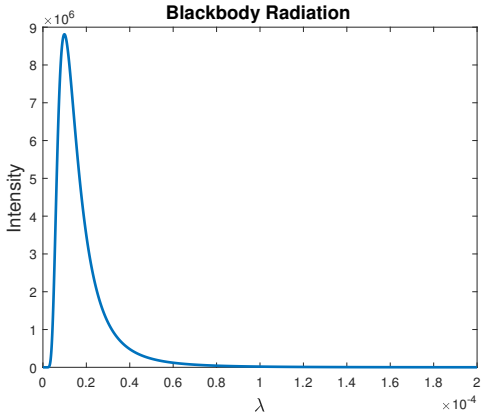

Figure 3: The black-body radiation curve for according to Planck's law at a temperature of 293 Kelvin.

The wavelength in an MRI is in the order of meters. When looking back at Figure 3 it is clearly seen that the curve becomes flat at larger wavelengths. Therefore the noise in an MRI measurement can be modeled as white Gaussian noise.
Thus four different sets of white Gaussian noise need to be constructed to obtain a realistic SNR. The corrupted maps are made by

$$\begin{aligned} \tilde{R}_1 &= R_1 + \eta_1, \\ \tilde{I}_1 &= I_1 + \eta_2, \\ \tilde{R}_2 &= R_2 + \eta_3, \\ \tilde{I}_2 &= I_2 + \eta_4, \end{aligned} \tag{2.6.2}$$

here η is the Gaussian noise, where η_1 and η_2 are related but independent of each other. The same holds for the η_3 and η_4. For $\eta_{1,2}$ the standard deviation is given by σ_{mag} and for $\eta_{3,4}$ the standard deviation is given by σ_{phase}

$$\begin{aligned} \sigma_{mag} &= \frac{\bar{r}}{SNR_{mag}}, \\ \sigma_{phase} &= \frac{\bar{r}}{SNR_{phase}}, \end{aligned} \tag{2.6.3}$$

here SNR_{mag} and SNR_{phase} denote the SNR of the magnitude measurement and phase measurement respectively. While $\bar{r}$ denotes the mean magnitude of the amplitude of the complex B_1^+ map. This amplitude is taken in the area where the object is located in the field of view (FoV) , because only this can be measured in an

MRI scanner whereas in Matlab and Sim4Life the complete electric and magnetic field distributions can be simulated.
Since the real and imaginary parts are corrupted separately, the corrupted magnitude and phase are obtained by

$$|\tilde{B}_1^+| = \sqrt{\tilde{R}_1^2 + \tilde{I}_1^2}, \tag{2.6.4}$$

$$\angle\tilde{B}_1^+ = \text{atan2}(\tilde{I}_2, \tilde{R}_2). \tag{2.6.5}$$

Combining Equation (2.6.4) and Equation (2.6.5) the corrupted complex B_1^+ map is acquired by

$$\tilde{B}_1^+ = |\tilde{B}_1^+| e^{i\angle\tilde{B}_1^+}. \tag{2.6.6}$$

3 The Contrast Source Inversion Method

This chapter begins with the idea of standard CSI for MRI purposes. The problems of this method are discussed and an improved update scheme is given.
To compute the scattered fields a discrete Green's function needs to be computed. For this the weak Green's function from [23] was used.

3.1 Contrast Source Inversion in an MRI setting

3.1.1 Cost Functional

From [11] the generalized cost functional that needs to be minimized is defined as

$$F(w_j, \chi) = \eta_S \Sigma_j ||f_j - G_S^+\{w_j\}||_S^2 + \eta_D \Sigma_j ||\chi u_j^{inc} - w_j + \chi G_D\{w_j\}||_D^2, \tag{3.1.1}$$

here f_j is the measured data where j are the different antenna settings and w_j is the corresponding contrast source which in the generalized form is

$$w_j = \chi u_j. \tag{3.1.2}$$

Further in this equation η_s and η_D are the normalization factors defined as

$$\begin{aligned} \eta_S &= \left(\Sigma_j ||f_j||_S^2\right)^{-1}, \\ \eta_D &= \left(\Sigma_j ||\chi u_j^{inc}||_D^2\right)^{-1}. \end{aligned} \tag{3.1.3}$$

Now in an ideal MRI setting, with ideal meaning the measured data being the complex B_1^{+TR}, Equation (3.1.1) transforms to

$$F(w_j^{TR}, \chi) = \eta_S \Sigma_j ||B_{1,j}^{+sc,TR} - G_S^+\{w_j^{TR}\}||_S^2 + \eta_D \Sigma_j ||\chi E_{z,j}^{inc,TR} - w_j^{TR} + \chi G_D\{w_j^{TR}\}||_D^2, \tag{3.1.4}$$

with

$$\begin{aligned} \eta_S &= \left(\Sigma_j ||B_{1,j}^{+sc,TR}||_S^2\right)^{-1}, \\ \eta_D &= \left(\Sigma_j ||\chi E_{z,j}^{inc,TR}||_D^2\right)^{-1}. \end{aligned} \tag{3.1.5}$$

The cost function in Equation (3.1.4) is minimized using a nonlinear Polak-Ribière updating scheme.
The first thing to do is defining the cost function at each iteration

$$F_n(w_j^{TR}, \chi) = \eta_S \Sigma_j ||B_{1,j}^{+sc,TR} - G_S^+\{w_j^{TR}\}||_S^2 + \eta_{D,n} \Sigma_j ||\chi E_{z,j}^{inc,TR} - w_j^{TR} + \chi G_D\{w_j^{TR}\}||_D^2, \tag{3.1.6}$$

with

$$\begin{aligned} \eta_S &= \left(\Sigma_j ||B_{1,j}^{+sc,TR}||_S^2\right)^{-1}, \\ \eta_{D,n} &= \left(\Sigma_j ||\chi_{n-1} E_{z,j}^{inc,TR}||_D^2\right)^{-1}. \end{aligned} \tag{3.1.7}$$

Equation (3.1.6) consists of two separate parts, the first is called the data cost functional and the other the object cost functional. These are given by

$$\begin{aligned} F_S(w_j^{TR}) &= \eta_S \Sigma_j ||B_{1,j}^{+sc,TR} - G_S^+\{w_j^{TR}\}||_S^2, \\ F_{D,n}(w_j^{TR}, \chi) &= \eta_{D,n} \Sigma_j ||\chi E_{z,j}^{inc,TR} - w_j^{TR} + \chi G_D\{w_j^{TR}\}||_D^2. \end{aligned} \tag{3.1.8}$$

Now that the cost functional is known the algorithm can be started by defining the residuals, the error of the estimation compared to the measured data. Again there is a data and an object variant. The data residual is given by

$$\rho_{j,n} = B_{1,j}^{+sc,TR} - G_S^+\{w_{j,n}^{TR}\} \tag{3.1.9}$$

and the object residual is given by

$$r_{j,n} = \chi_n E^{inc,TR}_{z,j} - w^{TR}_{j,n} + \chi_n G_D\{w^{TR}_{j,n}\}. \tag{3.1.10}$$

The to be minimized cost function and the corresponding residuals are known. How these residuals are minimized is in the next section.

3.1.2 Update scheme contrast source

The update formula for the contrast source is defined as

$$w^{TR}_{j,n} = w^{TR}_{j,n-1} + \alpha_n^{w^{TR}} v_{j,n}, \tag{3.1.11}$$

here $\alpha_n^{w^{TR}}$ is the stepsize and $v_{j,n}$ is the update direction. The stepsize that minimizes the cost function can be found by solving

$$\alpha_n^{w^{TR}} = arg\min_{\Re\alpha}\{F_n(w^{TR}_{j,n-1} + \alpha v_{j,n}, \chi_{n-1})\}. \tag{3.1.12}$$

The update direction is given by

$$v_{j,n} = \begin{cases} 0, & n = 0 \\ g_{j,n}^{w_j^{TR}} + \frac{\Sigma_j < g_{j,n}^{w_j^{TR}}, g_{j,n}^{w_j^{TR}} - g_{j,n-1}^{w_j^{TR}} >_D}{\Sigma_j ||g_{j,n-1}^{w_j^{TR}}||^2_D} v_{j,n-1}, & n \geq 1 \end{cases} \tag{3.1.13}$$

In Equation (3.1.13) $g_{j,n}^{w^{TR}}$ is the gradient of the cost functional in Equation (3.1.4) with respect to w^{TR}. This gradient can easily be found by using Taylor's theorem [24]

$$F_n(w^{TR}_{j,n-1} + \alpha v_{j,n}, \chi_{n-1}) = F_n(w^{TR}_{j,n-1}, \chi_{n-1}) + \alpha < g_{j,n}^{w^{TR}}, v_{j,n} >_D + o(\alpha). \tag{3.1.14}$$

Applying this definition to Equation (3.1.4) gives the following result

$$F_n(w^{TR}_{j,n-1} + \alpha v_{j,n}, \chi_{n-1}) = F_S(w^{TR}_{j,n-1} + \alpha v_{j,n}) + F_{D_n}(w^{TR}_{j,n-1} + \alpha v_{j,n}, \chi_{n-1}). \tag{3.1.15}$$

For the data cost functional this results in

$$\begin{aligned} F_S(w^{TR}_{j,n-1} + \alpha v_{j,n}) &= \eta_S \Sigma_j ||B^{+sc,TR}_{1,j} - G^+_S\{w^{TR}_{j,n} + \alpha v_{j,n}\}||^2_S, \\ &= \eta_S \Sigma_j ||B^{+sc,TR}_{1,j} - G^+_S\{w^{TR}_{j,n}\} - \alpha G^+_S\{v_{j,n}\}||^2_S, \\ &= \eta_S \Sigma_j ||\rho_{j,n-1} - \alpha G^+_S\{v_{j,n}\}||^2_S, \\ &= \eta_S \Sigma_j \left(||\rho_{j,n-1}||^2_S - 2\alpha < \rho_{j,n-1}, G^+_S\{v_{j,n}\} >_D + \alpha^2 ||G^+_S\{v_{j,n}\}||^2_S \right), \\ &= \eta_S \Sigma_j \left(||\rho_{j,n-1}||^2_S - 2\alpha < G^{+,\dagger}_S\{\rho_{j,n-1}\}, v_{j,n} >_D + \alpha^2 ||G^+_S\{v_{j,n}\}||^2_S \right) \end{aligned} \tag{3.1.16}$$

and for the object cost functional

$$\begin{aligned} F_{D_n}(w^{TR}_{j,n-1} + \alpha v_{j,n}, \chi_{n-1}) &= \eta_{D,n} \Sigma_j ||\chi_{n-1} E^{inc,TR}_{z,j} - w^{TR}_{j,n-1} - \alpha v_{j,n} + \chi_{n-1} G_D\{w^{TR}_{j,n-1} + \alpha v_{j,n}\}||^2_D, \\ &= \eta_{D,n} \Sigma_j ||\chi_{n-1} E^{inc,TR}_{z,j} - w^{TR}_{j,n-1} - \alpha v_{j,n} + \chi_{n-1} G_D\{w^{TR}_{j,n-1}\} + \alpha \chi_{n-1} G_D\{v_{j,n}\}||^2_D, \\ &= \eta_{D,n} \Sigma_j ||r_{j,n} - \alpha v_{j,n} + \alpha \chi_{n-1} G_D\{v_{j,n}\}||^2_D, \\ &= \eta_{D,n} \Sigma_j ||r_{j,n} + \alpha(\chi_{n-1} G_D\{v_{j,n}\} - v_{j,n})||^2_D, \\ &= \eta_{D,n} \Sigma_j \left(||r_{j,n}||^2_D + 2\alpha < r_{j,n}, (\chi_{n-1} G_D\{v_{j,n}\} - v_{j,n}) >_D + \alpha^2 ||\chi_{n-1} G_D\{v_{j,n}\} - v_{j,n}||^2_D \right), \\ &= \eta_{D,n} \Sigma_j \left(||r_{j,n}||^2_D + 2\alpha < G^\dagger_D\{\chi^*_{n-1} r_{j,n}\} - r_{j,n}, v_{j,n} >_D + \alpha^2 ||\chi_{n-1} G_D\{v_{j,n}\} - v_{j,n}||^2_D \right). \end{aligned} \tag{3.1.17}$$

Finally filling in Equation (3.1.16) and Equation (3.1.17) in (3.1.14) gives the explicit expression for the gradient as

$$g_{j,n}^{w^{TR}} = -2\Sigma_j \left(\eta_S G^{+,\dagger}_S\{\rho_{j,n-1}\} + \eta_{D,n} \left(r_{n,j} - G^\dagger_D\{\chi^*_{n-1} r_{n,j}\} \right) \right). \tag{3.1.18}$$

From the definition in Equation (3.1.14) the stepsize is also easily obtained by taking the derivative with respect to α and setting the result to zero, thus finding a minimum.

$$\begin{aligned} \frac{\partial F_n(w_{j,n-1}^{TR}+\alpha v_{j,n},\chi_{n-1})}{\partial \alpha} &= 0 \\ \frac{\partial F_S(w_{j,n-1}^{TR}+\alpha v_{j,n})}{\partial \alpha} + \frac{\partial F_{D_n}(w_{j,n-1}^{TR}+\alpha v_{j,n},\chi_{n-1})}{\partial \alpha} &= 0 \end{aligned} \tag{3.1.19}$$

Filling in the results from (3.1.16) and (3.1.17) gives an analytical solution to Equation (3.1.12). Given by

$$\begin{aligned} \eta_S\Sigma_j\left(-2<G_S^{+,\dagger}\{\rho_{j,n-1}\},v_{j,n}>_D+2\alpha||G_S^+\{v_{j,n}\}||_S^2\right)...\\ +\eta_{D,n}\Sigma_j\left(2<(G_D^\dagger\chi_{n-1}^*-I)r_{n,j},v_{j,n}>_D+2\alpha||(\chi_{n-1}G_D-I)v_{j,n}||_D^2\right)=0,\\ \Sigma_j\left(2\eta_S\alpha||G_S^+\{v_{j,n}\}||_S^2+2\eta_{D,n}\alpha||(\chi_{n-1}G_D-I)v_{j,n}||_D^2\right)=...\\ -\Sigma_j\left(-2\eta_S<G_S^{+,\dagger}\{\rho_{j,n-1}\},v_{j,n}>_D+2\eta_{D,n}<(G_D^\dagger\chi_{n-1}^*-I)r_{n,j},v_{j,n}>_D\right),\\ \alpha\Sigma_j\left(2\eta_S||G_S^+\{v_{j,n}\}||_S^2+2\eta_{D,n}||(\chi_{n-1}G_D-I)v_{j,n}||_D^2\right)=-\Sigma_j<g_{j,n}^{w^{TR}},v_{j,n}>_D,\\ \alpha=-\frac{1}{2}\frac{\Sigma_j<g_{j,n}^{w^{TR}},v_{j,n}>_D}{\Sigma_j\left(\eta_S||G_S^+\{v_{j,n}\}||_S^2+\eta_{D,n}||(\chi_{n-1}G_D-I)v_{j,n}||_D^2\right)}, \end{aligned} \tag{3.1.20}$$

with the stepsize and update direction known it is possible to update the contrast source by substituting Equation (3.1.13) and Equation (3.1.20) in Equation (3.1.11).

3.1.3 Updating the total electric field

Now that the contrast source is updated Equation (2.2.22) can be solved to get the scattered electric field. This together with the incident electric field can then be substituted into

$$E_{z,j,n}^{TR}=E_{z,j}^{inc,TR}+G_D\{w_{j,n}^{TR}\}. \tag{3.1.21}$$

This single equation concludes the updating of the total electric field.

3.1.4 Update scheme contrast

It is clearly seen that the data cost functional is not dependent on the contrast and only the object cost functional is. Plus using Equation (3.1.21) the object cost functional in Equation (3.1.8) can be rewritten to

$$F_{D,n}=\eta_{D,n}\Sigma_j||\chi E_{z,j}^{TR}-w_j^{TR}\}||_D^2. \tag{3.1.22}$$

Minimizing the object cost functional is now as easy as using the least squares solution which is given by

$$\chi_n=\frac{\Sigma_j w_{j,n}^{TR}E_{z,j,n}^{*TR}}{\Sigma_j|E_{z,j,n}^{TR}|^2}. \tag{3.1.23}$$

Of course the contrast can be updated using again the Polak-Ribière update directions, however this doesn't yield better results since they boil down to the same result.

3.1.5 Starting the algorithm

Now that the update scheme is known the algorithm needs to be initialized by a first guess. For this two options can be used, the first is simply using back propagation, which is defined as [11]

$$w_{j,0}^{TR}=\frac{||G_S^{+,\dagger}\{f_j\}||_D^2}{||G_S^+\{G_S^{+,\dagger}\{f_j\}\}||_S^2}G_S^{+,\dagger}\{f_j\}. \tag{3.1.24}$$

Substituting the result in (3.1.21) and finally in (3.1.23) will yield $E_{z,j,0}^{TR}$ and χ_0 respectively.
This is a decent start for the algorithm to work with, however with *a priori* information about the object that is scanned a much better initial guess can be made. In an MRI setting T1 or T2 weighted images are made very quickly, these can be used as a mask to which a certain conductivity and permittivity can be coupled. For

example the literature values for muscle. Or taking it a step further and identifying the tissue types present and linking the correct contrast values to that will result in a very accurate initial guess.
With this first guess for a contrast Equation (3.1.21) needs to be solved for the total electric field and using (2.2.19) the initial guess for the contrast sources can be acquired.

3.1.6 Total variation

In principal the algorithm described above would give solutions that are close to the true contrast. However in practice the measured data is corrupted with noise. The pleasant thing about this update scheme is that corrections can be done at each iteration rather than having a certain corrupted input and thus a corrupted output as is the case with many of the EPT schemes out there.
To handle the noise in this algorithm a new cost functional is introduced that incorporates a total variation denoising term [25]. First a small introduction to Total Variation (TV) is given and after that the new cost functional and update scheme are presented.

Total variation in a general sense
Let u_0 be the noise free image and $\tilde{u}$ the corrupted image given by

$$\tilde{u} = u_0 + \eta, \tag{3.1.25}$$

where η is white Gaussian noise. One property that is known about white Gaussian noise is that the mean value is 0

$$\bar{\eta} = 0. \tag{3.1.26}$$

With this property it is directly visible that the mean value of the true image and the corrupted image should be equal shown by

$$\begin{aligned} \bar{\tilde{u}} &= \overline{u_0 + \eta}, \\ &= \bar{u}_0 + \bar{\eta}, \\ &= \bar{u}_0. \end{aligned} \tag{3.1.27}$$

The next property of noise that is known is that it fluctuates, or in mathematical terms the norm of the gradient of noise is high thus

$$||\nabla \tilde{u}||_p > ||\nabla u_0||_p \tag{3.1.28}$$

where p denotes either the 1 or 2 norm.
In order to get the true image back from the corrupted image the gradient of has to be minimized while the mean value is kept the same. A cost functional that goes with this is given by

$$F(x) = ||\tilde{u} - x||_2^2 + \delta ||\nabla x||_p^2, \tag{3.1.29}$$

here the parameter δ is a steering parameter, it depicts the importance of minimizing the gradient compared to keeping the mean value the same. It is difficult to make an absolute choice for this parameter as it depends heavily on the kind of reconstruction that is done. For every reconstruction the steering parameter can be different.
Choosing to minimize the 2-norm will result in a smoothed image, whereas minimizing the 1-norm gives a more blocky image.

Total variation in CSI-EPT
Now that the basic idea for total variation is known it can be introduced into the existing algorithm. The choice was made to have a multiplicative TV term instead of an additive one. This choice was made on the basis that with the additive TV term a certain weight/importance has to be given to minimizing the gradient. With the multiplicative TV term this weighing is done automatically [11]. This gives rise to the cost functional

$$F_n^R(w_j^{TR}, \chi) = \left(F_S(w_j^{TR}) + F_{D,n}(w_j^{TR}, \chi)\right) F_n^{TV}(\chi). \tag{3.1.30}$$

A desirable property for F_n^{TV} is

$$F_n^{TV}(\chi_{n-1}) = 1, \tag{3.1.31}$$

because if this is true then with updating the contrast source the old cost functional is kept as

$$\begin{aligned} F_n^R(w_{j,n-1}^{TR} + \alpha V_{j,n}, \chi_{n-1}) &= \left(F_S(w_{j,n-1}^{TR}) + F_{D,n}(w_{j,n-1}^{TR}, \chi_{n-1})\right) F_n^{TV}(\chi_{n-1}), \\ &= F_S(w_{j,n-1}^{TR}) + F_{D,n}(w_{j,n-1}^{TR}, \chi_{n-1}). \end{aligned} \tag{3.1.32}$$

Because of this the update scheme for the contrast source as well as updating the total electric field is kept the same as before. The only thing that changes is the update scheme for the contrast. This is no longer a least squares solution.
The update formula for the contrast is now given by

$$\chi_n = \chi_{n-1} + \beta d_n, \tag{3.1.33}$$

where again β is the stepsize and d_n is the Polak-Ribière update direction as given by

$$d_n = \begin{cases} 0, & n = 0 \\ g_n^\chi + \frac{<g_n^\chi, g_n^\chi - g_{n-1}^\chi>_D}{||g_{n-1}^\chi||_D^2} d_{n-1}, & n \geq 1 \end{cases} \tag{3.1.34}$$

Again using Taylor's theorem the gradient can be found relatively easy

$$F_n^R(w_{j,n}^{TR}, \chi_{n-1} + \beta d_n) = F_n^R(w_{j,n}^{TR}, \chi_{n-1}) + \beta < g_n^\chi, d_n >_D + o(\beta). \tag{3.1.35}$$

From the property given in Equation (3.1.31) it can directly be seen that

$$F_n^R(w_{j,n}^{TR}, \chi_{n-1}) = F_n(w_{j,n}^{TR}, \chi_{n-1}). \tag{3.1.36}$$

Working out equation (3.1.35)

$$\begin{aligned} F_n^R(w_{j,n}^{TR}, \chi_{n-1} + \beta d_n) &= F_n(w_{j,n}^{TR}, \chi_{n-1} + \beta d_n) F_n^{TV}(, \chi_{n-1} + \beta d_n), \\ &= (F_n(w_{j,n}, \chi_{n-1}) + \beta < g_n, d_n >_D + o(\beta)) \cdot \left(F_n^{TV}(\chi_{n-1}) + \beta < g_n^{TV}, d_n >_D + o(\beta)\right), \end{aligned} \tag{3.1.37}$$

where g_n and g_n^{TV} are the gradient of F_n and F_n^{TV} respectively. These are evaluated at the points $w_j = w_{j,n}$ and $\chi = \chi_{n-1}$.
Continuing with Equation (3.1.37)

$$\begin{aligned} F_n^R(w_{j,n}^{TR}, \chi_{n-1} + \beta d_n) &= F_n^R(w_{j,n}^{TR}, \chi_{n-1}) + \beta \left(F_n(w_{j,n}, \chi_{n-1}) < g_n^{TV}, d_n >_D + F_n^{TV}(\chi_{n-1}) < g_n, d_n >_D\right) + o(\beta), \\ &= F_n^R(w_{j,n}^{TR}, \chi_{n-1}) + \beta < F_n(w_{j,n}, \chi_{n-1}) g_n^{TV} + g_n, d_n >_D + o(\beta). \end{aligned} \tag{3.1.38}$$

From this an expression for the gradient is given by

$$g_n^\chi = F_n(w_{j,n}, \chi_{n-1}) g_n^{TV} + g_n. \tag{3.1.39}$$

The only thing left to do to get the update direction is to get an expression for g_n^{TV} and g_n. First up is the g_n term, as was done before to get this gradient Taylor's theorem is used as

$$\begin{aligned} F_n(w_{j,n}, \chi_{n-1} + \beta d_n) &= F_S(w_{j,n}) + F_{D,n}(w_{j,n}, \chi_{n-1} + \beta d_n) \\ &= F_S(w_{j,n}) + \eta_{D,n}\Sigma_j < \chi_{n-1} E_{z,j,n}^{TR} - w_{j,n} + \beta d_n E_{z,j,n}^{TR}, \chi_{n-1} E_{z,j,n}^{TR} - w_{j,n} + \beta d_n E_{z,j,n}^{TR} >_D, \\ &= F_S(w_{j,n}) + F_{D,n}(w_{j,n}, \chi_{n-1}) + 2\beta\eta_{D,n}\Sigma_j < \chi_{n-1} E_{z,j,n}^{TR} - w_{j,n}, E_{z,j,n}^{TR} d_n >_D + \beta^2 \eta_{D,n}\Sigma_j ||E_{z,j,n}^{TR} d_n||_D^2 \\ &= F_n(w_{j,n}, \chi_{n-1}) + 2\beta\eta_{D,n}\Sigma_j < (\chi_{n-1} E_{z,j,n}^{TR} - w_{j,n}) E_{z,j,n}^{*TR}, d_n >_D + \beta^2 \eta_{D,n}\Sigma_j ||E_{z,j,n}^{TR} d_n||_D^2. \end{aligned} \tag{3.1.40}$$

From Equation (3.1.40) it can be seen that

$$g_n = 2\eta_{D,n}\Sigma_j (\chi_{n-1} E_{z,j,n}^{TR} - w_{j,n}) E_{z,j,n}^{*TR} \tag{3.1.41}$$

Now for the second gradient g_n^{TV} an explicit expression for F_n^{TV} is needed, this factor is introduced as

$$F_n^{TV}(\chi) = \frac{\int_D (|\nabla \chi|^2 + \delta_{n-1}^2 dV)^{p/2}}{\int_D (|\nabla \chi_{n-1}|^2 + \delta_{n-1}^2 dV)^{p/2}}, \tag{3.1.42}$$

here p denotes the norm that needs to be minimized, if $p = 1$ the 1-norm is minimized. This gives more piecewise constant areas whereas $p = 2$ the 2-norm minimizes and results in a more smoothed contrast. In the algorithm that is used for the rest of this work a weighted 2-norm variant is chosen for the TV factor, this is given by

$$F_n^{TV}(\chi) = \frac{1}{V}\int_D \frac{(|\nabla\chi|^2 + \delta_{n-1}^2 dV)}{(|\nabla\chi_{n-1}|^2 + \delta_{n-1}^2 dV)}, \tag{3.1.43}$$

where V is the 2-D volume of the object domain. The biggest benefit of choosing the 2-norm variant is that the stepsize can be expressed analytically which is not the case with the 1-norm variant. This is due to the stepsize being inside the square root of the integral.
The term δ_{n-1}^2 is a steering parameter. From Equation (3.1.42) it can be seen that when this parameter is very large then $F_n^{TV} \approx 1$ and the cost functional returns to Equation (3.1.4). The same holds when

$$|\nabla\chi_{n-1}|^2 \approx |\nabla\chi|^2. \tag{3.1.44}$$

In both cases the TV term plays no role, thus choosing an appropriate δ_{n-1}^2 becomes a real art. This decision depends heavily on what the user of the algorithm wants as an output. Results can be achieved where the reconstruction correctly shows all the boundaries and gets the small spots where the contrast has a certain value for only a few pixels. However in those cases the contrast is not constant where it should be. Choosing the steering parameter differently might result in better piecewise constant reconstructions but then the boundaries are not as clear and small peaks in the contrast can be filtered out. A few different steering parameters will be shown in the results section of this work.
Continuing with the task at hand, which was getting the gradient g_n^{TV}. To make writing this down somewhat simpler the following variable is introduced as

$$b_{n-1} = \frac{1}{\sqrt{V(|\nabla\chi_{n-1}|^2 + \delta_{n-1}^2)}}. \tag{3.1.45}$$

Equation (3.1.43) then becomes

$$\begin{aligned} F_n^{TV}(\chi) &= \int_D b_{n-1}^2(|\nabla\chi|^2 + \delta_{n-1}^2 dV), \\ &= ||b_{n-1}\nabla\chi||_D^2 + \delta_{n-1}^2||b_{n-1}||_D^2. \end{aligned} \tag{3.1.46}$$

Again Taylor's theorem is used to get the gradient from this cost functional

$$\begin{aligned} F_n^{TV}(\chi_{n-1} + \beta d_n) &= ||b_{n-1}\nabla\chi_{n-1} + \beta\nabla d_n||_D^2 + \delta_{n-1}^2||b_{n-1}||_D^2, \\ &=< b_{n-1}\nabla\chi_{n-1} + \beta\nabla d_n, b_{n-1}\nabla\chi_{n-1} + \beta\nabla d_n >_D + \delta_{n-1}^2||b_{n-1}||_D^2, \\ &= F_n^{TV}(\chi_{n-1}) + 2\beta < b_{n-1}\nabla d_n, b_{n-1}\nabla\chi_{n-1} >_D + \beta^2||b_{n-1}\nabla d_n||_D^2. \end{aligned} \tag{3.1.47}$$

From the definition of the inner product the following equation results

$$\begin{aligned} < b_{n-1}\nabla d_n, b_{n-1}\nabla\chi_{n-1} >_D &= \Re\int_D b_{n-1}\nabla d_n \cdot (b_{n-1}\nabla\chi_{n-1})^* dV, \\ &= \Re\int_D \nabla d_n \cdot b_{n-1}^2\nabla\chi_{n-1}^* dV. \end{aligned} \tag{3.1.48}$$

Now this last term can be rewritten to

$$\nabla d_n \cdot b_{n-1}^2\nabla\chi_{n-1}^* = \nabla\cdot(d_n \cdot b_{n-1}^2\nabla\chi_{n-1}^*) - d_n\nabla\cdot(b_{n-1}^2\nabla\chi_{n-1}^*). \tag{3.1.49}$$

Substituting this into Equation (3.1.48) results in

$$\Re\int_D \nabla d_n \cdot b_{n-1}^2\nabla\chi_{n-1}^* dV = \Re\int_D \nabla\cdot(d_n \cdot b_{n-1}^2\nabla\chi_{n-1}^*)dV - \Re\int_D d_n\nabla\cdot(b_{n-1}^2\nabla\chi_{n-1}^*)dV. \tag{3.1.50}$$

It can be shown that the first term on the right-hand side of Equation (3.1.50) vanishes [17]. This leaves

$$\Re\int_D \nabla d_n \cdot b_{n-1}^2\nabla\chi_{n-1}^* dV = -\Re\int_D d_n\nabla\cdot(b_{n-1}^2\nabla\chi_{n-1}^*)dV. \tag{3.1.51}$$

Finally substituting this back into Equation (3.1.48) results in

$$\begin{aligned} < b_{n-1}\nabla d_n, b_{n-1}\nabla\chi_{n-1} >_D &= -\Re\int_D d_n\nabla\cdot(b_{n-1}^2\nabla\chi_{n-1}^*)dV, \\ &= - < d_n, \nabla\cdot(b_{n-1}^2\nabla\chi_{n-1}) >_D . \end{aligned} \tag{3.1.52}$$

When this outcome is substituted in Equation (3.1.47) it reveals the gradient to be

$$g_n^{TV} = -2\nabla\cdot(b_{n-1}^2\nabla\chi_{n-1}). \tag{3.1.53}$$

Now all the pieces for the total gradient are known and can be filled into Equation (3.1.39) to obtain

$$g_n^{\chi} = -2F_n(w_{j,n},\chi_{n-1})\nabla\cdot(b_{n-1}^2\nabla\chi_{n-1}) + 2\eta_{D,n}\Sigma_j(\chi_{n-1}E_{z,j,n}^{TR} - w_{j,n})E_{z,j,n}^{*TR}. \tag{3.1.54}$$

The only unknown at this point is the stepsize. Since the choice was made to minimize the 2-norm the stepsize can be found explicitly by taking the derivative of Equation (3.1.38) with respect to the stepsize and setting the result to zero

$$\frac{\partial F_n^R(w_{j,n}^{TR},\chi_{n-1}+\beta d_n)}{\partial\beta} = 0. \tag{3.1.55}$$

Filling in the results from (3.1.40), (3.1.47) and (3.1.52) results in

$$\frac{\partial\left(\begin{array}{r}\left(F_n(w_{j,n},\chi_{n-1}) + 2\beta\eta_{D,n}\Sigma_j < (\chi_{n-1}E_{z,j,n}^{TR} - w_{j,n})E_{z,j,n}^{*TR}, d_n >_D + \beta^2\eta_{D,n}\Sigma_j||E_{z,j,n}^{TR}d_n||_D^2\right) \\ \cdot\left(F_n^{TV}(\chi_{n-1}) - 2\beta < d_n, \nabla\cdot(b_{n-1}^2\nabla\chi_{n-1}) >_D + \beta^2||b_{n-1}\nabla d_n||_D^2\right)\end{array}\right)}{\partial\beta} = 0. \tag{3.1.56}$$

To make this more readable the following variables are introduced

$$\begin{array}{ll} a = F_n(w_{j,n},\chi_{n-1}), & b = 2\eta_{D,n}\Sigma_j < (\chi_{n-1}E_{z,j,n}^{TR} - w_{j,n})E_{z,j,n}^{*TR}, d_n >_D, \\ c = \eta_{D,n}\Sigma_j||E_{z,j,n}^{TR}d_n||_D^2, & d = F_n^{TV}(\chi_{n-1}) = 1, \\ e = -2 < d_n, \nabla\cdot(b_{n-1}^2\nabla\chi_{n-1}) >_D, & f = ||b_{n-1}\nabla d_n||_D^2. \end{array} \tag{3.1.57}$$

With this in place Equation (3.1.56) transforms into

$$\begin{aligned} \frac{\partial\left(\left(a+b\beta+c\beta^2\right)\cdot\left(d+e\beta+f\beta^2\right)\right)}{\partial\beta} &= 0, \\ \frac{\partial\left(ad+ae\beta+af\beta^2+bd\beta+be\beta^2+bf\beta^3+cd\beta^2+ce\beta^3+cf\beta^4\right)}{\partial\beta} &= 0, \\ ae+2af\beta+bd+2be\beta+3bf\beta^2+2cd\beta+3ce\beta^2+4cf\beta^3 &= 0, \\ ae+b+2(af+be+c)\beta+3(ce+bf)\beta^2+4cf\beta^3 &= 0. \end{aligned} \tag{3.1.58}$$

This third order polynomial has three roots, two which are complex and one that is real [11]. The real root is the one that will minimize the cost functional and thus should be computed. In [26] a different update scheme is given for the contrast which is very similar to the one that has been shown here. The difference with this method of updating is that there first the contrast is updated according to Equation (3.1.23). Then after that a TV regularisation step is taken in the form of

$$\chi_n^{TV} = \chi_n + \alpha^{TV}v_n^{TV}, \tag{3.1.59}$$

where again α^{TV} is the stepsize and v_n^{TV} is the Polak-Ribière update direction. The overall idea of the update is the same as discussed above. This version was implemented in the CSI method.

3.2 Improving the algorithm for an MRI setting

So far the algorithm assumes that the true complex $B_1^{+sc,TR}$ is known. However, as discussed in 2.5 this is not the case. The MRI scanner measures the total B_1^+ amplitude and the transceive phase. Going from the total field to the scattered field not a big problem, simply subtracting the incident field from the total field as shown in (2.2.4) will give the scattered field.

The problem is the transceive phase, in the results section a reconstruction with the standard CSI-EPT scheme with the transceive phase as input will be shown. The measured data is thus given by

$$\begin{aligned} f_j &= |B_{1,j}^{+TR}|e^{i\phi_{\pm}}, \\ &= |B_{1,j}^{+TR}|e^{i(\phi_+ + \phi_-)}, \\ &= |B_{1,j}^{+TR}|e^{i\phi_+}e^{i\phi_-}. \end{aligned} \tag{3.2.1}$$

The data cost functional from Equation (3.1.8) changes to

$$F_S(w_j^{TR}) = \eta_S \Sigma_j ||| B_{1,j}^{+TR}|e^{i\phi_+}e^{i\phi_-} - G_S^+\{w_j^{TR}\}||_S^2. \tag{3.2.2}$$

Correcting for the total field gives rise to

$$\begin{aligned} F_S(w_j^{TR}) &= \eta_S \Sigma_j ||| B_{1,j}^{+TR}|e^{i\phi_+}e^{i\phi_-} - G_S^+\{w_j^{TR}\} - B_{1,j}^{+i,TR}||_S^2, \\ &= \eta_S \Sigma_j || B_{1,j}^{+TR}e^{i\phi_-} - G_S^+\{w_j^{TR}\} - B_{1,j}^{+i,TR}||_S^2. \end{aligned} \tag{3.2.3}$$

Now the problem that is left is correcting the cost functional for the transceive phase. The term $G_S^+\{w_j^{TR}\}$ in the cost functional above is the $B_1^{+sc,TR}$ field, thus the only difference with that and the measured data is the term $e^{i\phi_-}$ which is dependent on the $B_1^{-,RE}$. Note that there is no 'j' in the subscript, this is because it would make no sense to receive the signal with a lower receive sensitivity. As this would only lower the SNR of the measurement. Thus receiving is only done in reverse quadrature.
From Equation (2.2.4) it can be seen again that

$$B_1^{-,RE} = B_1^{-i,RE} + B_1^{-sc,RE}. \tag{3.2.4}$$

Luckily in section 2.3 not only an expression for the B_1^{+i} field was derived but for the B_1^{-i} field as well. To get the $B_1^{-i,RE}$ the correct phase shift has to be given to each line source. Further an expression for the scattered field can be deduced from (2.2.24)

$$B_1^{-sc,RE} = G_S^-\{\chi E_z^{RE}\}. \tag{3.2.5}$$

To solve (3.2.5) the total electric field during receiving is needed. Again going back to Equation (2.2.4) and substituting the outcome of (2.2.22) this field can be written as

$$\begin{aligned} E_z^{RE} &= E_z^{i,RE} + E_z^{sc,RE}, \\ &= E_z^{i,RE} + G_D\{\chi E_z^{RE}\}. \end{aligned} \tag{3.2.6}$$

The same way $B_1^{-i,RE}$ is obtained $E_z^{i,RE}$ can be acquired and since the algorithm is approximating the contrast at every iteration the equation above can be solved for the total electric field during the receive state of the MRI. Thus at every iteration a better approximation of the receive phase,$\varphi_{-,n}$, can be acquired, under the condition that the algorithm converges to the true contrast.
The next step is to implement this into the cost functional and thus into the algorithm. The cost functional as seen in Equation (3.2.3) is updated to

$$F_{S,n}(w_j^{TR}, \varphi) = \eta_{S,n} \Sigma_j ||| B_{1,j}^{+TR}|e^{i\phi_+}e^{i\phi_-}e^{i\varphi_{-,n}} - G_S^+\{w_j^{TR}\} - B_{1,j}^{+i,TR}||_S^2. \tag{3.2.7}$$

When $\chi_n \to \chi$ converges the cost functional above converges to

$$\begin{aligned} F_{S,n}(w_j^{TR}) &= \eta_{S,n} \Sigma_j ||| B_{1,j}^{+TR}|e^{i\phi_+} - G_S^+\{w_j^{TR}\} - B_{1,j}^{+i,TR}||_S^2, \\ &= \eta_{S,n} \Sigma_j || B_{1,j}^{+TR} - G_S^+\{w_j^{TR}\} - B_{1,j}^{+i,TR}||_S^2. \end{aligned} \tag{3.2.8}$$

Which resembles the data cost functional in Equation (3.1.8) again. Further an extra benefit from this correction is that the approximated phase $\varphi_{-,n}$ is dependent on $w_{j,n}^{RE}$, the contrast source during the receive state, and not on the $w_{j,n}^{TR}$. This means that the update scheme from above stays exactly the same and the only new addition is after each update of the contrast the new $\varphi_{-,n}$ should be computed.

3.3 Overview of all the inputs and outputs

In Table 1 all the inputs needed to run the CSI algorithm are given. Instead of the back propagation as an initial guess, Equation (3.1.24), another initial guess for the contrast can be supplied. This can help the algorithm to converge in less iterations. Further the outputs of the algorithm are given as well. These include all the RF-fields during the transmit and receive state of the MRI scanner.

Table 1: In- and outputs of the algorithm

Inputs (name)	Inputs (symbol)	Outputs (name)	Outputs (symbol)
Measured data	$B_{1,j}^{+,TR}e^{\phi-}$	Complex transmit magnetic field in transmit	$B_1^{+,TR}$
Incident electric field in transmit	$E_{z,j}^{TR}$	Complex receive magnetic field during in receive	$B_1^{-,RE}$
Incident electric field in receive	$E_{z,j}^{RE}$	Total electric field in transmit	E_z^{TR}
Incident transmit magnetic field in transmit	$B_{1,j}^{+,TR}$	Total electric field in receive	E_z^{RE}
Incident receive magnetic field in receive	$B_{1,j}^{-,RE}$	The conductivity	σ
The number of antenna settings	j	The relative permittivity	ϵ_r
The spacing between data points	dx & dy	Complex transmit magnetic field in receive**	$B_1^{+,RE}$
The radius of the birdcage coil	r_{coil}	Complex receive magnetic field during in transmit**	$B_1^{-,TR}$
The radius of the RF-shield	R_{PEC}	SAR distribution**	SAR
The location of the antennas	ρ_s		
The magnitude of the static magnetic field	$\lvert B_0 \rvert$		
Initial guess for the contrast*	χ_0		
A mask of the object*	$\mathbb{D}^{obj}$		

* are optional inputs that might improve the reconstruction.
** are the optional outputs that are acquired through straightforward calculations.

3.4 Pseudo code

In this section a pseudo code is given to show how the algorithm will look like, this can be seen as an extension of the pseudo code in [12].

Algorithm 1: Transceive phase corrected CSI-EPT

- Compute w_0 and χ_0
for $n = 1$ *to maxIterations* **do**
  Step 1: Update the contrast sources
    - Compute $g_n^{w^{TR}}$ for $F_n^R(w_{n-1}, \chi_{n-1}, \varphi_{n-1})$
    - Compute the Polak-Ribière update direction
    - Compute the stepsize
    - Update the contrast source
  Step 2: Update E_z^{TR}
  Step 3: Update the contrast
    - Compute g_n^{χ} for $F_n^R(w_n, \chi_{n-1}, \varphi_{n-1})$
    - Compute the Polak-Ribière update direction
    - Compute the stepsize
    - Update the contrast
  Step 4: Update the receive phase
    - Solve for E_z^{RE} with χ_n
    - Compute $B_1^{-,RE}$
    - Extract the receive phase
  Step 5: Update the residuals and normalization factors
  if $F_n \leq$ *tolerance* **then**
    Stop
  end
end
- Compute remaining outputs

4 Matlab Simulations

Now that all the equations and algorithms are known it is time to put the CSI-EPT algoritm to the test and see how it performs. In this section the input data is generated by Matlab. In the section afterwards the input data will be generated by an FDTD solver called Sim4Life. This will also be used to validate the Matlab generated data. The main difference between the two simulations is that the data from Matlab is 2D and E polarized and the data from Sim4Life is 3D.
The Matlab simulation is used to test how the algorithm handles noise, truncation of k-space and different voxel sizes. This is done step by step in order to see where certain artifacts in the reconstruction come from. In the section of the Sim4Life results the same procedure of testing is done. This will give the most realistic scenario of data that comes from the scanner.

4.1 The contrasts

In addition to the different kind of tests a multitude of test objects are used. For both Matlab and Sim4Life these include a simple phantom as seen in Figure 4, a more complicated phantom as seen in Figure 5 and the head of a human model called Ella which is seen in Figure 6. This model is from the virtual family [27].
The simple phantom is used to show that the algorithm can reconstruct this the transceive phase input because the asymmetry of the phantom leads to the TPA to be invalid.
The values for the different compartments are shown in Table 2.

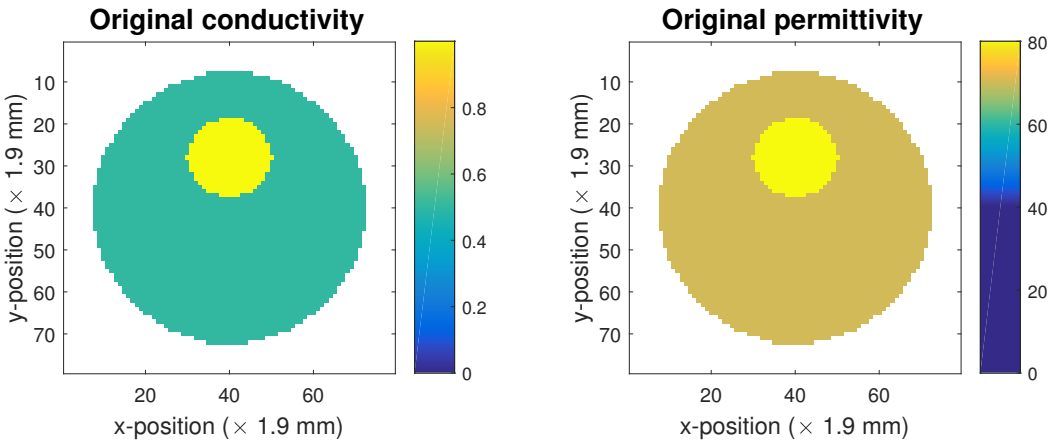

Figure 4: The structure of the simple phantom. On the left is the conductivity profile and on the right is the permittivity map.

Table 2: Conductivity and relative permittivity values for the first phantom at 128 MHz.

	Conductivity [S/m]	Relative permittivity	Radius [cm]
Inner Compartment	1	80	2
Outer Compartment	0.5	70	6.5

The more complicated phantom shows better how the algorithm handles multiple structures with different conductivities and permittivities and how well it reconstructs boundaries that are close together. The values for the different compartments of the second phantom are shown in Table 3. And since this reconstruction method needs to work on human tissue, a 2D slice of Ella's brain is used to test how the final result will look like. Finally, the electrical property values of Ella are given in Table 4.

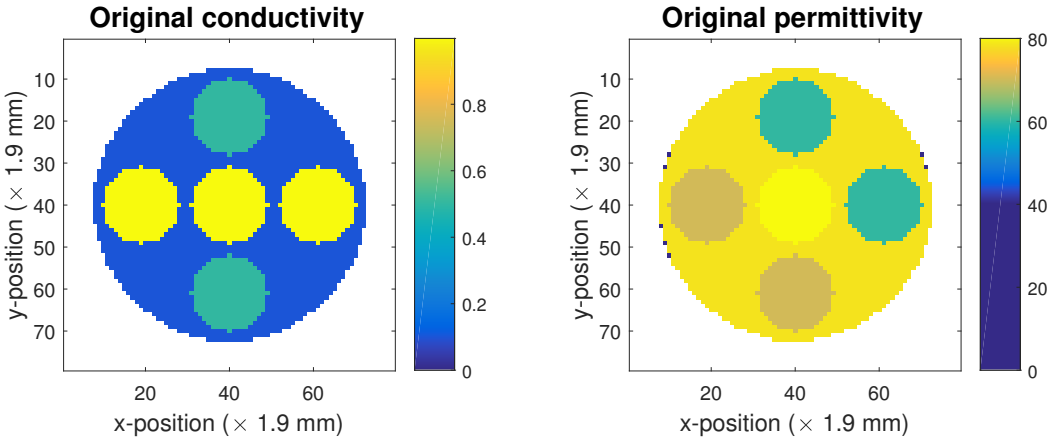

Figure 5: The structure of a more complicated phantom. On the left is the conductivity profile and on the right is the permittivity map.

Table 3: Conductivity and relative permittivity values for the second phantom at 128 MHz.

	Conductivity [S/m]	Relative permittivity	Radius [cm]
Top Compartment	0.5	60	2
Left Compartment	1	70	2
Middle Compartment	1	80	2
Right Compartment	1	60	2
Bottom Compartment	0.5	70	2
Background	0.1	78	6.5

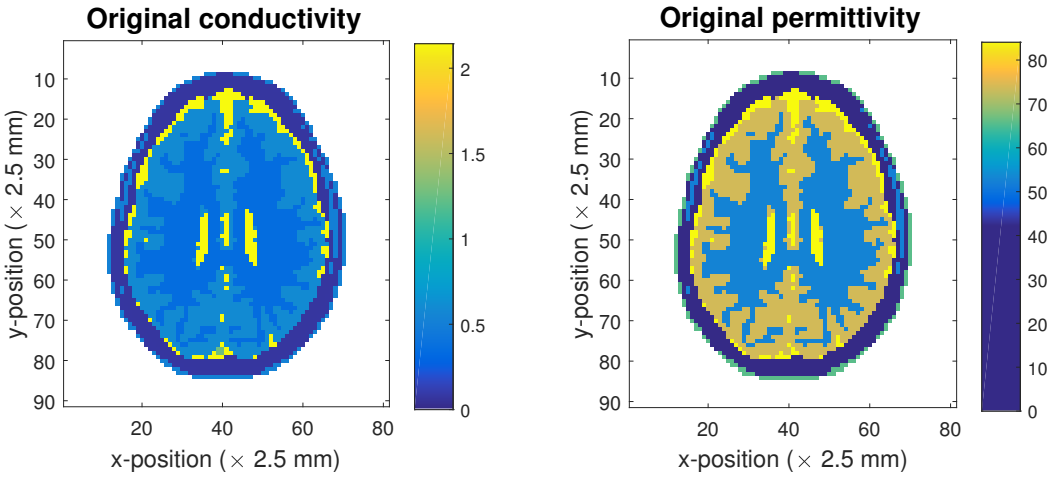

Figure 6: A slice of Ella's brain. On the left is the conductivity profile and on the right is the permittivity map.

Table 4: Conductivity and relative permittivity values for Ella at 128 MHz.

	Conductivity [S/m]	Relative permittivity
White matter	0.342	52.53
Gray matter	0.587	73.52
CSF	2.14	84.04

4.2 2D antenna setup

With the three different contrasts known the next thing that is looked at is the geometry of the MRI. For both the Matlab and Sim4Life simulations the same antenna setup is used. The specifications of these are given in Table 5.

Table 5: 2D antenna setup parameters

Parameter	Value	Unit
Coil radius	35.2	[cm]
RF-shield radius	37.15	[cm]
Number of legs	16	

In Figure 7 the resulting 2D antenna setup can be seen, including the mirror sources that are used to numerically implement the RF-shield.

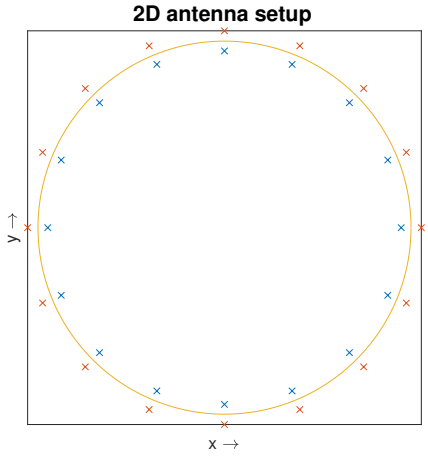

Figure 7: The simulated 2D antenna setup. The blue crosses indicate the true line sources whereas the red crosses show the locations of the mirror sources. The location of the RF-shield is indicated by the orange circle.

4.3 The incident fields

The first thing that can be tested is how the incident fields look like with this setup. This can be shown for all three modes, quadrature and two linear modes. For the electric fields the expected outcome would be a minimum in the center of the coil, and no field where the RF-shield is located. In the quadrature mode the field should be circularly polarized and for the linear modes the fields, as the name suggests, should be linearly polarized. The resulting incident electric fields can be seen in Figure 8.

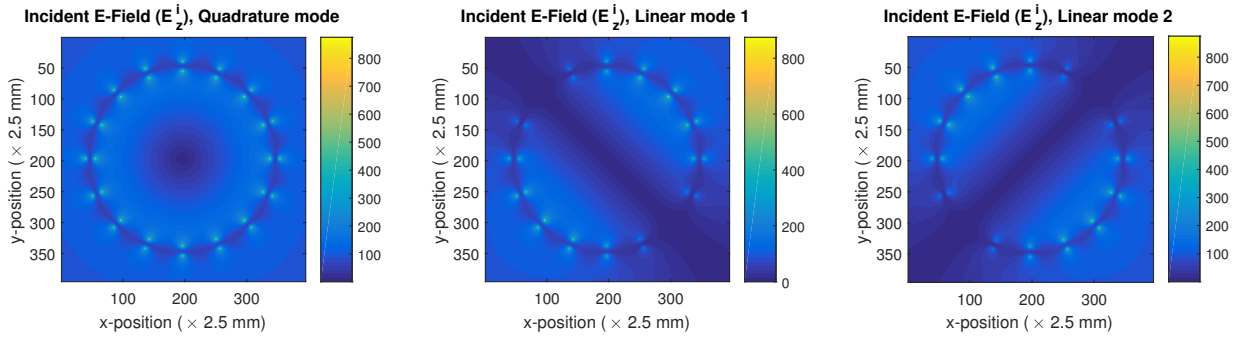

Figure 8: The magnitude of the incident electric fields $|E_z^{i,TR}|$. On the left is the quadrature mode, then in the middle and on the right are the two linear modes.

It can clearly be seen that the field goes to zero where the RF-shield is implemented. There are a few advantages to implementing such an RF-shield, the first is of course that this is more realistic. As there is a shield in the

physical MRI as well, this improves the qualitative aspect of the fields (i.e. the field lines represent a more realistic case). This is especially the case when the object is not precisely in the center of the coil.
However, also the quantitative aspect of the fields are improved. For a certain current running through the line sources the corresponding fields match the physical MRI better. This is relevant for the reconstruction because the MRI measures the total magnetic fields, whereas the algorithm is based on the scattered fields.
A zoomed in version of the incident electric fields is given in Figure 9. The zoomed in versions are given in order to compare them with the incident magnetic fields $B_1^{+i,TR}$. For these fields it is beneficial if they are as homogeneous as possible. The results of this are seen in Figure 10.

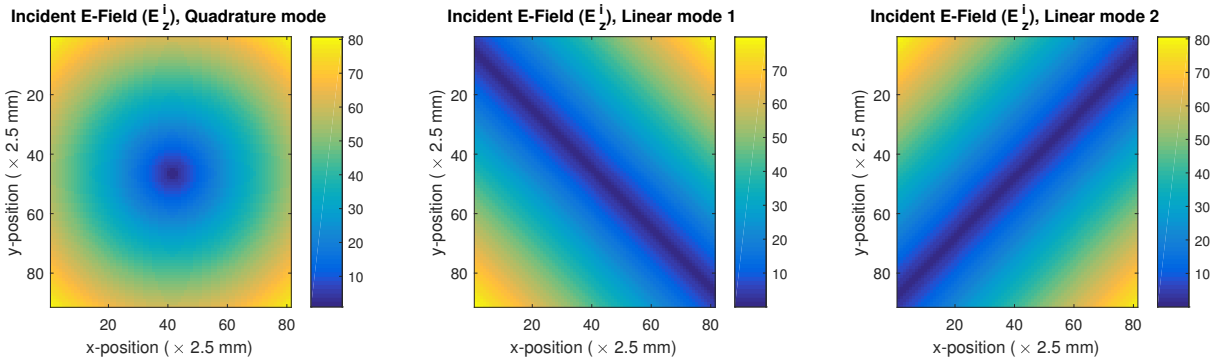

Figure 9: The magnitude of the incident electric fields $|E_z^{i,TR}|$ zoomed in. On the left is the quadrature mode, then in the middle and on the right are the two linear modes.

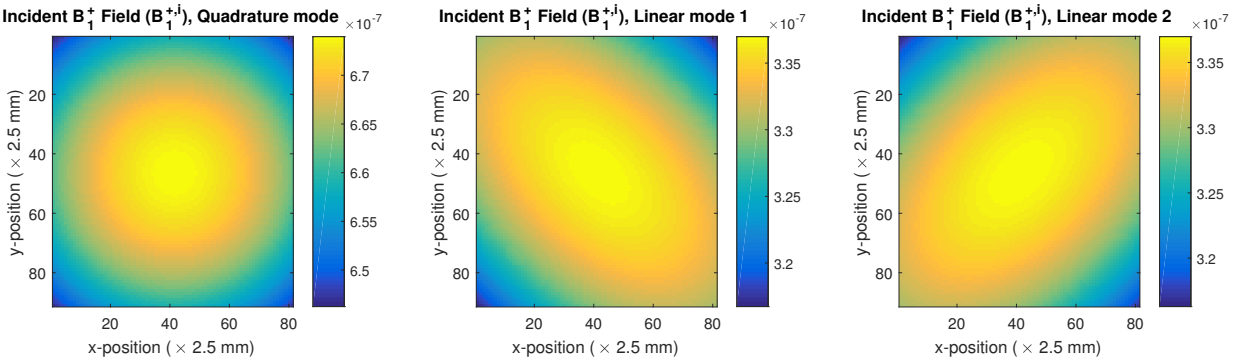

Figure 10: The magnitude of the incident magnetic fields $|B_1^{+i,TR}|$ zoomed in. On the left is the quadrature mode, then in the middle and on the right are the two linear modes.

4.4 Standard CSI-EPT reconstructions

With all the fields constructed it is time to see how well the algorithm can reconstruct the contrast. The first thing that needs to be checked is if the algorithm without the transceive phase correction is able to output good results. This has of course been shown in [12] but is still good to check.
In the following figures the conductivity and permittivity are take separately to be compared with different reconstruction settings. For the algorithm without the transceive phase correction the figures are ordered according to Table 6.

Table 6: Order of figures for the algorithm without transceive phase correction

The original	Perfect input reconstruction	Noisy input reconstruction
Noisy input reconstruction with TV reconstruction (Haffinger)	The wrong incident fields amplitude is halved	The wrong incident fields a global phase shift is added

Here the original means just that, the original conductivity and permittivity maps as shown in Section 4.1. With perfect input it is meant that there is no noise added to the input data and the full k-space is supplied, this is just used to test the algorithm and check if there are no bugs in the code. For noisy input an SNR of 70 is chosen for both the amplitude and phase. This will show how the algorithm handles noise and how the SNR

of the input propagates through to the reconstructed contrast.
Now there are two different TV regularization options, this has to do with the steering parameter from equation (3.1.43). A steering parameter was proposed in [28].

$$\delta_n^2 = (\int_x dx)^{-1} \int_x |\nabla \chi_{n-1}|^2 dx. \tag{4.4.1}$$

Whereas one for data from an MRI scanner was proposed as [17]

$$\delta_n^2 = \frac{F_s}{F_{D,n}} \triangle^2, \tag{4.4.2}$$

here $\triangle^2$ is the reciprocal of the meshsize. Of course there are many more choices possible here, as explained before it really depends on the kind of problem that is being minimized. For the reconstructions with Matlab data the steering parameter from Equation (4.4.1) was chosen, for the Sim4Life data and the measured data in the next chapters the steering parameter from Equation (4.4.2) gave better results.
As for the last two reconstruction they were done by supplying the wrong incident fields to the algorithm to see how sensitive it is to this. First the amplitude was halved and the second reconstruction was done by giving a global phase shift to the incident fields. The results are shown in Figure 11 and Figure 12.

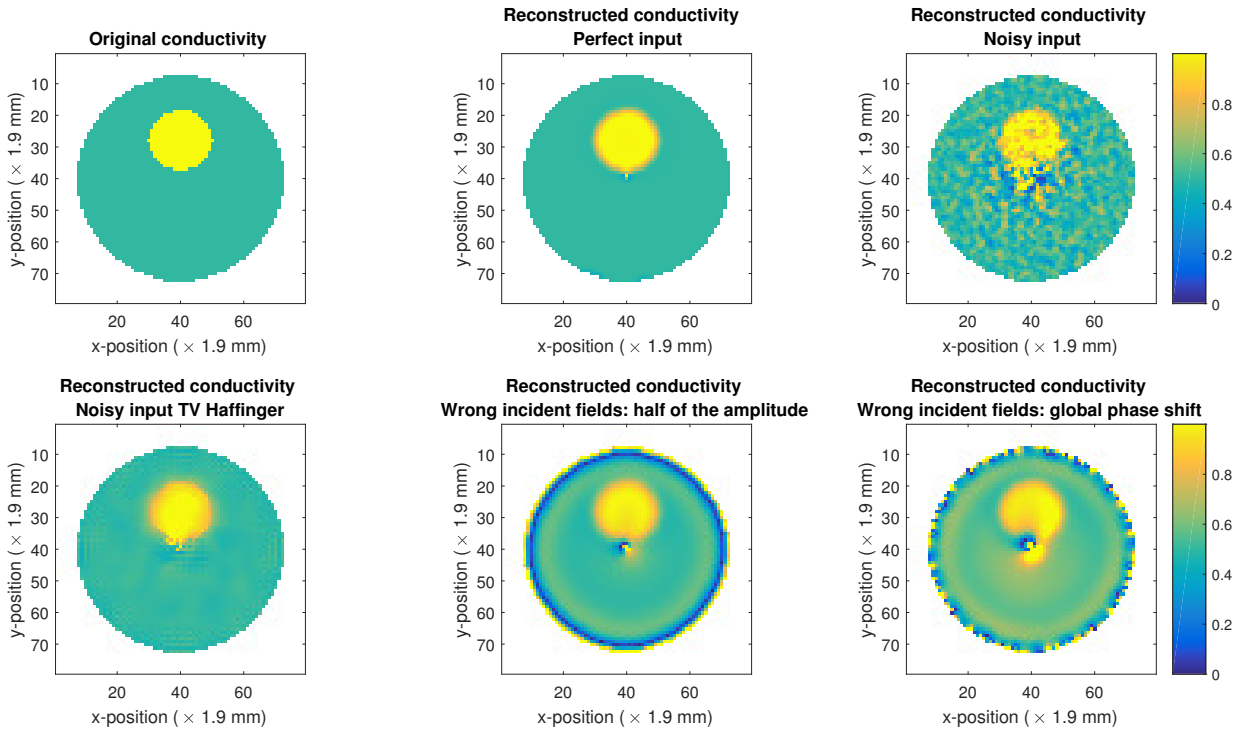

Figure 11: Conductivity profiles of the simple phantom. In the top row are from left to right the original profile,the reconstruction with perfect input and the noisy reconstruction. In the bottom row are the TV regularized noisy reconstruction and two reconstruction with the wrong incident fields.

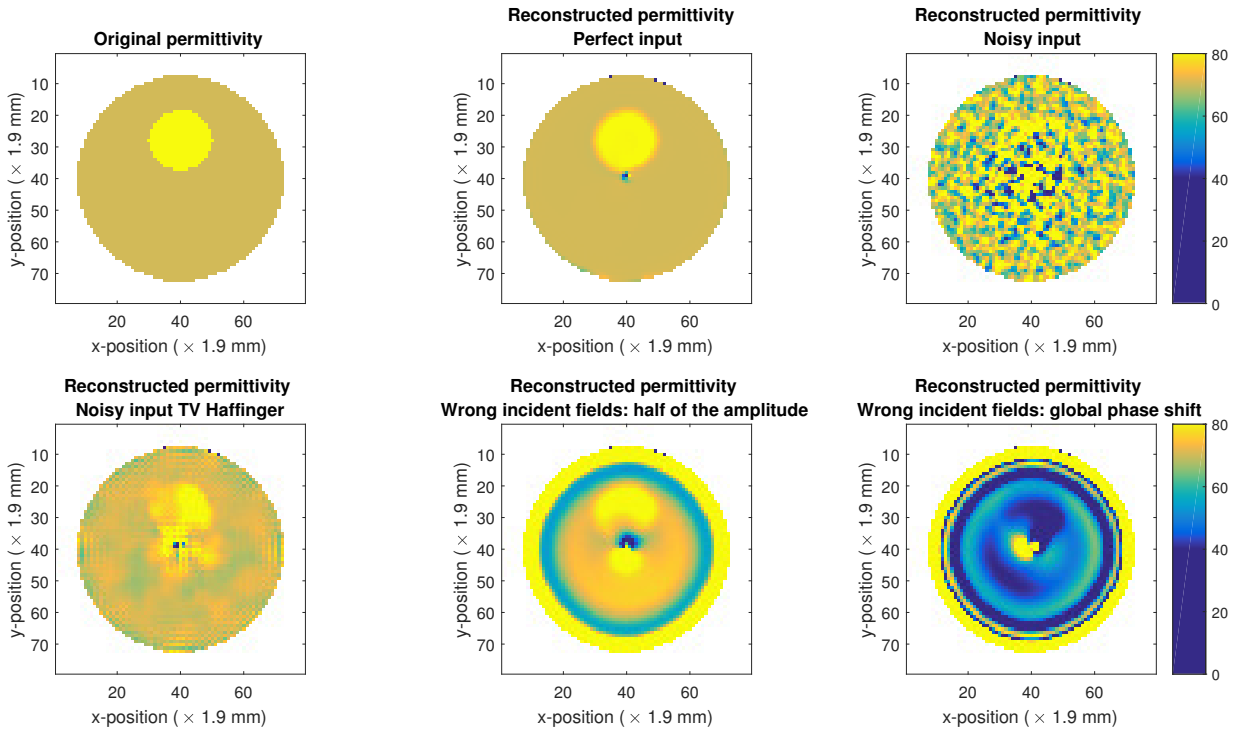

Figure 12: Permittivity profiles of the simple phantom. In the top row are from left to right the original profile,the reconstruction with perfect input and the noisy reconstruction. In the bottom row are the TV regularized noisy reconstruction and two reconstruction with the wrong incident fields.

The first thing to notice from the reconstruction in Figure 11 and Figure 12 is that when the perfect input is given to the algorithm it works very well. The next phenomenon is that the noise added to the input has a larger effect on the permittivity reconstruction compared with the conductivity reconstruction. This makes reconstruction the permittivity more difficult. However, the precision of the reconstructed conductivity scales linearly with the transmit frequency whereas the precision of the reconstructed permittivity scales quadratically [29]. Thus when a reconstruction is done with a static magnetic field strength of 7T instead of 3T the permittivity reconstruction will benefit more than the conductivity reconstruction.
The TV regularization improves the reconstruction significantly, especially the permittivity resembles the original a lot better.
Finally from the last two figures it is seen that supplying the algorithm with the wrong incident fields ruins the reconstruction. The conductivity reconstruction is slightly less sensitive to the wrong amplitude than the permittivity, however for both the global phase shift does not give good results. This is because the global phase shift comes back into the contrast and part of the conductivity is translated to permittivity and the other way around.
The reconstructions of the second phantom and Ella are in the appendix. Here the same order of figures hold as shown in Table 6.
From the results in Figure A.1 and Figure A.2 the same conclusion can be drawn with respect to the simple phantom. The only object left is Ella's brain, again the same order of figures is in place.
In these set of reconstructions, Figure A.3 and Figure A.4, again similar conclusions can be drawn as with the simple phantom. The aspect to notice here however is that noise makes it more difficult to reconstruct the fine structures in the brain. What can be seen is that the structures are smoothed out more than one would like them to be.

4.5 Transceive phase assumption compared to transceive phase corrected

In this section the effect on the reconstructions of the TPA is tested and compared to the reconstructions when using the transceive phase correction algorithm. First the error between the transmit phase and the TPA for different static magnetic field strengths for the first phantom are quantified as seen in Figure 13. The error is defined as

$$\varepsilon_{TPA} = \phi_+ - \frac{\phi_\pm}{2}. \tag{4.5.1}$$

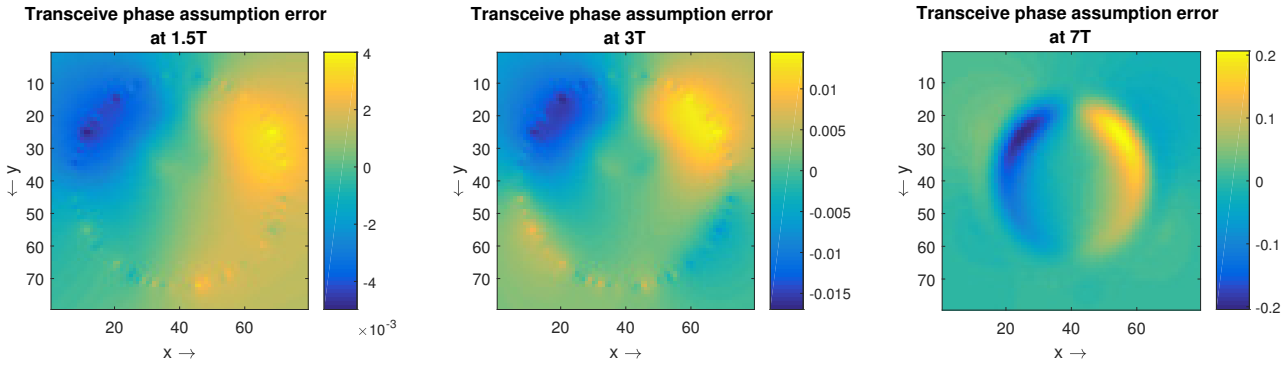

Figure 13: The error between the transmit phase and the TPA at different static magnetic field strengths for the first phantom. On the left is 1.5T in the centre is 3T and on the right is 7T.

From Figure 13 it is clear that the stronger the static magnetic field the larger the error becomes. This is also what follows from Section 2.5, because as the static magnetic field strength goes up the amplitude of the scattered fields will grow too [30]. This makes the TPA less valid [20].
In Figure 14 and Figure 15 the error can be seen that is due to the TPA at 3T. On the right of the figure the transceive phase corrected reconstruction is shown.

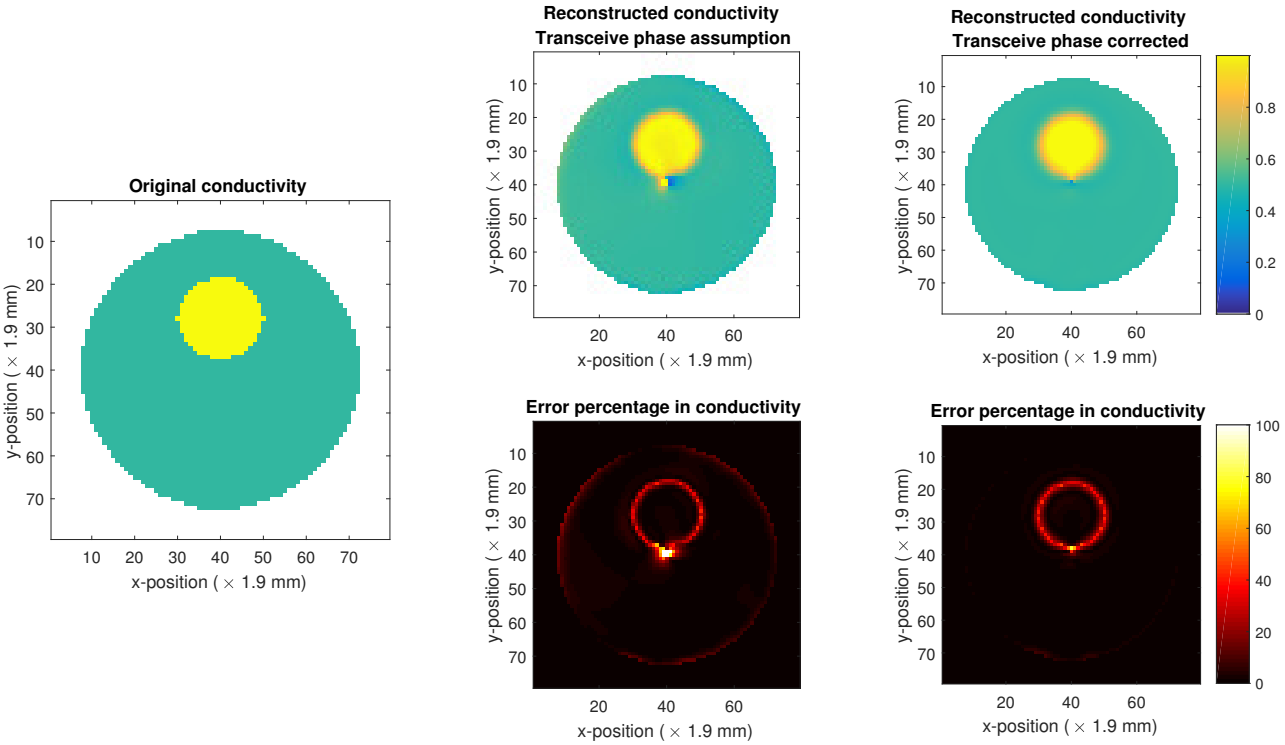

Figure 14: On the left is the original conductivity. In the top middle figure the reconstructed conductivity is shown by using the TPA, with underneath that the error compared to the original. On the right is the transceive phase corrected reconstructed conductivity, with underneath it the error compared to the original. The static magnetic field strength is 3T.

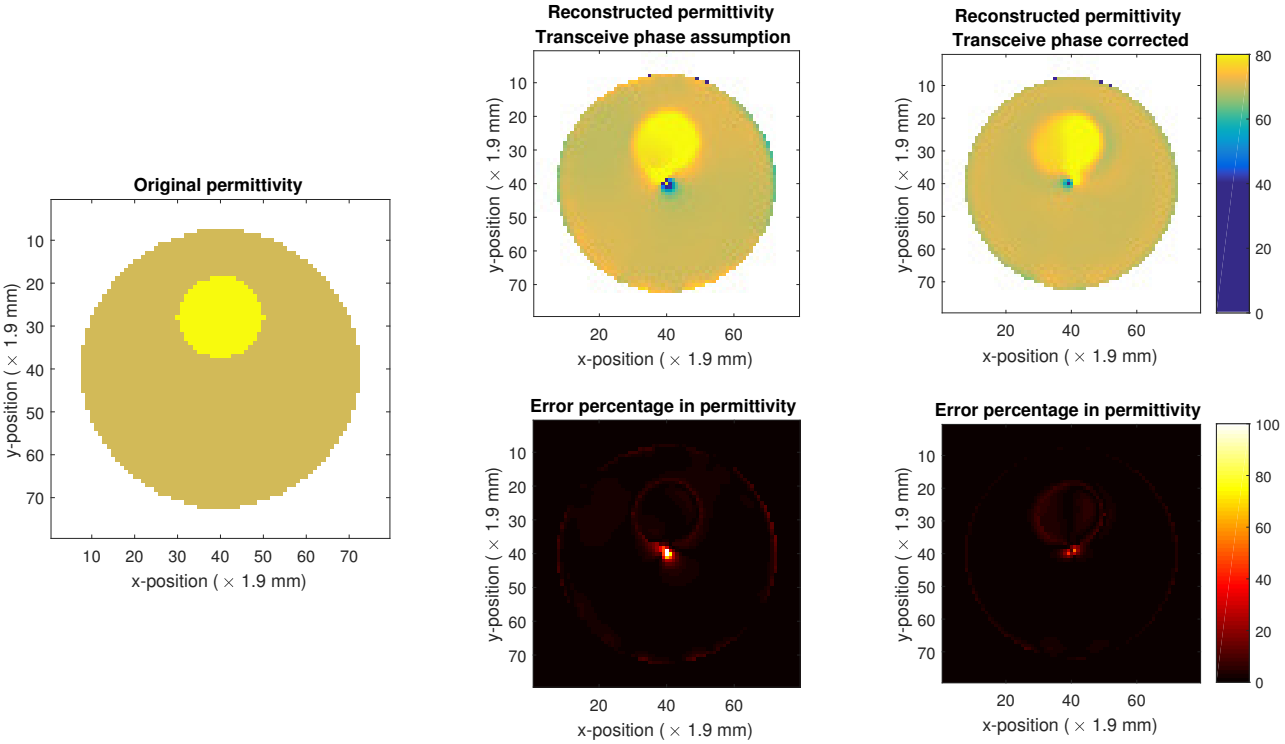

Figure 15: On the left is the original permittivity. In the top middle figure the reconstructed permittivity is shown by using the TPA, with underneath that the error compared to the original. On the right is the transceive phase corrected reconstructed permittivity, with underneath it the error compared to the original. The static magnetic field strength is 3T.

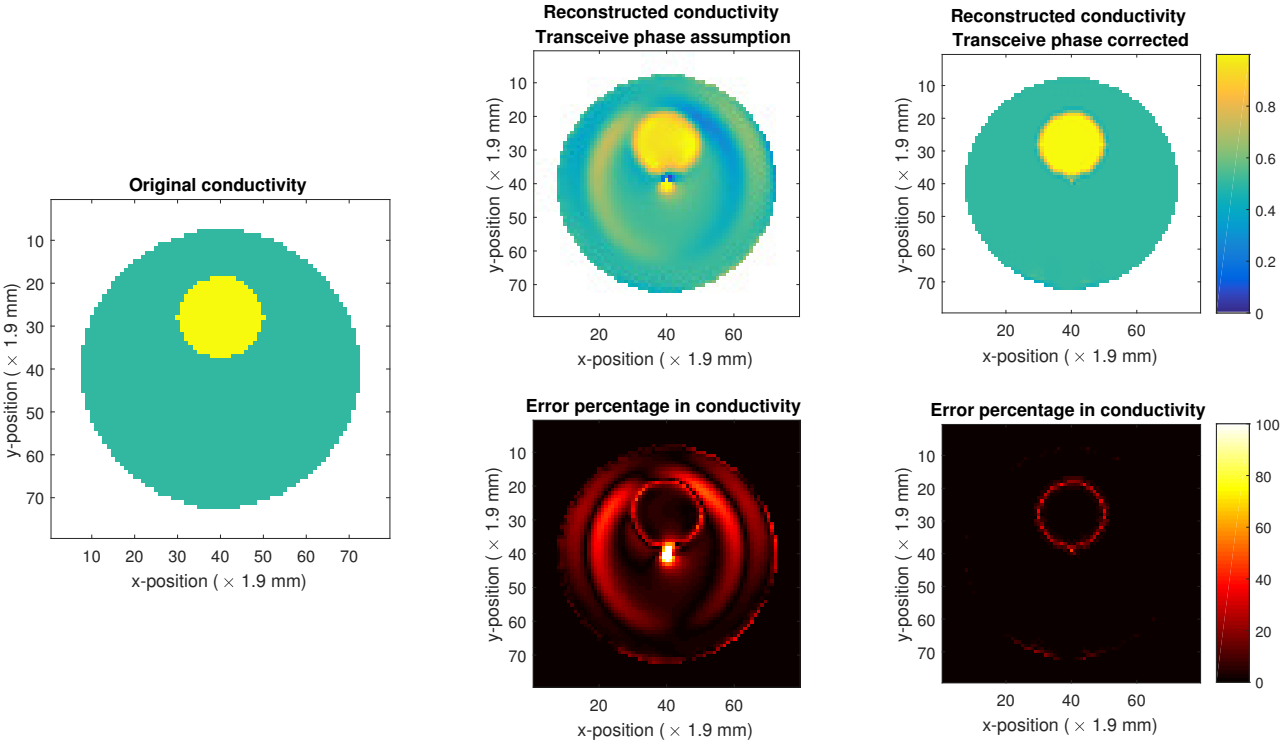

Figure 16: On the left is the original conductivity. In the top middle figure the reconstructed conductivity is shown by using the TPA, with underneath that the error compared to the original. On the right is the transceive phase corrected reconstructed conductivity, with underneath it the error compared to the original. The static magnetic field strength is 7T.

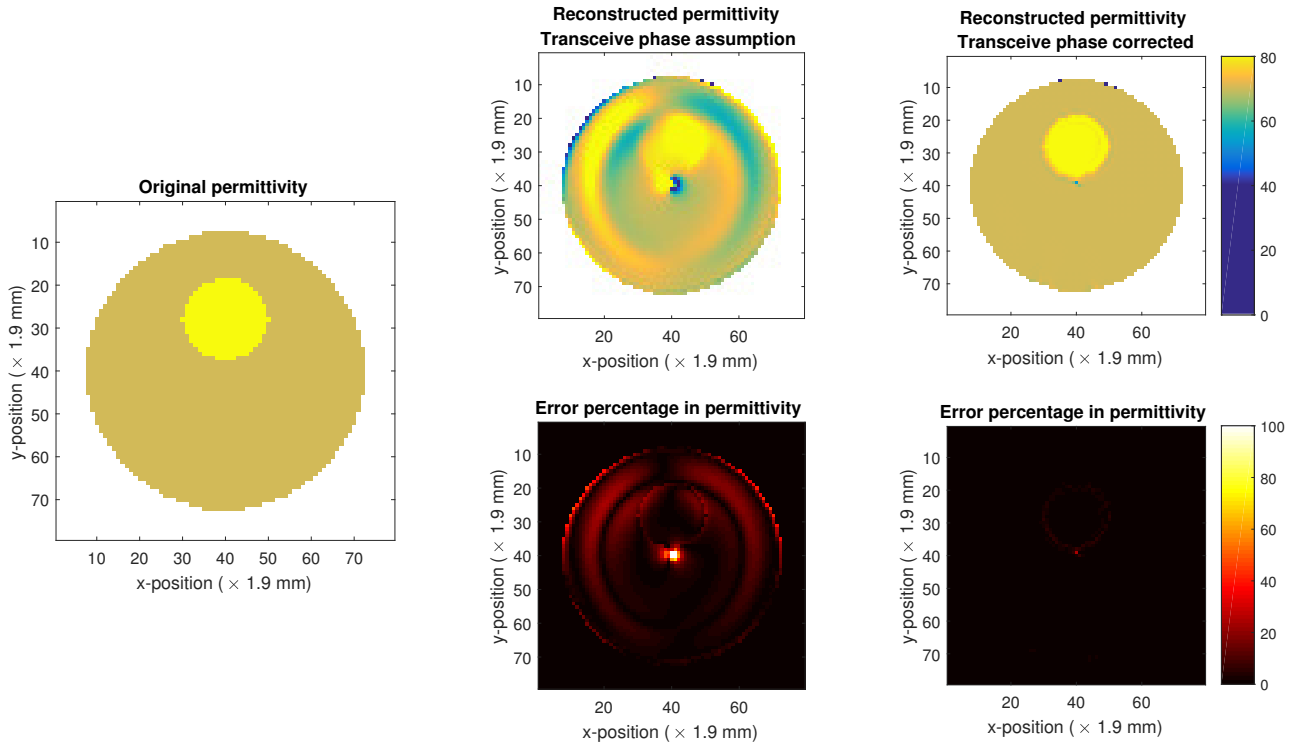

Figure 17: On the left is the original permittivity. In the top middle figure the reconstructed permittivity is shown by using the TPA, with underneath that the error compared to the original. On the right is the transceive phase corrected reconstructed permittivity, with underneath it the error compared to the original. The static magnetic field strength is 7T.

From Figure 14 and Figure 15 it can be seen that the transceive phase correction shows some small improvement with respect to using the TPA. The same reconstructions were also done with a static magnetic field strength of 7T, these are shown in Figure 16 and Figure 17.
From Figure 16 and Figure 17 it can be concluded that at higher static magnetic field strengths the TPA is not accurate enough and the transceive phase correction must be done to get better results. In the appendix are the 7T reconstructions for the other phantom, Figure A.5 and Figure A.6, and Ella, Figure A.7 and Figure A.8. In Figure 18 the mean absolute error is plotted against the field strength, for both the conductivity and permittivity, with and without noise. The noisy reconstructions were done with SNR 70. Normally the higher the static magnetic field strength is the better the SNR becomes (i.e. there is more signal compared to the same amount of noise), this was not taken into account in this reconstruction.

From Figure 18 it can be seen that at higher fields strengths the TPA is the main contributor to the error in the reconstruction. This error disappears when the transceive phase correction is done. Furthermore, at higher field strengths the conductivity and permittivity are reconstructed better. This is due to the higher curvature of the measured field at higher field strengths (i.e. the conductivity and permittivity have a bigger influence on the measured field) [29],[30]. The noise added also has less effect on the reconstructions at higher field strengths for the same reason. From the top right plot it can thus clearly be seen that at lower field strengths the noise is the dominant contributor of the error in the reconstruction and at the higher field strength the error is due to the TPA.

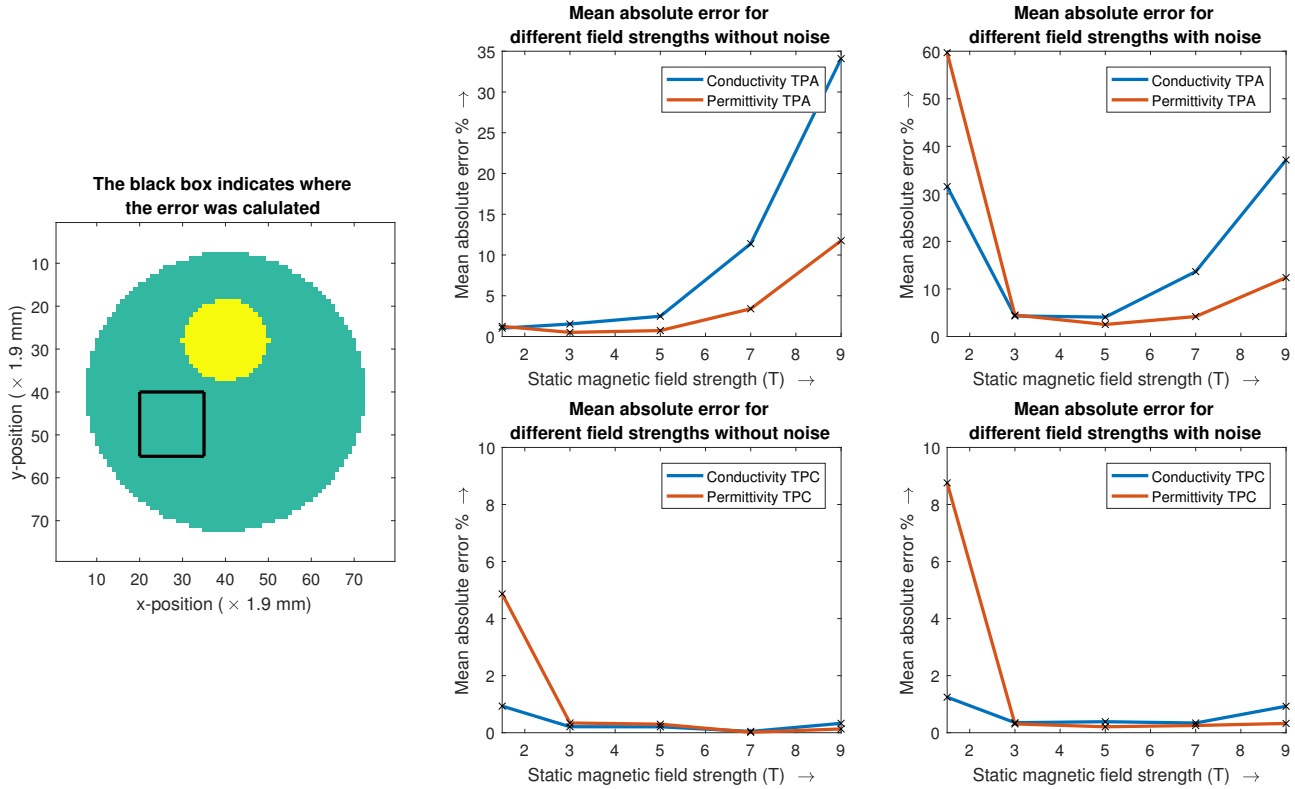

Figure 18: On the left the area is indicated by the black box over which the error is calculated. In the top row are the errors plotted for the TPA, the left is without noise and the right is with SNR 70. In the bottom row are the errors plotted for the transceive phase correction (TPC),the left is without noise and the right is with SNR 70. The blue line is the conductivity and the red line is the permittivity.

4.6 Transceive phase corrected CSI-EPT reconstructions at 3T

From the previous section it is clear that the reconstructions with the transceive phase correction show a significant improvement, especially for the higher static magnetic field strengths. For the reconstructions in the following figures the order is as seen in Table 7.

Table 7: Order of figures for the algorithm without transceive phase correction

The original	Noisy input reconstruction	Noisy input reconstruction with TV reconstruction (Haffinger)
Voxels resized to 3mm by 3mm	Truncated k-space input	Noisy input with voxels resized to 3mm by 3mm and truncated k-space with TV reconstruction (Haffinger)

All reconstructions from here on out are done with the transceive phase as input, because this is a more realistic scenario. Plus it would not make sense to test a transceive phase correcting algorithm without the transceive phase in there. Here the first three reconstructions were already discussed with the previous algorithm, thus the attention is focused on the fourth reconstruction. This reconstruction tests the algorithm when the data is resized to another grid. This will force the boundaries of the contrast to be inside the voxels rather than in between the voxels. To acquire this input data the $B_1^{+,TR}$ with transceive phase is upscaled to a finer grid size and then downscaled again to the desired voxel size. For all these the new voxel size becomes 3mm by 3mm.
After this the k-space is truncated to see the effect of the sampling that is done inside the MRI. In a realistic situation the object would be continuous and then discretized by the MRI measurement. To mimic this effect the input that is again scaled up to a very fine grid. It is then Fourier transformed to get the k-space. Here the higher frequencies are set to zero.
Finally the last reconstruction is as close as the 2D Matlab simulation will get compared to the actual measurements. All the previous tests are put into one, meaning noise is added as well as the voxel size being set to 3mm by 3mm and the k-space is truncated. The order of the operations is as follows: first the k-space is truncated and afterwards the noise is added, otherwise the noise would be truncated which would beat that purpose of the

simulation. Furthermore, in a normal MRI measurement the SNR would go up if larger voxels were sampled because there would be more signal and the same amount of noise. This was not taken into account in these simulations.

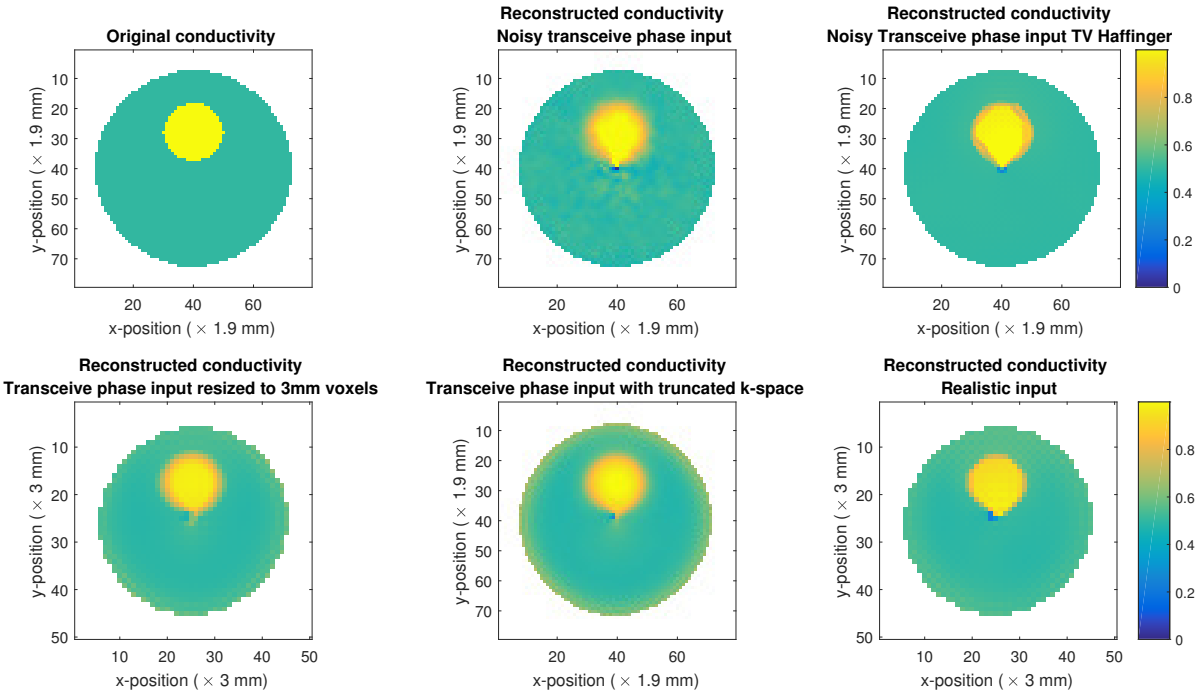

Figure 19: Conductivity profiles of the simple phantom, all reconstructed with the transceive phase. In the top row from left to right are the original profile, the noisy input reconstruction and the TV regularized reconstruction. In the bottom row are the reconstructions with the resized voxels, k-space truncation and the most realistic scenario

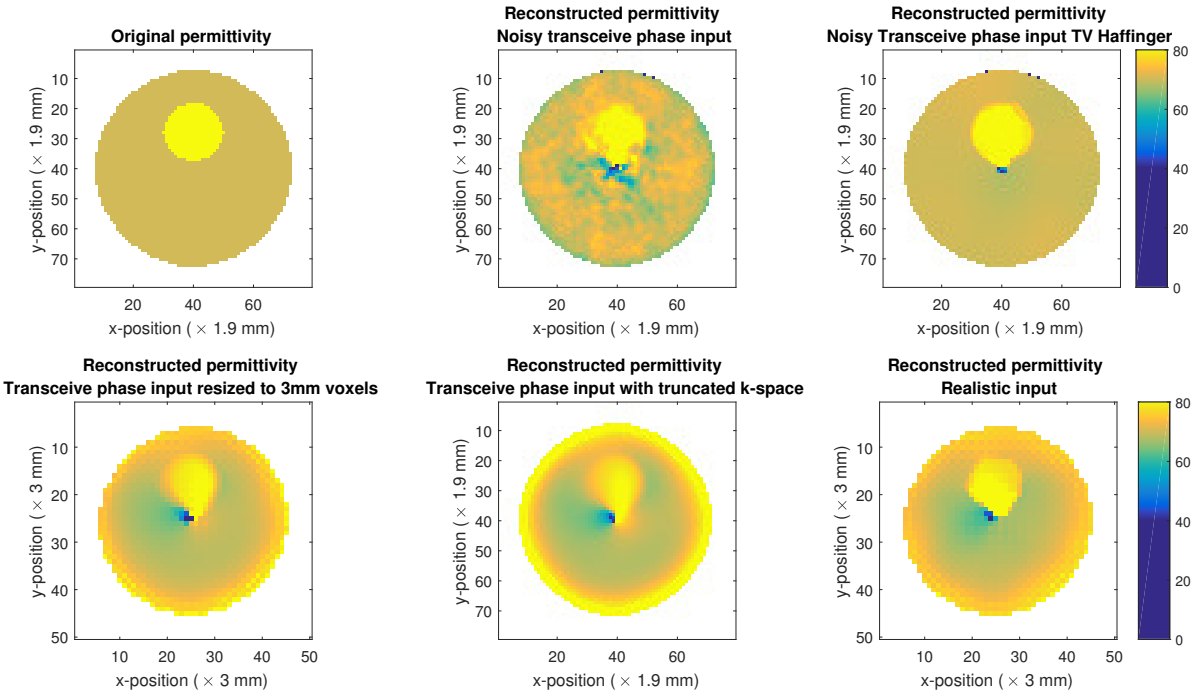

Figure 20: Permittivity profiles of the simple phantom, all reconstructed with the transceive phase. In the top row from left to right are the original profile, the noisy input reconstruction and the TV regularized reconstruction. In the bottom row are the reconstructions with the resized voxels, k-space truncation and the most realistic scenario.

From Figure 19 and Figure 20 similar conclusions can be drawn with respect to the noisy input and the TV regularization reconstructions as without the transceive phase correction algorithm. From the bottom left reconstruction it is seen that resizing of voxels is not a problem. The truncation of k-space does have a small impact at the boundary of the two compartments and at the edge of the phantom. This is because the higher frequencies that are now truncated are needed for sharper edges. The most realistic reconstruction shows that putting everything together is still not a problem for the algorithm.
Again the reconstruction for the second phantom and Ella are found in the appendix. The results from Figure A.9 and Figure A.10 show similar results as the simple phantom did. A thing to notice in both reconstructions is that often the voxels in the center are incorrect. This is due to the fact that in Equation (3.1.23) the total electric field is in the numerator of the equation. When looking back at Figure 8 the center of the incident electric field is a minimum that goes to zero. This causes an instability in those few voxels in the center.
With the TV regularization however it can happen that when the 2-norm is minimized that this part of the contrast gets smoothed out resulting in either a correct reconstruction when the surrounding voxels have the same conductivity and permittivity as the center voxels. Or it causes the structure in the center to be smoothed out, this can be seen in the reconstructions of Ella's brain, Figure A.3 and Figure A.4 are good examples of this.
In Figure A.11 and Figure A.12 Ella's brain is reconstructed and again due to noise and smoothing of the TV regularization the boundaries get smoothed out and a lot of fine details are lost in the process.
Until now only the complete maps have been shown, to get an idea about the difference between the two different TV regularization parameters a line profile can give a better feeling on how it behaves. These profiles are only shown for the last scenario from Figure 19,20 and Figure A.9 to Figure A.12. Plus the line profile is shown when there is no TV regularization, to see the full scale effect it has on the reconstruction. In Figure 21, Figure A.13 and Figure A.14 these line profiles are visible.

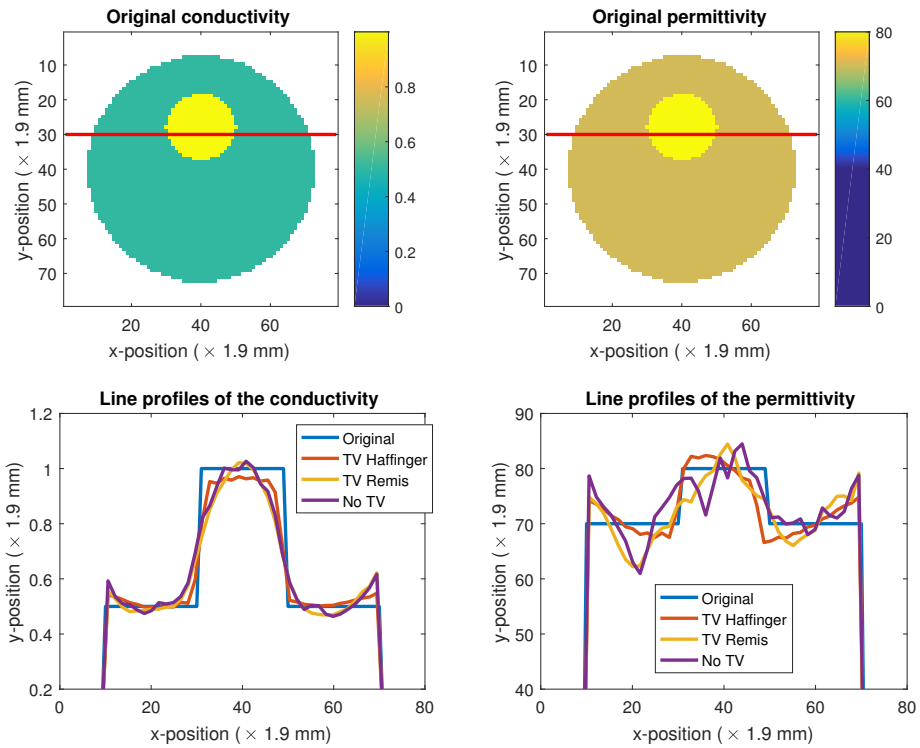

Figure 21: The line profiles of the simple phantom. The red line in the original images show where the profile was examined.

From these line profiles it can be concluded that the TV regularization does help with reducing the noise on the reconstruction. However as can be seen in Figure 21 and Figure A.13 the reconstruction does not jump from one value to another instantly at the boundary. It takes 2 or 3 voxels to get to the desired value. This results in fine structures to be either skipped or underestimated as can be seen in Figure A.14. This is due to the minimization of the 2-norm which smooths the contrast. And one last thing to keep in mind with these line profiles is that the reconstructions were on a 3mm by 3mm grid whereas their originals are not. This can make it so that the jump at the boundary happens a voxel too early or too late.

4.7 $B_1^{-,RE}$ reconstruction

With all the reconstructions of the contrast done it is also interesting to look at how well the algorithm reconstructs the $B_1^{-,RE}$, since this has never been done before. The reconstruction is shown for the two phantoms and Ella in the most realistic simulation setting. The results can be seen in Figure 22 and in the Appendix in Figure A.15 and Figure A.16.

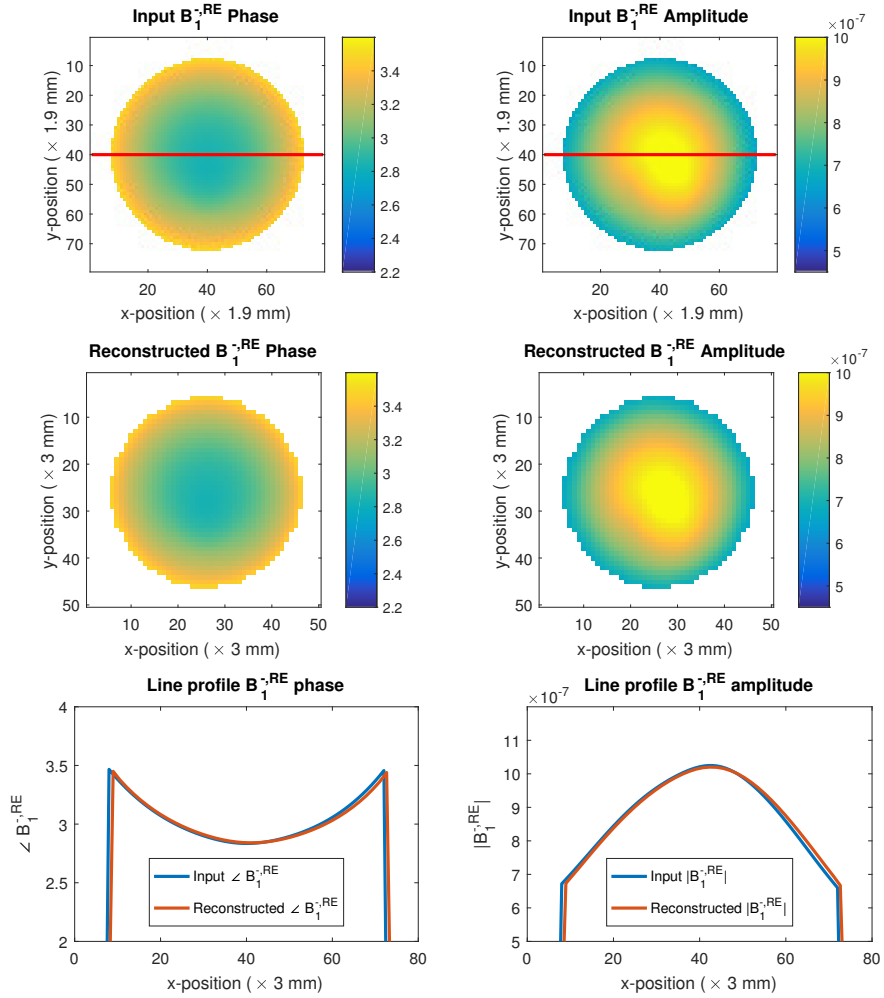

Figure 22: The $B_1^{-,RE}$ reconstruction for the simple phantom. In the top row are the input phase and amplitude. In the middle are the reconstructed phase and amplitude and in the bottom row are the line profiles taken at the location of the red line.

From these figures it is clear that the input $B_1^{-,RE}$ field is in line with the reconstructed one. This accounts for both qualitatively and quantitatively as seen by the line profiles. In the next chapter of this work the reconstructions from Sim4Life are discussed.

5 Sim4Life Simulations

In this chapter the main goal is to get a step closer to the real measurements. The Matlab reconstructions shown before are all for 2D data, whereas Sim4Life is a 3D FDTD simulation program. The first thing that will be done is comparing the field distributions that come from the Matlab simulation with those that Sim4Life outputs. After this comparison the reconstructions will be shown for the same objects as in the previous chapter, except for Ella, a simulation was done with Duke instead. However, the true conductivity and permittivity profiles were not available thus these results were omitted from this report.

5.1 Setup Sim4Life

In Sim4Life the birdcage coil in Figure 23 was tuned to 128MHz, the Larmor frequency for hydrogen atoms at 3T. Around the birdcage coil is the RF-shield and inside the coil is the bore. The bore is a plastic encapsulation of the coil. The objects that were simulated in this coil setup were placed in the centre of the coil (i.e. the centre of the object coincided with the centre of the coil). The reconstructions were also done with the data from the centre slice, unless otherwise stated.

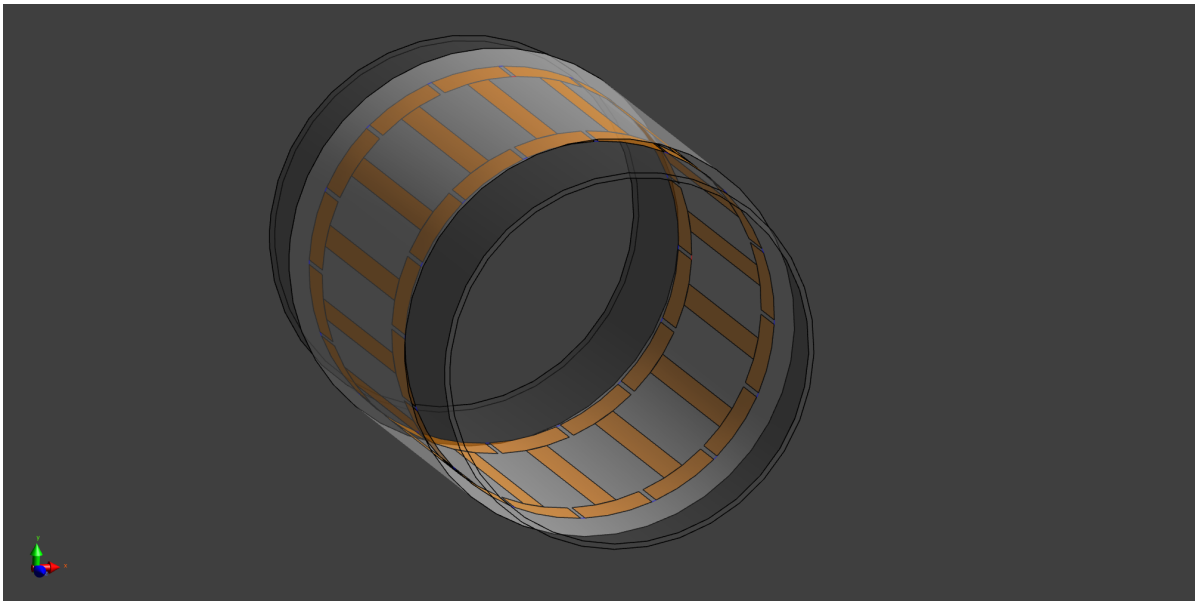

Figure 23: The coil setup in Sim4Life. This setup includes a tuned birdcage coil, an RF-shield and a bore.

The parameters that were used for the geometry of the setup are shown in Table 8.

Table 8: Geometry parameters of the setup in Sim4Life.

Parameter	Value	Unit
Coil radius	35.2	[cm]
RF shield radius	37.15	[cm]
Bore radius	35	[cm]
Coil length	44	[cm]
Number of legs	16	

Finally, the simulations were run until Sim4Life stopped them, which it does if the difference between iterations is smaller than -30dB. This was done to be sure that the simulation was converged.

5.2 Field distributions in Sim4Life

The first assumption that needs to be substantiated is the assumption that the electromagnetic field is two-dimensional and E-polarized in the z-direction in the centre plane of MRI. This can be seen in Figure 24.
As can be seen in Figure 24 the z component of the magnetic field is negligible compared to the x and y components. The same holds for the x and y components of the electric field with respect to the z component. Thus the assumption in Equation (2.2.1) seems to be valid, the only problematic point is the middle of the electric field. Here the amplitude of the z component has a comparable amplitude as the x and y components

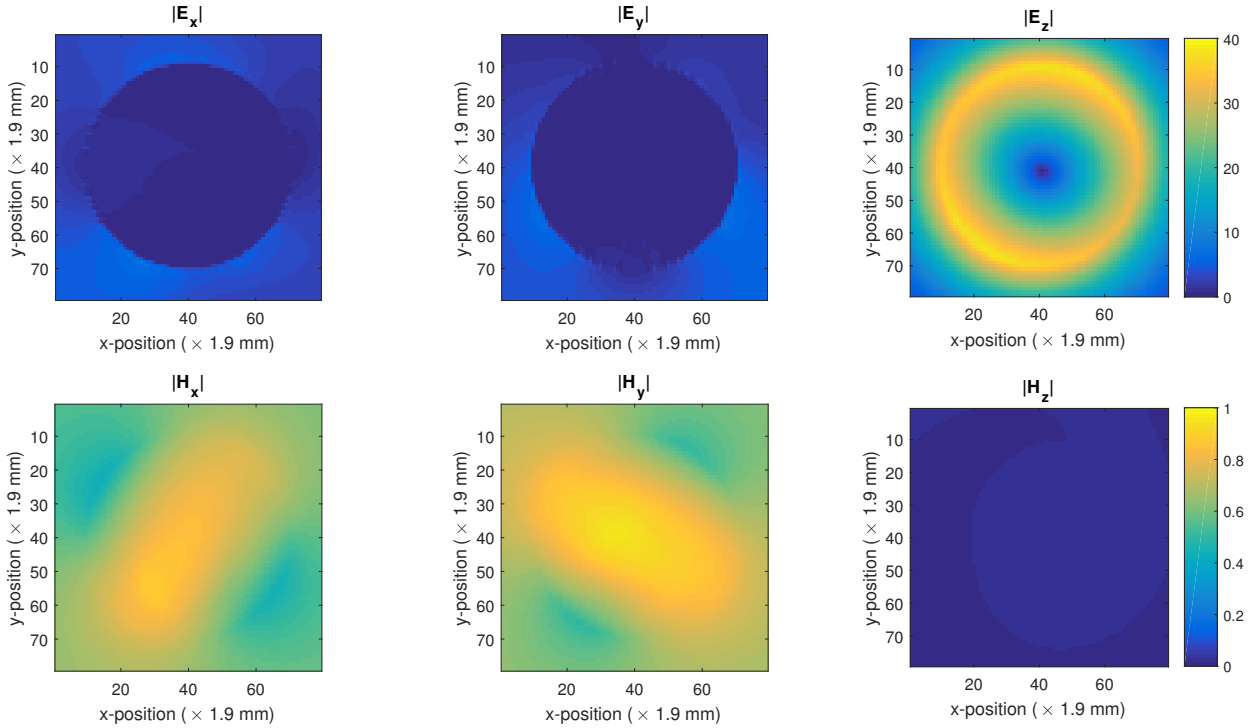

Figure 24: In the top row are the amplitudes of the electric field in the x,y and z-direction all on the same color scale. In the bottom row are the amplitudes of the magnetic field in the x,y and z-direction all on the same color scale. This is that data from the centre slice of the MRI.

of the electric field.
The following thing to verify is how well the 2D simulation from Matlab corresponds with the 3D simulation from Sim4Life. For this the field distributions of the second phantom are shown, because the second phantom has a larger scattered field and thus a more complex field distribution. In Figure 25 the B_1^+ amplitudes are shown for the quadrature and the linear settings.
As can be seen in Figure 25 the amplitudes of the Matlab simulation correspond to those from Sim4Life, the only difference is that the amplitude of the Matlab simulation diminishes slightly faster. In Figure 26 the phase maps are shown for the quadrature and the linear settings.
From Figure 26 a clear mismatch can be seen between the Matlab and the Sim4Life phase profiles. The profiles have a similar curve, however the gradient of the Matlab phase profiles is larger. In the following section the effect this has on the reconstruction will be shown.

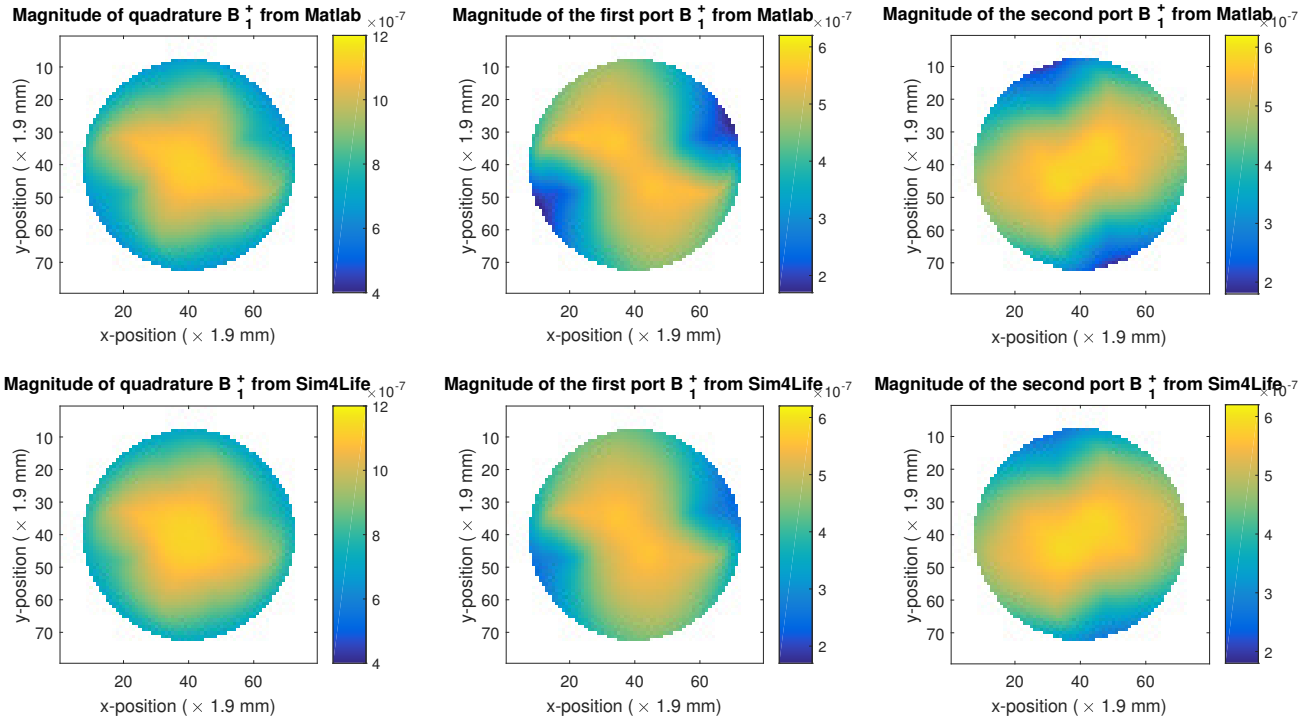

Figure 25: Portrayed are the B_1^+ amplitudes for equal power settings in Matlab and Sim4Life. In the top row from left to right are the quadrature, the left linear and the right linear B_1^+ amplitude maps from Matlab. In the bottom row are the corresponding Sim4Life maps.

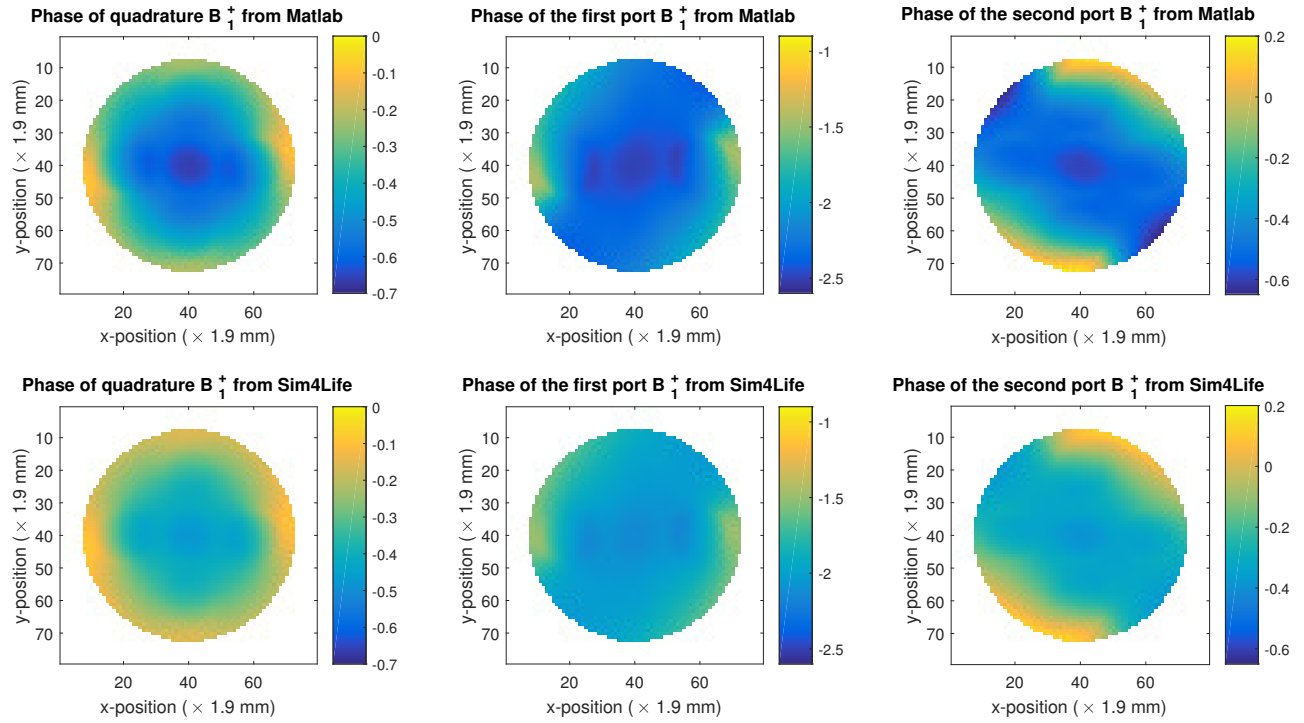

Figure 26: Portrayed are the B_1^+ phases for equal power settings in Matlab and Sim4Life. In the top row from left to right are the quadrature, the left linear and the right linear B_1^+ phase maps from Matlab. In the bottom row are the corresponding Sim4Life maps.

5.3 Reconstructions Sim4Life

This section is started with the reconstruction of the simple phantom with the Sim4Life data. The same values as in Table 2 were simulated. The first permutation of the reconstruction is supplying the algorithm with the perfect B_1^+ data. The next reconstruction is by feeding the algorithm with the TPA data. After this the transceive phase correction algorithm is used with noise and TV regularization. The last reconstruction is the realistic scenario (i.e. transceive phase, noise, truncation of k-space and TV regularisation). In Figure 27 and Figure 28 these reconstructions are shown.

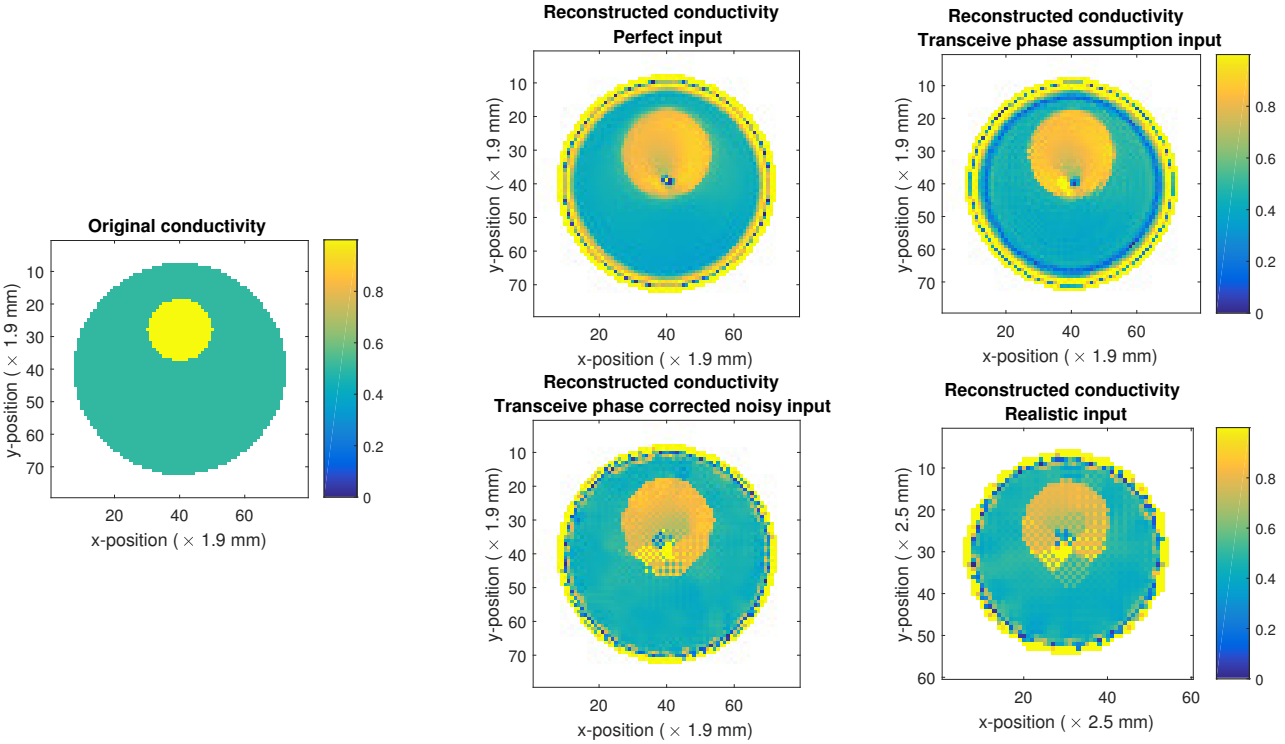

Figure 27: The reconstructed conductivity profiles. On the left is the original profile. In the middle on top is the reconstruction using perfect input. Next to it on the right is the reconstruction with the TPA as input. In the middle on the bottom is the transceive phase corrected with noise on top. On the right of that is the realistic input.

From Figure 28 it can be seen that these reconstructions do not match the original permittivity. The reconstructions from Figure 27 represent the original conductivity better, however the values of the reconstructed conductivity are underestimated. This underestimation is about 15% of the original value. This is most likely the result of the difference in the phase that was seen in Figure 26, which showed the mismatch between the 2D and 3D simulations. To further explore this effect reconstructions were done where not the center slice was taken but slices out of the center of the MRI. This is shown in Figure 29.
From Figure 29 it can seen that taking a slice out of the middle of the centre of the MRI results in a bigger underestimation of the conductivity. This is due to the x and y components of the electric field grow in amplitude, thus the assumption in Equation (2.2.1) is not valid anymore. This can be seen in Figure 30, which can be compared to Figure 24.
To get better reconstructions out of the centre slice a 3D CSI-EPT code needs to be implemented. This has been done in [31]
Furthermore the middle of the phantom is again a problem because the low electric field in the middle creates an instability due to Equation (3.1.23) and because the x and y components of the electric field are in the same order of magnitude as the z component. This results in Equation (2.2.1) to be invalid in this point.

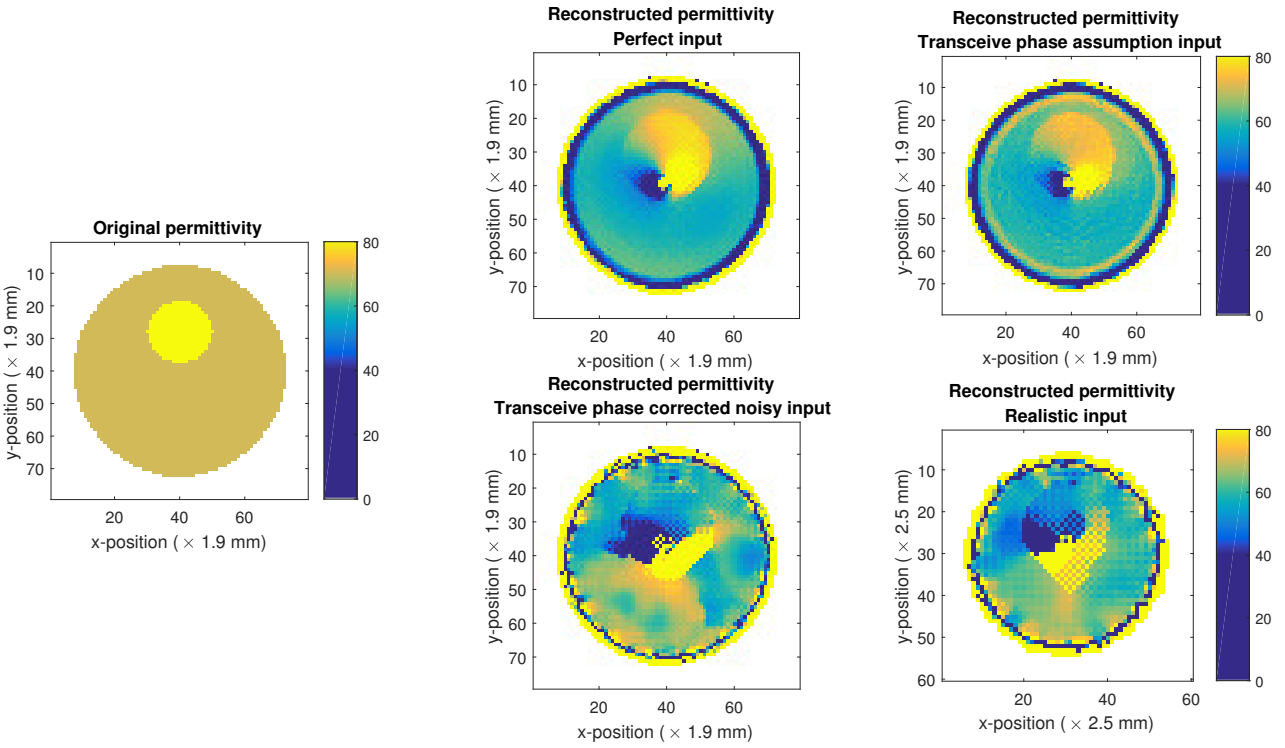

Figure 28: The reconstructed permittivity profiles. On the left is the original profile. In the middle on top is the reconstruction using perfect input. Next to it on the right is the reconstruction with the TPA as input. In the middle on the bottom is the transceive phase corrected with noise on top. On the right of that is the realistic input.

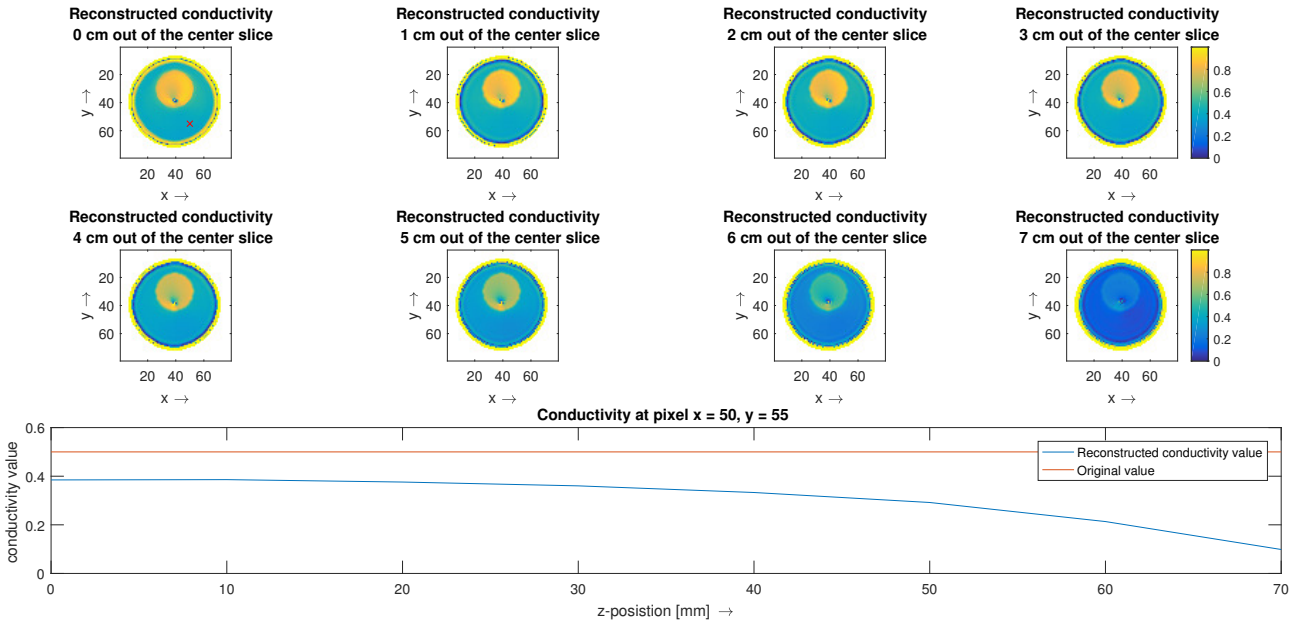

Figure 29: From left to right are the reconstructions of the conductivity out of the center slice, 1cm more per reconstruction. On the bottom is a line plot with in orange the original value of the conductivity at the voxel indicated with the red cross and the blue line is the same voxel plotted for the different reconstructions.

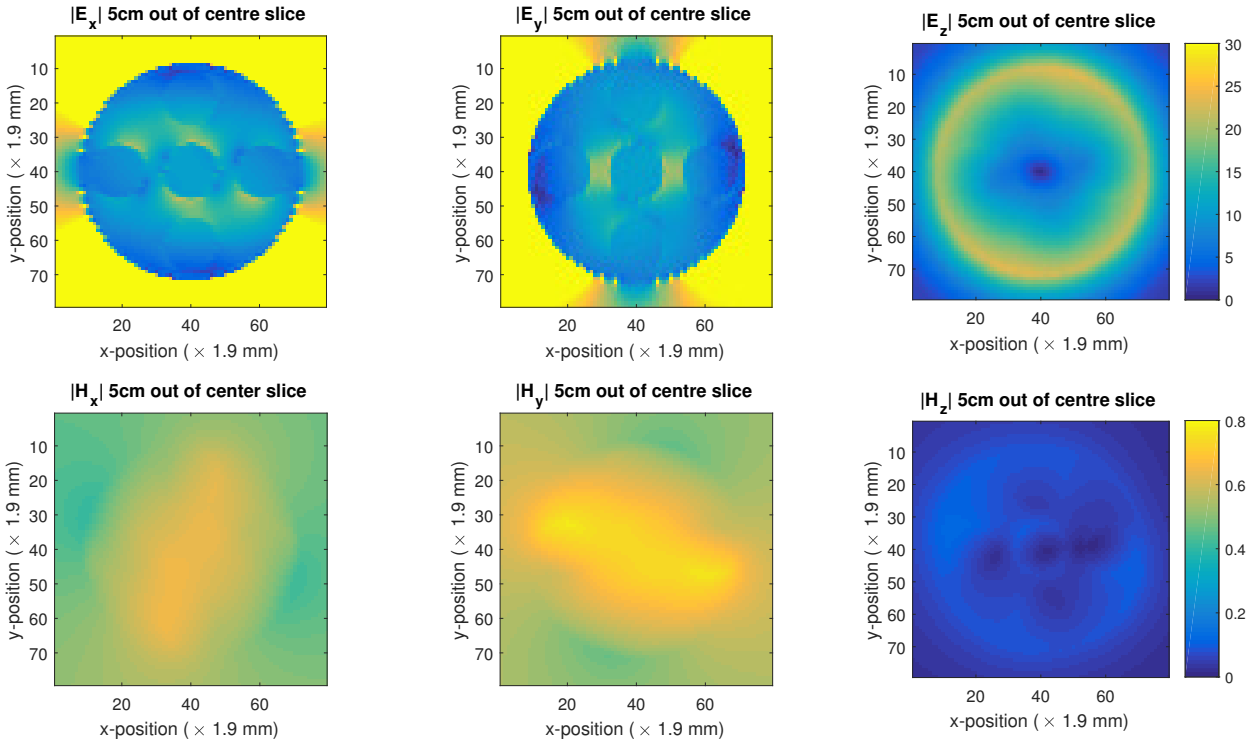

Figure 30: In the top row are the amplitudes of the electric field in the x,y and z-direction all on the same color scale. In the bottom row are the amplitudes of the magnetic field in the x,y and z-direction all on the same color scale. These slices are 5cm out of the centre of the MRI.

5.4 $B_1^{-,RE}$ reconstruction

In Sim4Life the $B_1^{-,RE}$ field is created by simulating the linear excitation and adding the H_x and H_y to get their respective B_1^- fields, as seen in Equation (2.1.6). These are then added with a 90° phase shift to get the correct field. This field is then used to create the transceive phase which is reconstructed with the new CSI algorithm. The result for the simple phantom is shown in Figure 31.

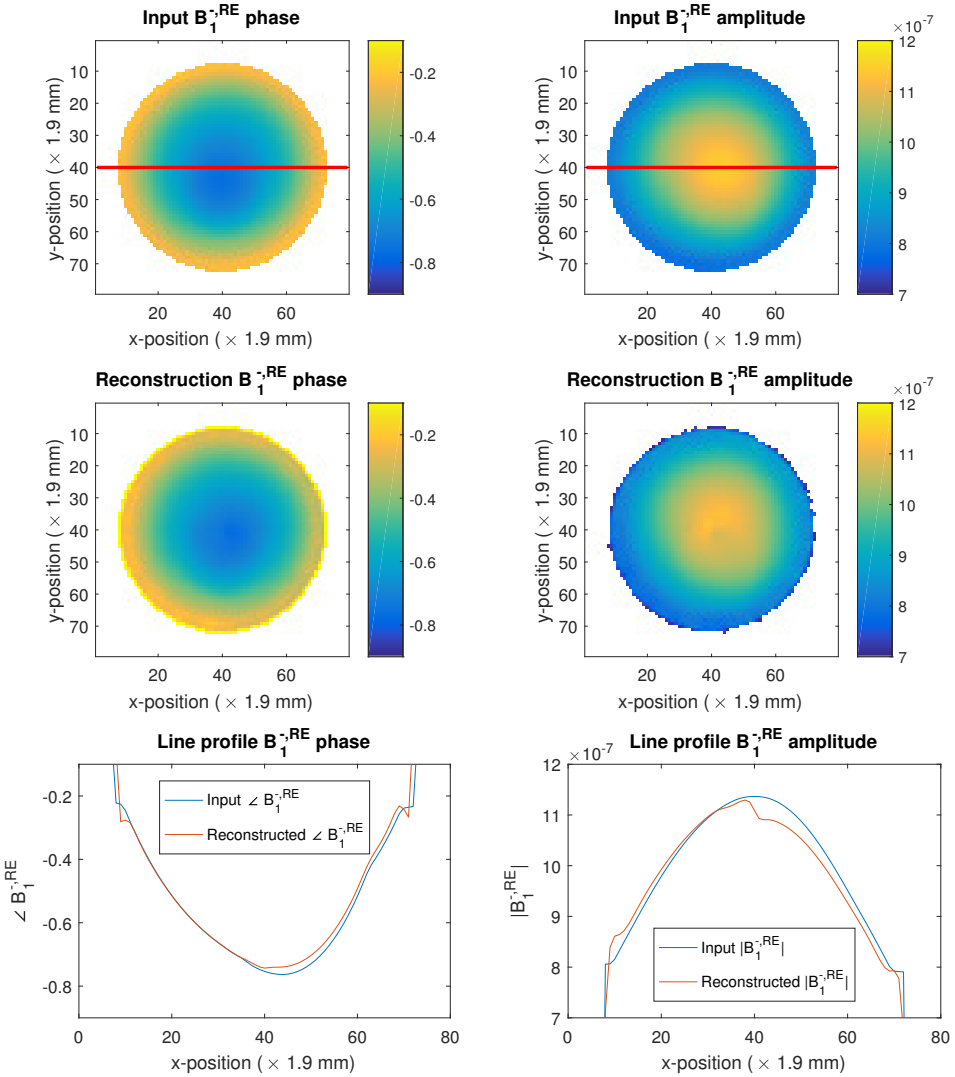

Figure 31: In the top row are the input $B_1^{-,RE}$ phase and amplitude for the simple phantom. In the middle row are the reconstructed $B_1^{-,RE}$ phase and amplitude. The bottom row consists of a line profile of both the phase and amplitude. These line profiles are taken at the location indicated by the red line.

As can be seen in Figure 31 the reconstructed $B_1^{-,RE}$ corresponds very well with the field given as input. The mismatch in the line profiles is due to the minimum in the electric field that is located at exactly the centre of the phantom. For the complicated phantom the result is shown in Figure 32.

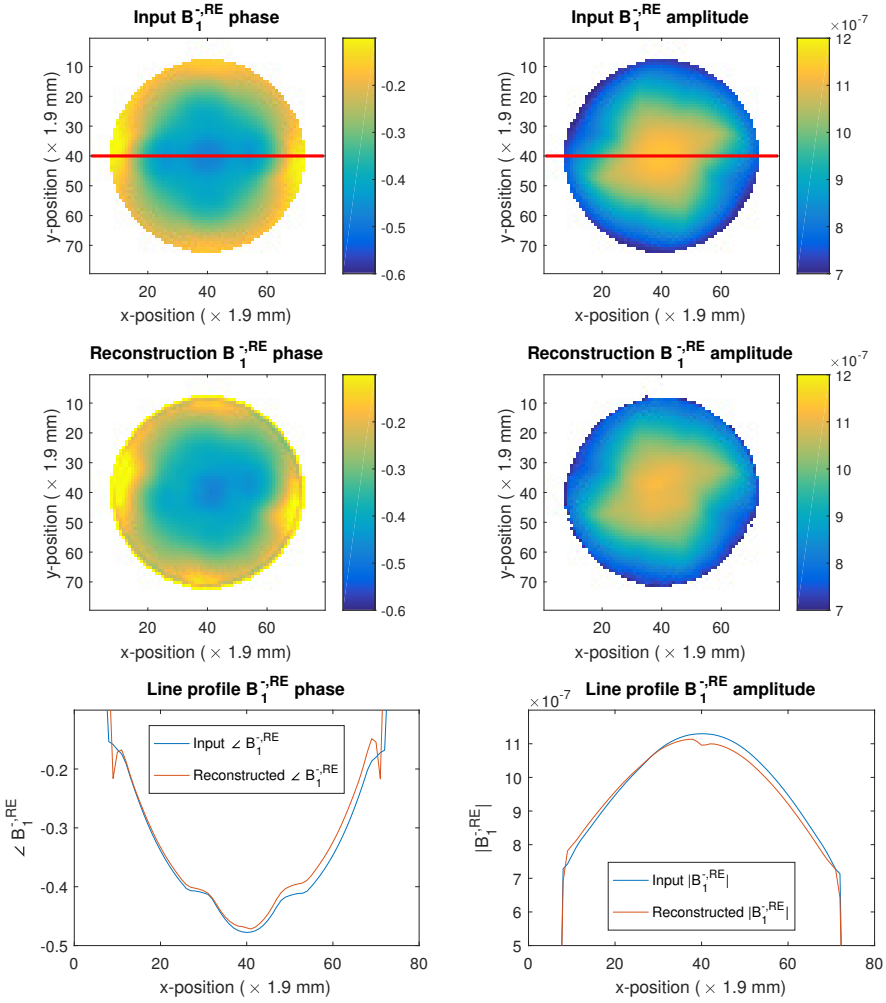

Figure 32: In the top row are the input $B_1^{-,RE}$ phase and amplitude for the complicated phantom. In the middle row are the reconstructed $B_1^{-,RE}$ phase and amplitude. The bottom row consists of a line profile of both the phase and amplitude. These line profiles are taken at the location indicated by the red line.

5.5 Comparison between CSI-EPT and phase only EPT

In this section the current implementation of CSI-EPT will be compared to one of the standard EPT schemes, the phase only EPT method [20]. The magnitude is omitted because it does not improve the reconstruction much and when noise is added it will often make the reconstruction worse. This will give some perspective to the differences between the two methods. For this comparison the Sim4Life data is used and a noiseless case is tested as well as one with SNR 70. For the phase only EPT a kernel of 7 is used to compute the gradients. This kernel is more robust with respect to noise but has a bigger boundary error [9]. The results can be seen in Figure 33, for the phase only reconstruction the absolute values were plotted.

From Figure 33 it can be seen that CSI-EPT has less boundary issues compared to the phase only reconstruction. However the conductivity values of the phase only reconstruction show a better result than the CSI-EPT. This is again because CSI-EPT is underestimating the conductivity value. For a quantitative analysis the mean and variance are calculated for the three different conductivity values. Voxels near a boundary were not taken into account because it is already clear from the images in Figure 33 that CSI-EPT reconstructs these correctly whereas the phase only EPT method does not. The masks that were used are shown in Figure 34.

The values of the mean and variance or shown in table Table 9. In Figure 35 the normal distributions are plotted to visualize these results better.

From Figure 35 it can be concluded that CSI-EPT is more precise than the phase only EPT, except for the noiseless case for 0.1 S/m. This is because CSI-EPT has difficulty with reconstruction very small conductivities precisely. Further it is seen that in all the conductivity values that were reconstructed with noise that CSI-EPT

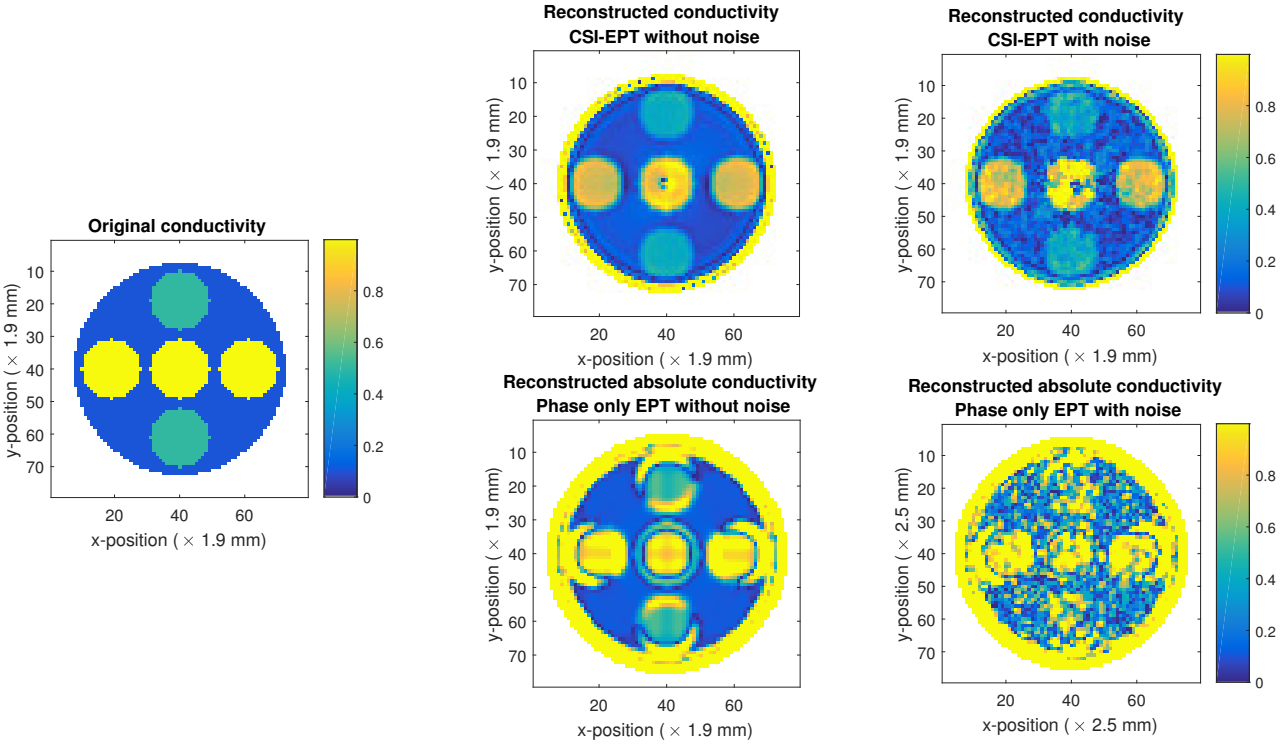

Figure 33: On the left is the original conductivity. In the top row are the CSI-EPT reconstructions, first the noiseless case and then the noisy case. In the bottom row are the phase only EPT reconstructions, first the noiseless case and then the noisy case. For the phase only reconstruction the absolute values were plotted.

Table 9: The mean and variance for the four different reconstructions. Without the boundaries regions.

Reconstruction method	Mean at 1 S/m	Variance at 1 S/m	Mean at 0.5 S/m	Variance at 0.5 S/m	Mean at 0.1 S/m	Variance at 0.1 S/m
CSI-EPT without noise	0.7932	0.0882	0.4124	0.00034	0.0752	0.0148
CSI-EPT with noise	0.7979	0.0589	0.4020	0.0051	0.0560	0.0292
Phase only EPT without noise	0.8705	0.1304	0.4353	0.0534	0.0848	0.0066
Phase only EPT with noise	0.8649	0.2405	0.4910	0.2402	0.0679	0.1586

is significantly more precise than phase only EPT. On the other hand the mean value of phase only EPT is slightly better a reason for this is that the noise in the simulation is white Gaussian noise, as has been explained in Section 2.6. The mean of this noise is zero and thus has no influence on the mean value of the reconstructed conductivity. Finally for the left plot of Figure 35 the noisy CSI-EPT reconstruction is more precise than its noiseless counterpart. This can be explained by the fact that the centre voxels are not reconstructed into a smooth profile, but when TV regularization is applied on noisy data the middle is smoothed out and thus the variance decreases.
The results shown were without the boundaries taken into account because here the phase only EPT does not work well. However, when reconstructing an object the location of the boundaries are not known. Therefore it is not known where the phase only EPT is accurate, thus the mean values and the variance when the boundary regions are taken into account are shown in Table 10. The results are plotted as normal distributions in Figure 36.

Table 10: The mean and variance for the four different reconstructions. With the boundaries regions included.

Reconstruction method	Mean at 1 S/m	Variance at 1 S/m	Mean at 0.5 S/m	Variance at 0.5 S/m	Mean at 0.1 S/m	Variance at 0.1 S/m
CSI-EPT without noise	0.7353	0.0756	0.3702	0.0085	0.2405	0.2460
CSI-EPT with noise	0.7512	0.0641	0.3710	0.0111	0.0142	0.0466
Phase only EPT without noise	0.4755	1.0636	0.2514	0.4074	-0.0250	0.1134
Phase only EPT with noise	0.4534	1.1721	0.2839	0.5388	-0.0297	0.2634

From Table 10 and Figure 36 it can be seen that the CSI-EPT reconstruction is more accurate and more precise when the boundaries are included.

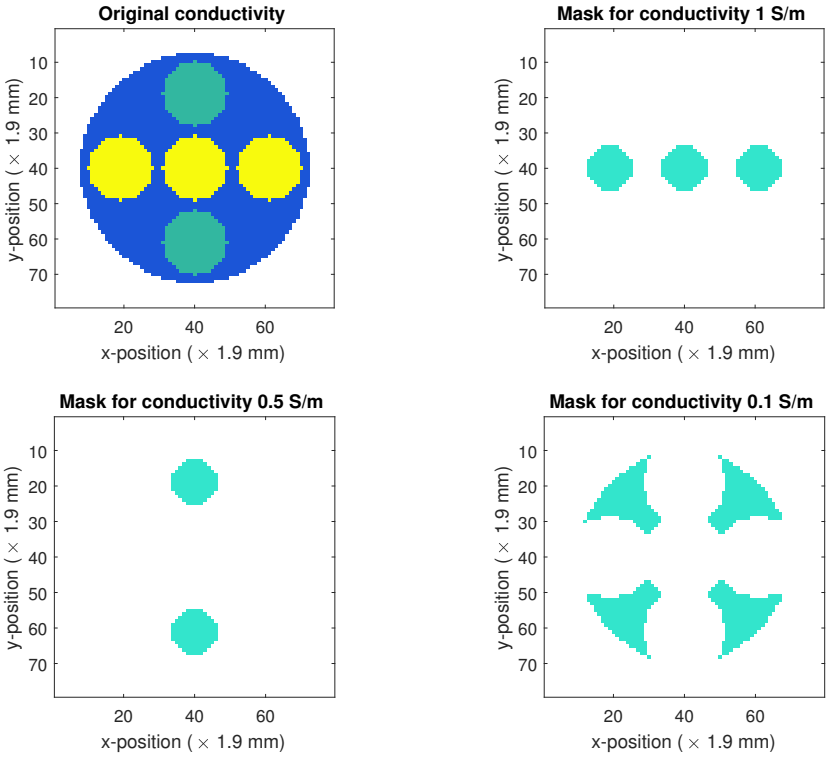

Figure 34: The top left figure is the original conductivity map. The rop right shows the mask that was used for the conductivity compartments with a value of 1 S/m. The bottom left shows the mask for 0.5 S/m and the bottom right the mask for 0.1 S/m. These masks exclude the biggest part of the boundary in the phase only EPT approach.

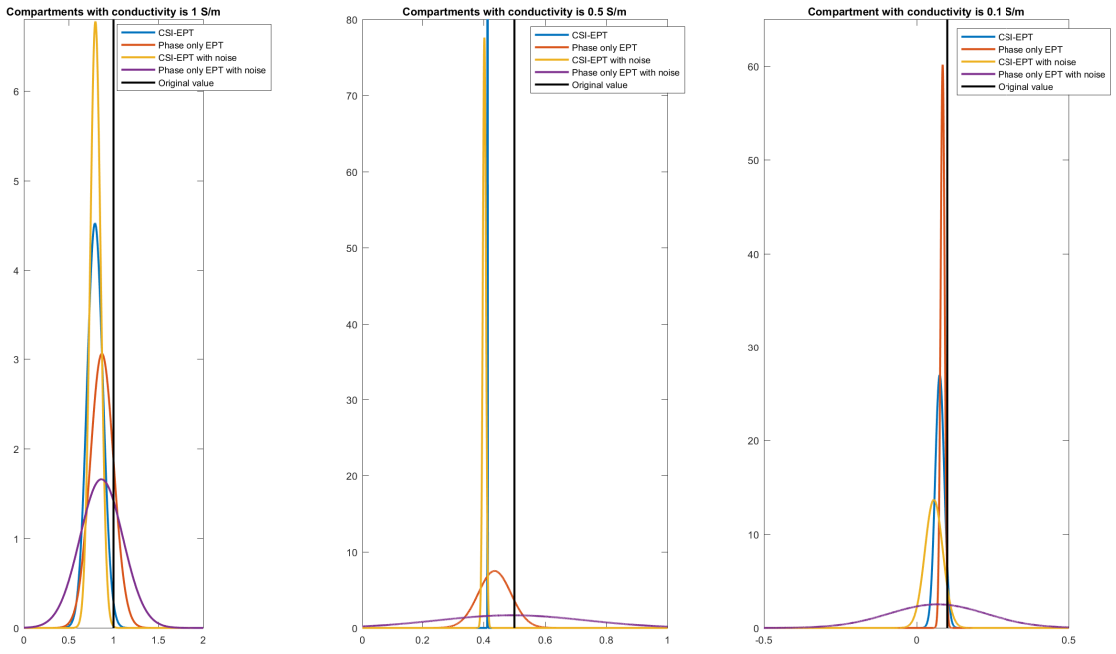

Figure 35: The normal distributions from Table 9.The left plot shows the distribution for the compartments with conductivity value of 1 S/m. The middle plot for the compartments with conductivity value 0.5 S/m. In the right plot the distributions for 0.1 S/m are shown.

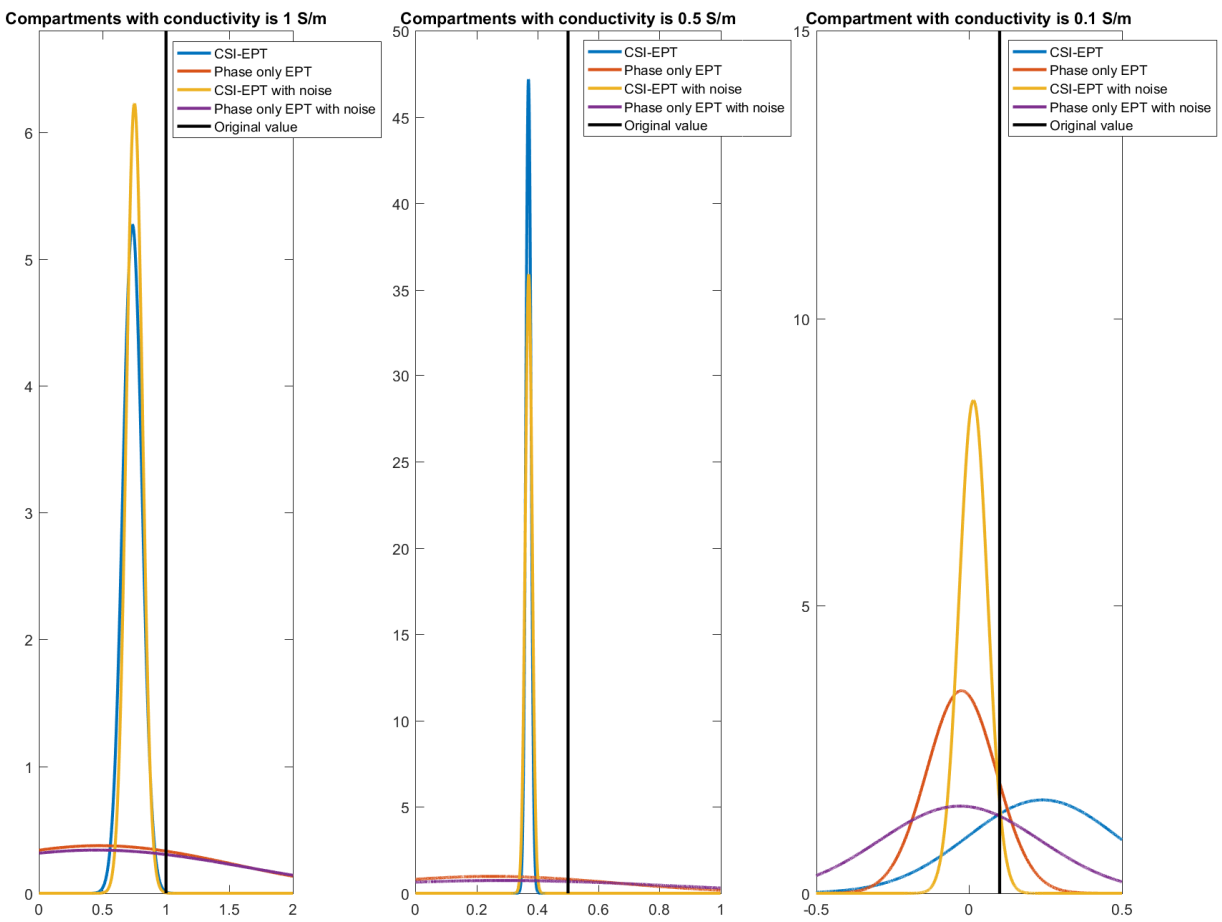

Figure 36: The normal distributions from Table 10.The left plot shows the distribution for the compartments with conductivity value of 1 S/m. The middle plot for the compartments with conductivity value 0.5 S/m. In the right plot the distributions for 0.1 S/m are shown.

6 MRI Measurements

The goal for this thesis is to show an experimental result of CSI-EPT and that is what this section will cover. First the setup of the experiment is discussed. After this the measurements are compared to the simulated fields. And finally the results of the reconstruction are shown.

6.1 Materials and methods

The scanner that was used is a Philips ingenia 3T which is located in UMC Utrecht. To measure the RF phase two single Spin Echo sequences were used, this sequence is described in [32]. Two measurements are used to compensate for the artifacts that arise due to the eddy currents. The parameters of the sequence are shown in Table 11.

Table 11: The Spin Echo sequence parameters.

Parameter	Value
FoV	200 by 200 by 2.5 mm^3
Resolution	2.5 by 2.5 by 2.5 mm^3
Repetition time (TR)	1000 ms
Echo time (TE) quadrature mode acquisition	5 ms
Echo time linear mode acquisition	9 ms
Water-fat shift/Bandwidth	$\frac{0.3}{1400}$ pixels Hz^{-1}

For the B_1^+ magnitude a dual TR AFI(3D - FFE) sequence was used [13]. The parameters for this scan are shown in Table 12.

Table 12: The AFI sequence parameters.

Parameter	Value
FoV	200 by 200 by 9 mm^3
Resolution	2.5 by 2.5 by 3 mm^3
TR1	50 ms
TR2	250 ms
TE	2.7 ms
Water-fat shift/Bandwidth	$\frac{0.9}{480}$ pixels Hz^{-1}
Flip angle	65°

Both sequences were done with both NSA 10 and NSA 2 with the same parameters. Further the FoV was set to (0,0,0).
An 1.5% agar based phantom was made for testing, this phantom can be seen in Figure 37.
The conductivity values and the size of the phantom are given in Table 13.

Table 13: The conductivity values and the size of the constructed phantom.

	Conductivity [S/m]	Diameter [cm]
Inner compartment	0.45	4
Outer compartment	0.95	11.5

For the measurements the phantom was placed in the centre of the MRI in order to satisfy the 2D assumption in Equation (2.2.1) the best. Further a body coil was used for transmitting and a head coil was used for receiving the signal. The CLEAR setting on the scanner was on. By setting this option on the measured signal in the head coil is post processed to output the results that would be acquired when using the body coil for both transmitting and receiving.

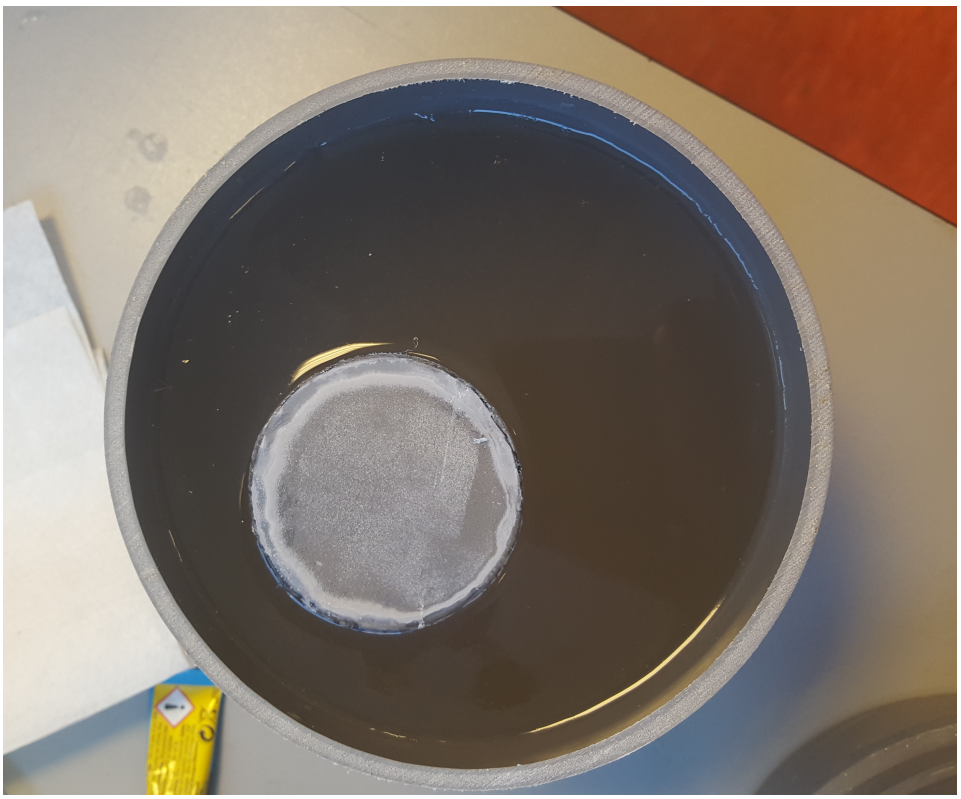

Figure 37: The constructed phantom with one compartment inside. It should resemble the conductivity profile of the simple phantom used in simulations.

6.2 Comparison measured data with Sim4Life simulation

An interesting comparison to make is how the B_1^+ amplitudes and transceive phase maps from Sim4Life and the MRI scanner differ from each other. The maps from Sim4Life do not contain noise whereas the measured data does. The measured data is from a scanning session with NSA 2. The result of the amplitude and phase maps are shown in Figure 38 and Figure 39. respectively.
From Figure 38 it can be seen that the quadrature and the second linear excitation do not match the simulation very well, especially the second linear excitation. This can be due to the fact that the permittivity of the constructed phantom is not know and therefore does not match the one simulated in Sim4Life. From Figure 39 it can be concluded that the phase patterns do look very similar. In the following section the reconstructions are shown.

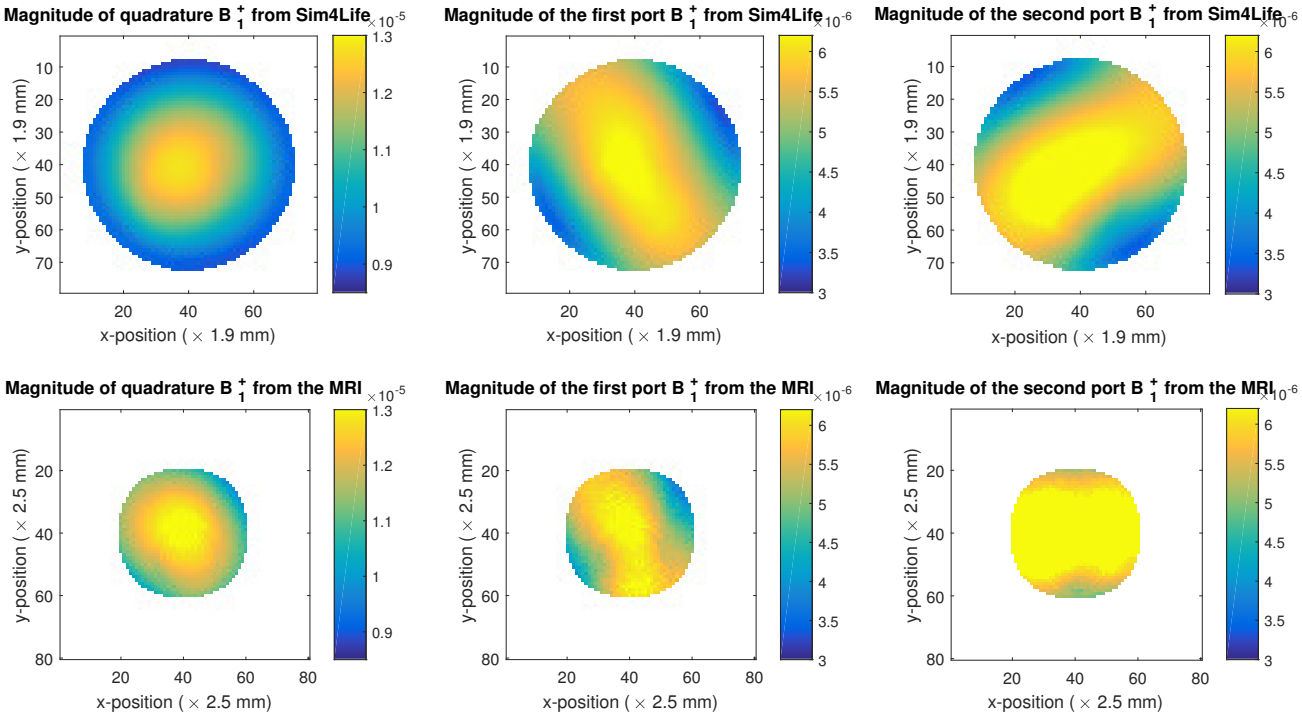

Figure 38: The top row are the B_1^+ maps for the simple phantom from Sim4Life. From left to right are the quadrature excitation and then the two linear excitations. On the bottom are the B_1^+ maps from the scanner.

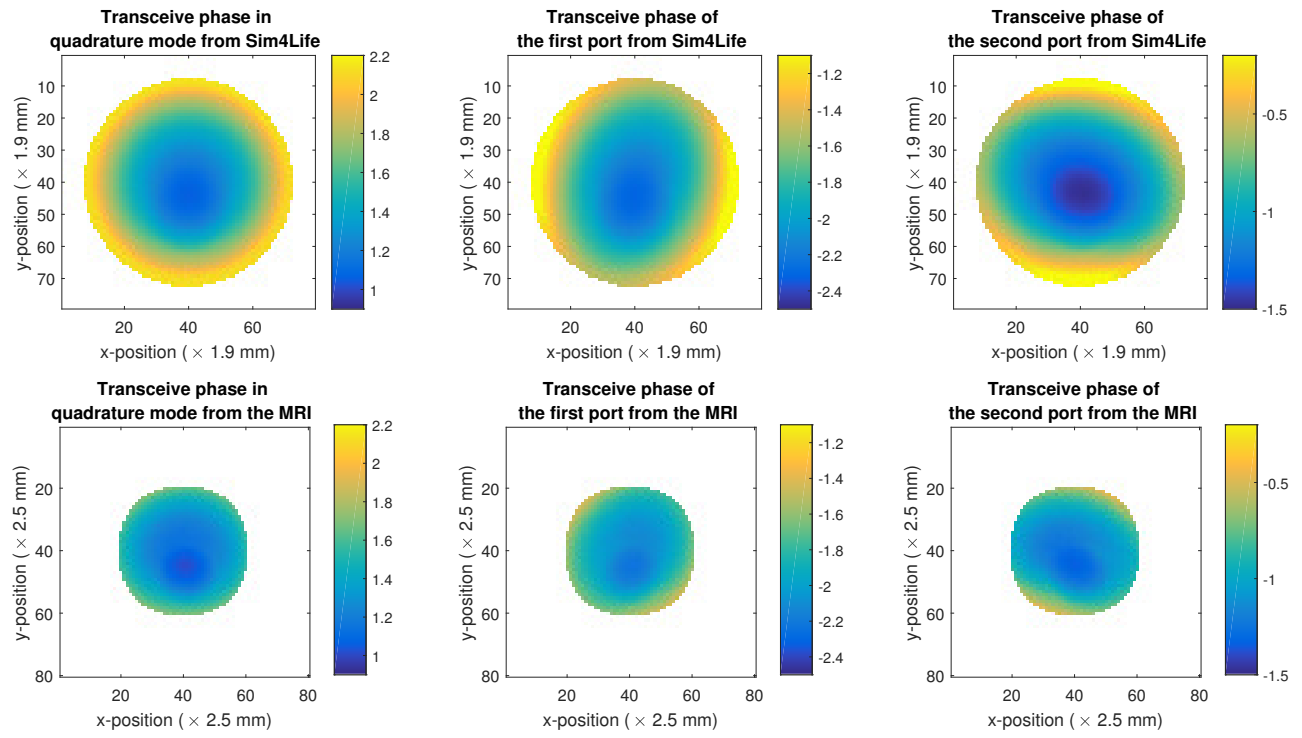

Figure 39: The top row are the transceive phase maps for the simple phantom from Sim4Life. From left to right are the quadrature excitation and then the two linear excitations. On the bottom are the transceive phase maps from the scanner.

6.3 Reconstructions measured data

For the reconstruction both the NSA 10 measurements and the NSA 2 measurements were used, to see the difference the SNR of the measurement has on the reconstruction. Further for the reconstruction only the quadrature excitation maps were taken because the linear excitation maps did not help the reconstruction at all. This can be due to the fact that in Figure 38 the linear excitation do not match very well. Or it can be because some of the parameters of the scanner are not known exactly. For example the RF-shield and coil radius, it is known that they are larger than 35 cm and smaller than 40 cm and there are more of these parameters that should be known in order to get the best possible reconstruction. These parameters are necessary for the construction of the incident fields. What has been done to verify that the parameters were correct was by taking the first order induced current method from [7] and sweep each parameter until an optimal reconstruction was acquired. This method uses the incident fields as well but is much faster in reconstructing the contrast compared to CSI-EPT (i.e. a few milliseconds compared to 1 minute).
The reconstructed conductivity can be seen in Figure 40. For the phase only EPT kernel 7 was used for the reconstruction.

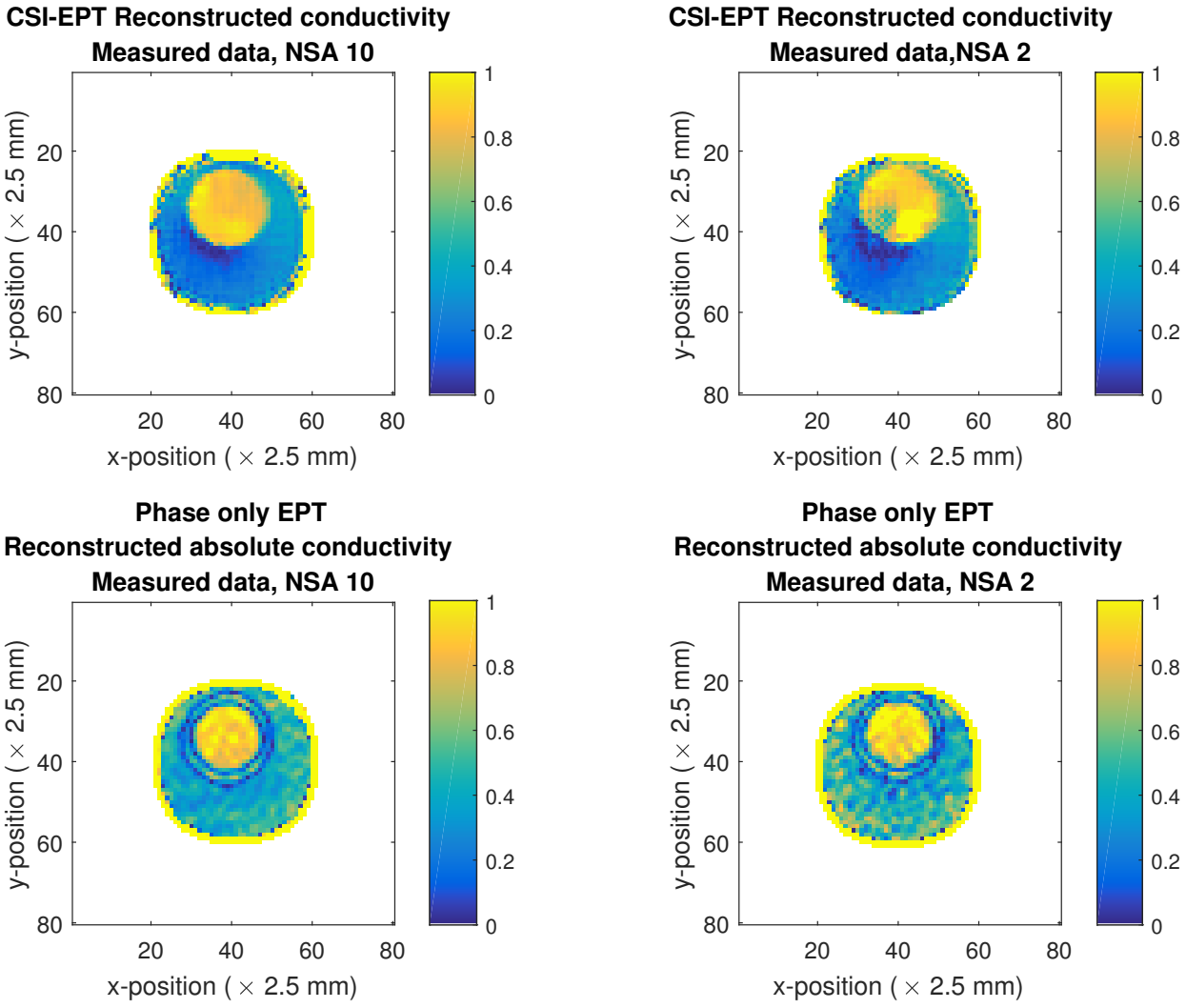

Figure 40: The top left image is the reconstruction of the conductivity with NSA 10 and the top right is the reconstruction with NSA 2. The bottom left is the phase only EPT reconstruction with NSA 10 and the bottom right is the phase only EPT reconstruction with NSA2.

From Figure 40 it can be seen that the CSI-EPT reconstruction resembles the constructed phantom very well. There are no boundary issues in the CSI-EPT reconstruction compared to the phase only EPT reconstruction. However, there is still an underestimation present in the CSI-EPT reconstruction. Further the outer compartment shows as slope in the conductivity this is most likely because only the quadrature map has been used

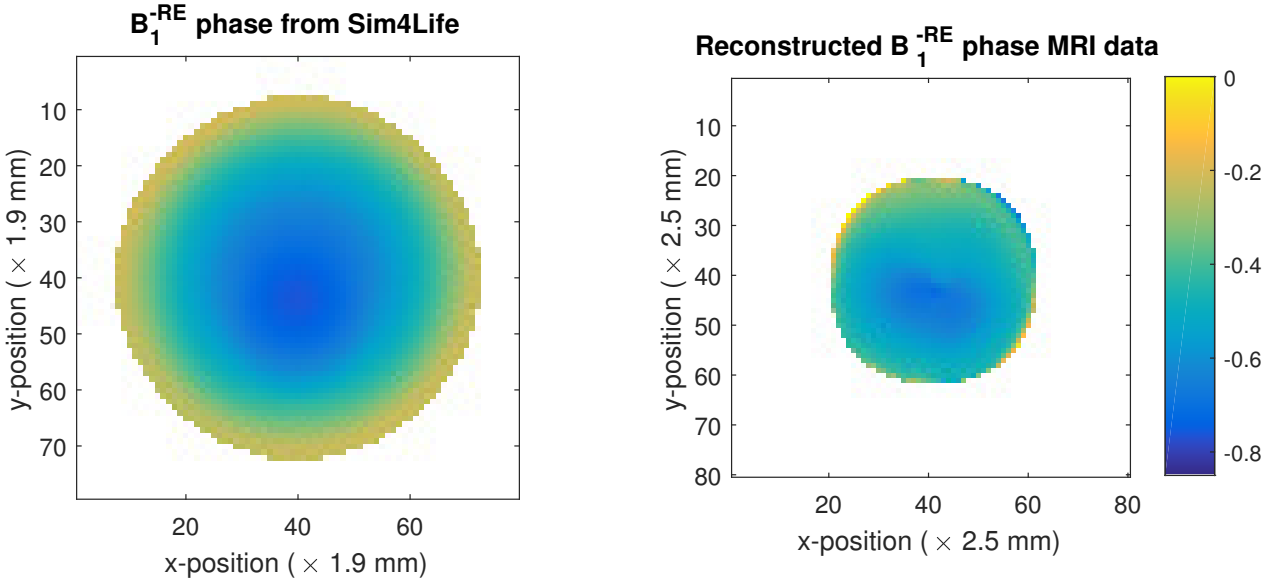

Figure 41: On the left is the receive phase from Sim4Life, on the right is the reconstructed receive phase.

for reconstruction. Normally the extra data from the linear excitations helps the reconstruction to get a more uniform profile, this is what is used in the simulations. In [12] the effect of only using the quadrature map is shown. Finally the effect of a lower SNR can be seen near the centre of the phantom at the boundary between the two compartments. This is the point where the electric field is at a minimum and the algorithm sometimes has difficulty reconstructing this.
Again the receive phase is reconstructed this can be seen in Figure 41.
From this reconstruction it can be seen that the phase profile is very similar compared to the simulated phase from Sim4Life. There is however no way to check if this is actually correct other than comparing it to simulations since this has never been done before. But the profiles are comparable and that should give some confidence that this is indeed the receive phase from the scanner.

7 Conclusion

The main goal of this thesis was to investigate if CSI-EPT can be used on measured MRI data. The 2D Matlab simulations showed that the algorithm works well for 2D data and can handle a variety of realistic situations. One of the limitations is that the incident fields need to be known, this posed a problem with the processing of the measurements. However the numerically implemented RF-shield made the incident fields that are computed more realistic. A first order approximation was enough to match the constructed incident fields with those present in the MRI scanner, since the value for the current in the log file of the scanner resulted in a good reconstruction.
In the Sim4Life reconstructions it was concluded that the step from 2D to 3D introduced an underestimation of the conductivity profiles. This is due to the difference in the phase profiles between the 2D simulation and the 3D simulation. As of now the underestimation seems to be about 15%. However, it is not known if for different objects this underestimation is different. As for the permittivity profile, it is still very difficult to reconstruct this at a static magnetic field strength of 3T. For higher field strengths this reconstruction should improve significantly because of the higher curvature of the magnetic field. The receive phase reconstruction that was implemented showed good results in both the 2D and 3D simulations. Only in 3D the minimum of the electric field had a larger effect on both the reconstruction of the receive phase and the reconstruction of the contrast.
Finally the reconstructions done with the measured data showed that the conductivity profile matched the constructed phantom values, however again with the same underestimation as with the Sim4Life reconstructions. This indicates that the simulations are close to the reality except for the linear excitations, where the phase maps did match but the simulated and measured amplitude maps did not. This is most likely due to the fact that scanner wants to optimize the homogeneity of the B_1^+ and thus introduces a phase shift between the two ports. Nonetheless the measured data could be reconstructed, thus giving an answer to the research question that CSI-EPT can indeed be practically implemented.
When compared to the phase only EPT reconstructions, CSI-EPT showed much better precision plus the boundary regions between compartments are reconstructed properly. This was both seen for the 3D simulations and the measured data.
Further by rewriting the algorithm to include the transceive phase additional outputs of the algorithm can be computed. These are all the RF-fields present in the scanner, both during the transmitting and receiving state of the MRI. On top of that it enables CSI-EPT to have potential at reconstructing the electrical properties at higher static magnetic field strengths. The benefits from these higher field strength is that the SNR increases and since noise is not a problem for CSI-EPT a higher resolution image can be made of the object in the scanner. Plus the higher curvature of the magnetic field helps the reconstruction of the permittivity. Which at 3T still is not feasible.

8 Future Research

In this section a few new ideas are opted that can be researched. There are two problems at hand that should be tackled to get a better reconstruction. The first is the electric field that has a minimum in the centre of the coil. This can be done by for example adding dielectric pads to the scanned object, this can shift the minimum of the electric field out of the object and thus circumvent the problem. What changes in the code is the incident fields need to be calculated with the dielectric pad in the scanner. This however is a forward problem and can be computed easily. Another way this problem can be solved is by changing the measurement setup, by instead of using a body coil a dipole antenna array is used. These dipoles create a different incident electric field that has no minimum in the centre. The difficulty with this however is finding a well designed dipole antenna array, plus the coupling of the dipoles needs to be kept in mind when computing the incident fields.
The second problem with the algorithm right now is the 2D assumption. In [31] a 3D implementation of the CSI-EPT algorithm is presented. A logical next step is to combine the transceive phase correction presented in this work with the 3D algorithm. Further the free space Green's function can be changed to include the RF-shield, which is now implemented numerically. This has been shown in [16], however the free space Green's function does not show any problems as of yet and implementing this new Green's function will slow down the algorithm tremendously. The combination of a 3D algorithm, the Green's function with the RF-shield included and the presented transceive phase correction method should result in an algorithm without assumptions.
Something that has been tried during this project is changing the update direction, nonlinear conjugate gradient method, to a quasi newton method (i.e. Broyden–Fletcher–Goldfarb–Shanno, or its memory limited variant). This should give superlinear convergence, thus less iterations are needed. A downside is that each iteration will take longer, especially when not using the memory limited variant. This is because the inverse Hessian matrix needs to be updated which is n by n matrix, where n is that number of variables to be solved. The problem I encountered with using this method was that exact stepsize given in Equation (3.1.20) together with the new update direction does not fulfill the secant equations that are imposed for superlinear convergence. Thus to make this work an inexact line search must be done which seems very counter intuitive and was thus not pursued.
Further from Figure 18 it is apparent that a higher field strength results in better reconstructions. This is due higher curvature of the measured fields. Plus the signal strength is higher than at 3T thus the SNR goes up for these scans. However, the SNR is not a problem for CSI-EPT thus the resolution can be increased. By taking smaller voxels the SNR goes down again but the resolution goes up.
Finally the most interesting advancement this transceive phase correction algorithm enables is the improvement of antenna designs for MRI. Using this algorithm on measured data will output the B_1^- fields in both transmit and receive. This information was always corrupted by the transceive phase. With the current antenna design done on 7T systems this algorithm can help with giving more insight on the efficiency of those designs.

References

[1] C. Westbrook, C. Roth, and J. Talbot, *MRI in Practice*. Wiley, 2011.

[2] E. Haacke, R. Brown, M. Thompson, and R. Venkatesan, *Magnetic Resonance Imaging: Physical Principles and Sequence Design*. Wiley, 1999.

[3] A. G. Webb, Ed., *Magnetic Resonance Technology*, ser. New Developments in NMR. The Royal Society of Chemistry, 2016.

[4] E. M. Haacke, L. Petropoulost, E. Nilges, and D. Wu, "Extraction of conductivity and permittivity using magnetic resonance imaging," *Physics in Medicine and Biology*, vol. 36, no. 6, pp. 723–734, 1991.

[5] E. Balidemaj, H. P. Kok, G. Schooneveldt, A. L. van Lier, R. F. Remis, L. J. Stalpers, H. Westerveld, A. J. Nederveen, C. A. van den Berg, and J. Crezee, "Hyperthermia treatment planning for cervical cancer patients based on electrical conductivity tissue properties acquired in vivo with ept at 3 t mri," *International Journal of Hyperthermia*, vol. 32, no. 5, pp. 558–568, 2016.

[6] J. Liu, X. Zhang, S. Schmitter, P.-F. V. de Moortele, and B. He, "Gradient-based Electrical Properties Tomography (gEPT): a Robust Method for Mapping Electrical Properties of Biological Tissues In Vivo Using Magnetic Resonance Imaging," *Magnetic Resonance Med.*, vol. 28, no. 10, pp. 1304–1314, 2016.

[7] P. Fuchs, "Mri based electrical properties tomography: Electromagnetic inversion," 2016.

[8] X. Zhang, J. Liu, and B. He, "Magnetic-resonance-based electrical properties tomography: a review," *IEEE reviews in biomedical engineering*, vol. 7, pp. 87–96, 2014.

[9] S. Mandija, A. Sbrizzi, P. Luijten, and C. van den Berg, "Error analysis of helmholtz based mr electric property tomography," *To be submitted*, 2017.

[10] P. van den Berg and R. Kleinman, "A contrast source inversion method," *Inverse Problems*, vol. 13, no. 6, p. 1607, 1999.

[11] A. Abubaker and P. Van Den Berg, "Total variation as a multiplicative constraint for solving inverse problems," *IEEE Transactions on Image Processing*, vol. 10, no. 9, pp. 1384–1392, 2001.

[12] E. Balidemaj, C. A. T. Van Den Berg, J. Trinks, A. L. H. M. W. Van Lier, A. J. Nederveen, L. J. A. Stalpers, H. Crezee, and R. F. Remis, "CSI-EPT: A Contrast Source Inversion Approach for Improved MRI-Based Electric Properties Tomography," *IEEE Transactions on Medical Imaging*, vol. 34, no. 9, pp. 1788–1796, 2015.

[13] V. L. Yarnykh, "Actual flip-angle imaging in the pulsed steady state: A method for rapid three-dimensional mapping of the transmitted radiofrequency field," *Magnetic Resonance in Medicine*, vol. 57, no. 1, pp. 192–200, 2007.

[14] L. Sacolick, F. Wiesinger, I. Hancu, and M. W. Vogel, "B1 Mapping by Bloch-Siegert Shift," *Magnetic Resonance Med.*, vol. 21, no. 2, pp. 146–154, 2011.

[15] K. Nehrke and P. Börnert, "DREAM-a novel approach for robust, ultrafast, multislice B1 mapping," *Magnetic Resonance in Medicine*, vol. 68, no. 5, pp. 1517–1526, 2012.

[16] A. Arduino, L. Zilberti, M. Chiampi, and O. Bottauscio, "CSI-EPT in presence of rf-shield for mr-coils," *Transactions on Medical Imaging.*, 2017.

[17] R.F.Remis, "Lecture notes Wavefield Imaging," 2016.

[18] M. Abramowitz and I. Stegun, *Handbook of mathematical Functions With Formulas, Graphs, and Mathematical Tables*, ser. Applied Mathematics Series. National Bureau of Standards, 1964.

[19] J. Jin, *Electromagnetic Analysis and Design in Magnetic Resonance Imaging*, ser. Biomedical Engineering. Taylor & Francis, 1998.

[20] A. L. Van Lier, D. O. Brunner, K. P. Pruessmann, D. W. J. Klomp, P. R. Luijten, J. J. W. Lagendijk, and C. A. T. Van Den Berg, "B 1+ phase mapping at 7 T and its application for in vivo electrical conductivity mapping," *Magnetic Resonance in Medicine*, vol. 67, no. 2, pp. 552–561, 2012.

[21] P. F. Van De Moortele, C. Akgun, G. Adriany, S. Moeller, J. Ritter, C. M. Collins, M. B. Smith, J. T. Vaughan, and K. agurbil, "B1 destructive interferences and spatial phase patterns at 7 T with a head transceiver array coil," *Magnetic Resonance in Medicine*, vol. 54, no. 6, pp. 1503–1518, 2005.

[22] T. Voigt, U. Katscher, and O. Doessel, "Quantitative conductivity and permittivity imaging of the human brain using electric properties tomography," *Magnetic Resonance in Medicine*, vol. 66, no. 2, pp. 456–466, 2011.

[23] R. Remis and E.Charbon, "An Electric Field Volume Integral Equation Approach to Simulate Surface Plasmon Polaritons," *Advanced Electromagnetics*, vol. I, pp. 16–19, 2012.

[24] J. Nocedal and S. J. Wright, *Numerical optimization*. Springer, 1999.

[25] L. I. Rudin, S. Osher, and E. Fatemi, "Nonlinear total variation based noise removal algorithms," *Physica D*, vol. 60, pp. 259–268, 1992.

[26] P. M. van den Berg, A. Abubakar, and J. T. Fokkema, "Multiplicative regularization for contrast profile inversion," *Radion Science*, vol. 38, no. 2, 2003.

[27] A. Christ, W. Kainz, E. G. Hahn, K. Honegger, M. Zefferer, E. Neufeld, W. Rascher, R. Janka, W. Bautz, J. Chen, B. Kiefer, P. Schmitt, H.-P. Hollenbach, J. Shen, M. Oberle, D. Szczerba, A. Kam, J. W. Guag, and N. Kuster, "The virtual family—development of surface-based anatomical models of two adults and two children for dosimetric simulations," *Physics in Medicine & Biology*, vol. 55, no. 2, p. N23, 2010.

[28] P. R. Haffinger, "Seismic Broadband Full Waveform Inversion by shot / receiver refocusing door," pp. 4–7, 2013.

[29] S. K. Lee, S. Bulumulla, and I. Hancu, "Theoretical Investigation of Random Noise-Limited Signal-to-Noise Ratio in MR-Based Electrical Properties Tomography," *IEEE Transactions on Medical Imaging*, vol. 34, no. 11, pp. 2220–2232, 2015.

[30] V. Vaidya, C. Collins, D. Sodickons, R. Brown, G. Wiggins, and R. Lattanzi, "Dependence of b_1^+ and b_1^- field patterns of surface coils on the electrical properties of the sample and the MR operating frequency," *Concepts in Magnetic Resonance Part B*, vol. 46B, pp. 25–40, 2016.

[31] R. Leijsen, "Three-dimensional contrast source inversion-electrical properties tomography: 3D csi-ept," 2016.

[32] A. L. Van Lier, A. Raaijmakers, T. Voigt, J. J. W. Lagendijk, P. R. Luijten, U. Katscher, and C. A. T. Van Den Berg, "Electrical properties tomography in the human brain at 1.5, 3, and 7T: A comparison study," *Magnetic Resonance in Medicine*, vol. 71, no. 1, pp. 354–363, 2014.

Appendix A Extra figures

In this section are the reconstructions that were done on the second phantom and on Ella's brain slice. These were done to see the effect more (complicated) structures has on the reconstruction. First are the same reconstructions as Figure 11 and Figure 12. After this the TPA is compared to the transceive phase correction. These are followed by the same reconstructions from Figure 19 and Figure 20. Then the line profiles of the second phantom and Ella are given. Finally the $B_1^{-,RE}$ reconstruction for a realistic scenario is shown.

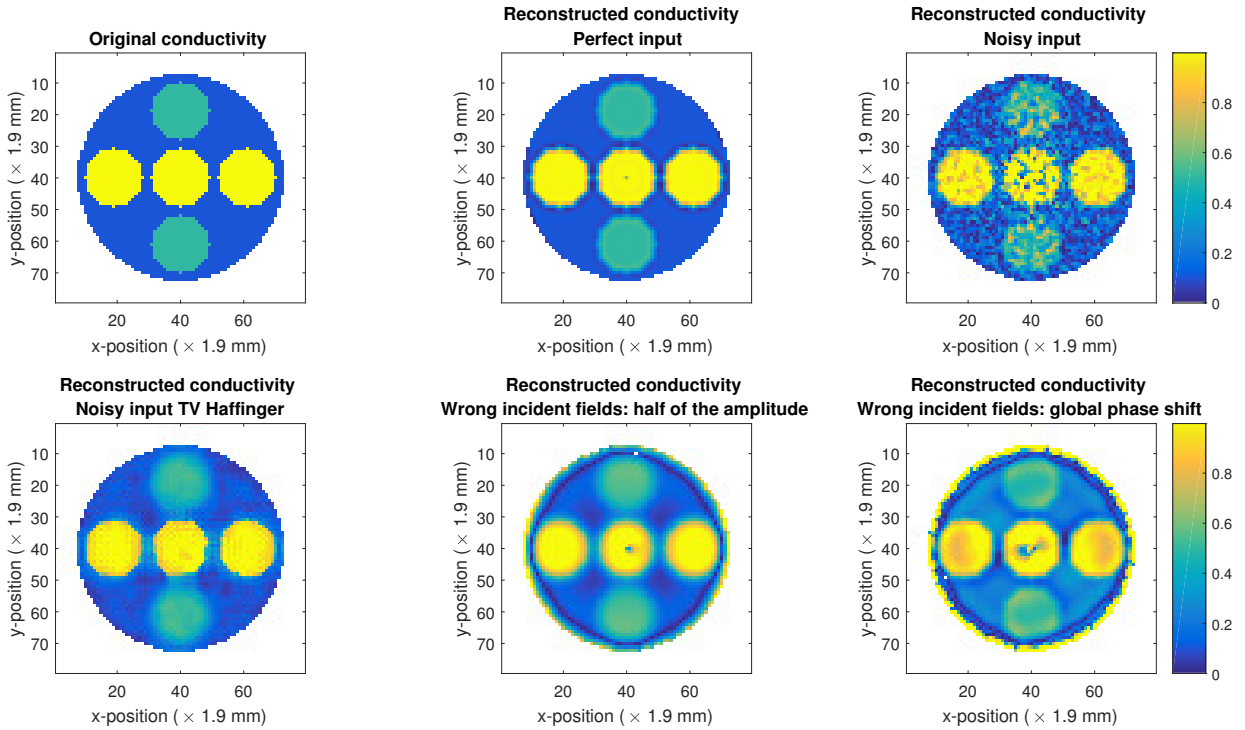

Figure A.1: Conductivity profiles of the complicated phantom. In the top row are from left to right the original profile,the reconstruction with perfect input and the noisy reconstruction. In the bottom row are the TV regularized noisy reconstruction and two reconstruction with the wrong incident fields.

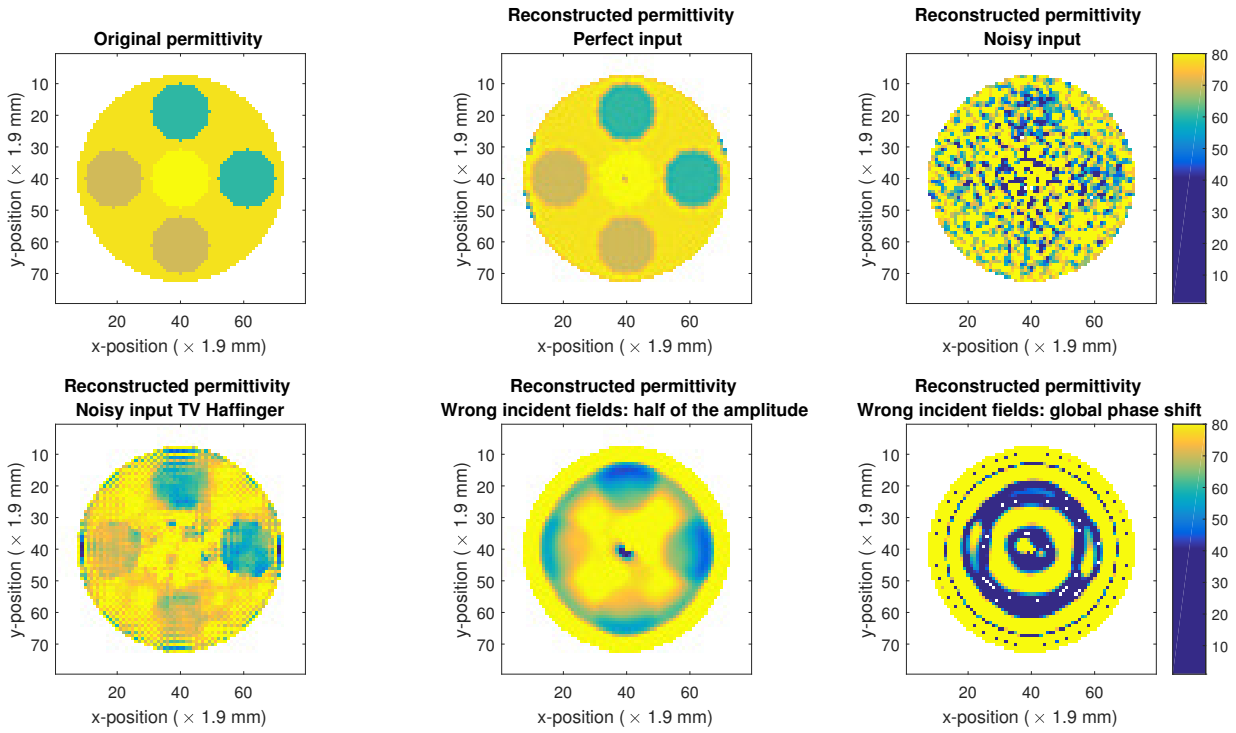

Figure A.2: Permittivity profiles of the complicated phantom. In the top row are from left to right the original profile,the reconstruction with perfect input and the noisy reconstruction. In the bottom row are the TV regularized noisy reconstruction and two reconstruction with the wrong incident fields.

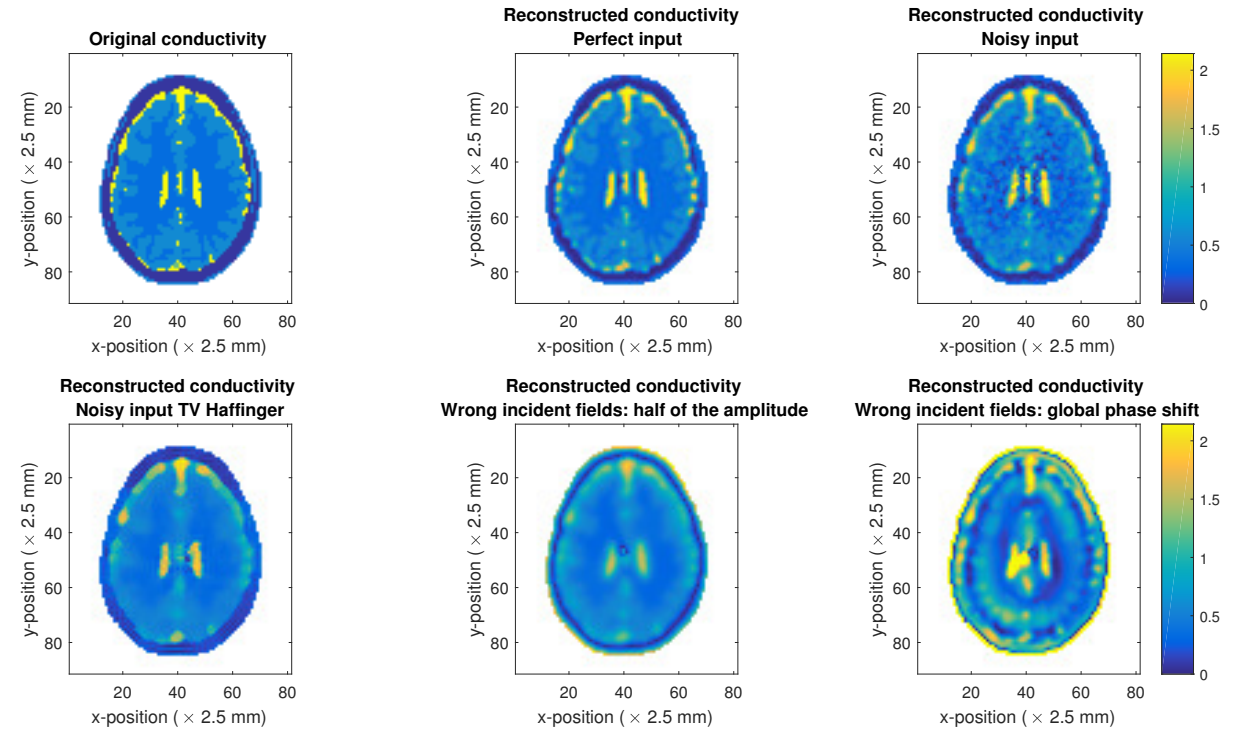

Figure A.3: Conductivity profiles of Ella's brain slice. In the top row are from left to right the original profile,the reconstruction with perfect input and the noisy reconstruction. In the bottom row are the TV regularized noisy reconstruction and two reconstruction with the wrong incident fields.

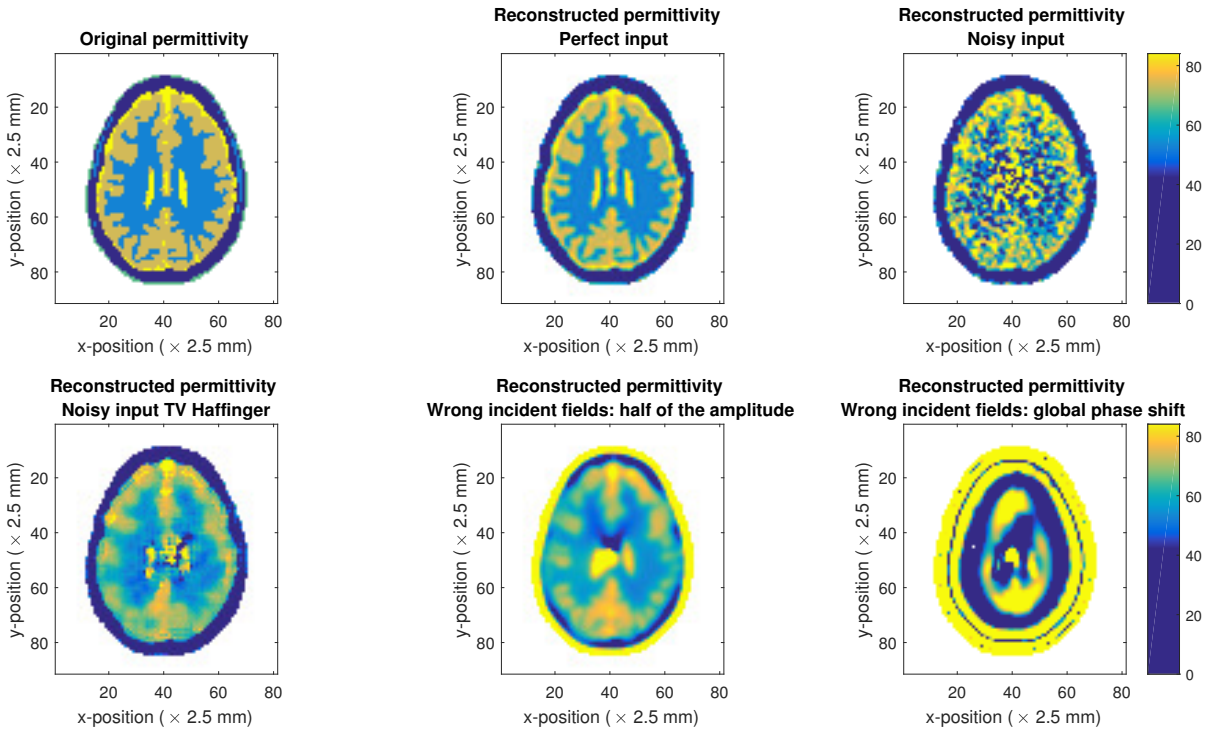

Figure A.4: Permittivity profiles of Ella's brain slice. In the top row are from left to right the original profile,the reconstruction with perfect input and the noisy reconstruction. In the bottom row are the TV regularized noisy reconstruction and two reconstruction with the wrong incident fields.

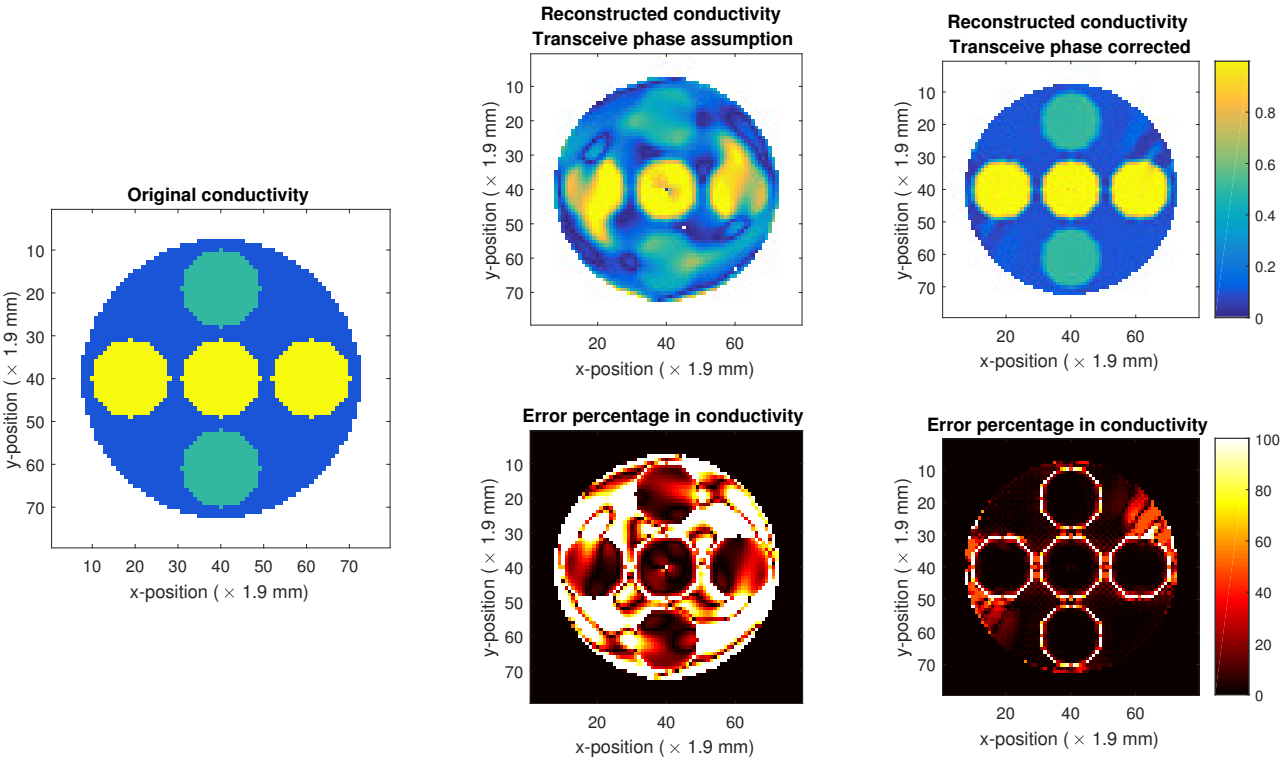

Figure A.5: On the left is the original conductivity. In the top middle figure the reconstructed conductivity is shown by using the TPA, with underneath that the error compared to the original. On the right is the transceive phase corrected reconstructed conductivity, with underneath it the error compared to the original. The static magnetic field strength is 7T.

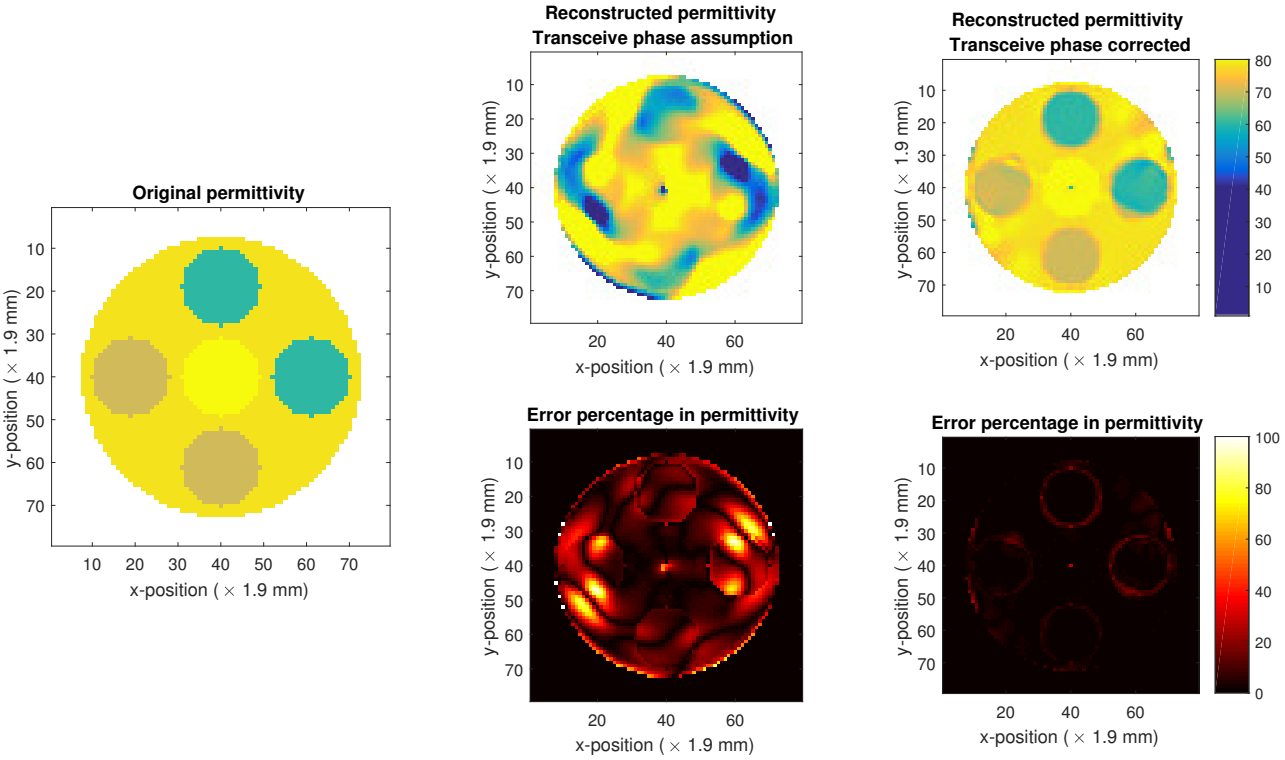

Figure A.6: On the left is the original permittivity. In the top middle figure the reconstructed permittivity is shown by using the TPA, with underneath that the error compared to the original. On the right is the transceive phase corrected reconstructed permittivity, with underneath it the error compared to the original. The static magnetic field strength is 7T.

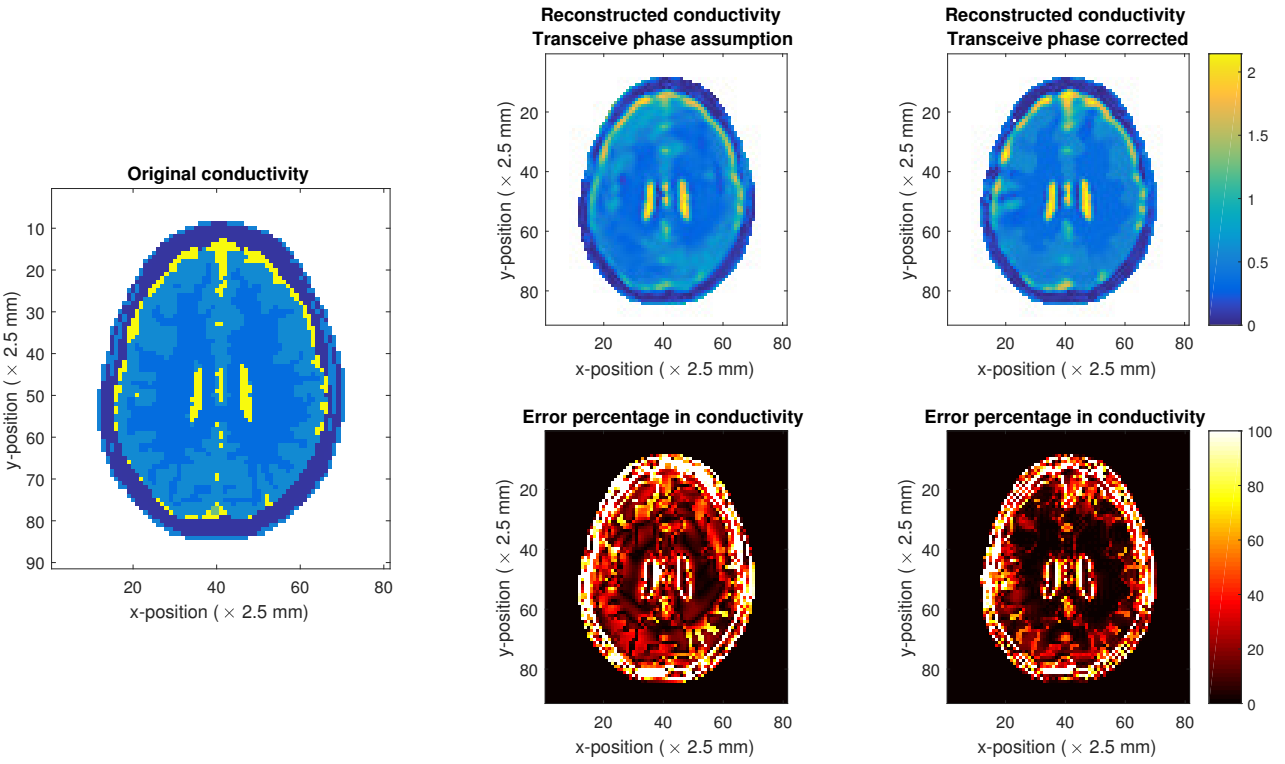

Figure A.7: On the left is the original conductivity. In the top middle figure the reconstructed conductivity is shown by using the TPA, with underneath that the error compared to the original. On the right is the transceive phase corrected reconstructed conductivity, with underneath it the error compared to the original. The static magnetic field strength is 7T.

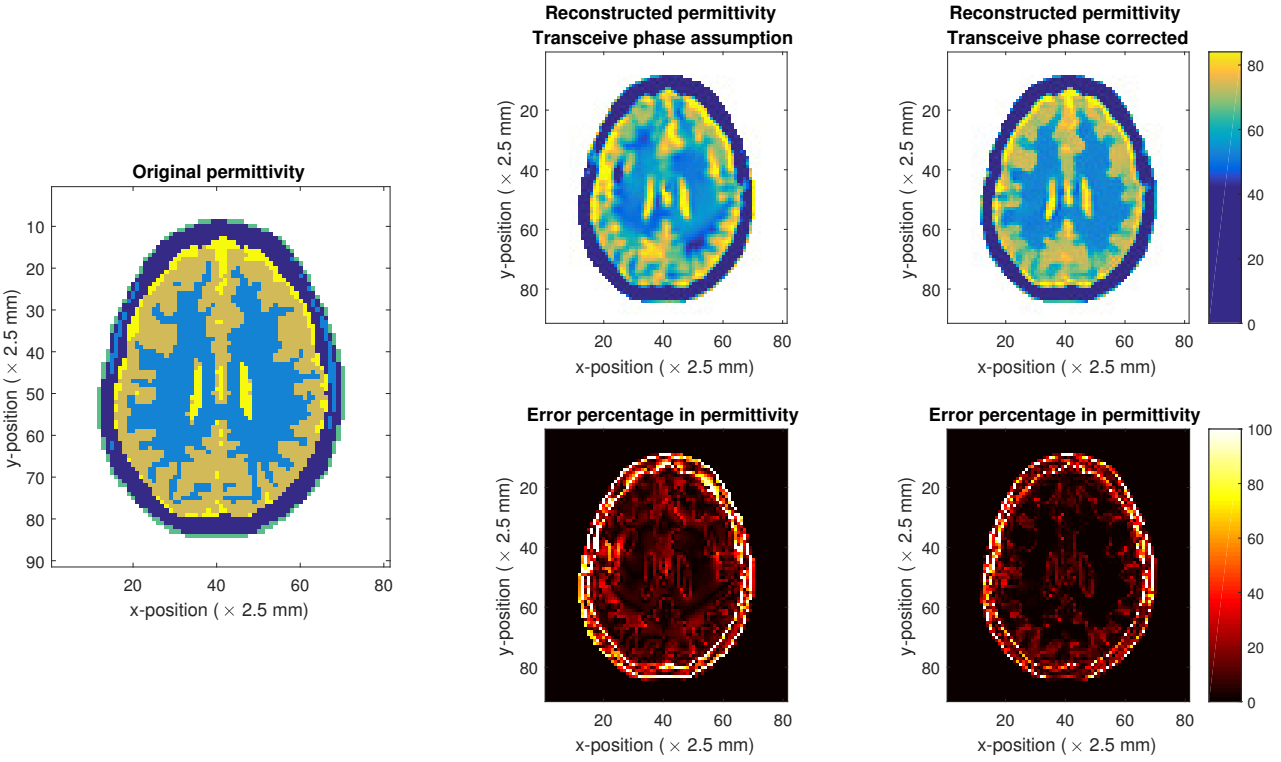

Figure A.8: On the left is the original permittivity. In the top middle figure the reconstructed permittivity is shown by using the TPA, with underneath that the error compared to the original. On the right is the transceive phase corrected reconstructed permittivity, with underneath it the error compared to the original. The static magnetic field strength is 7T.

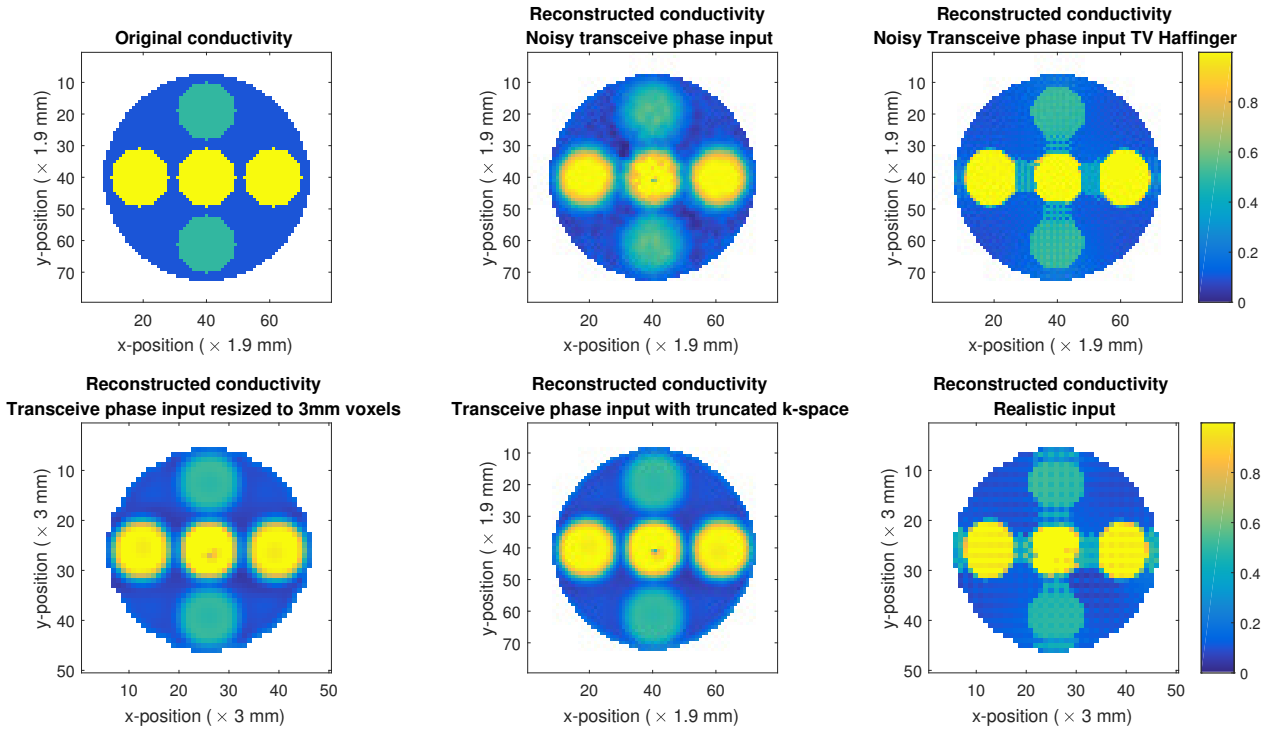

Figure A.9: Conductivity profiles of the complicated phantom, all reconstructed with the transceive phase. In the top row from left to right are the original profile, the noisy input reconstruction and the TV regularized reconstruction. In the bottom row are the rereconstructions with the resized voxels, k-space truncation and the most realistic scenario.

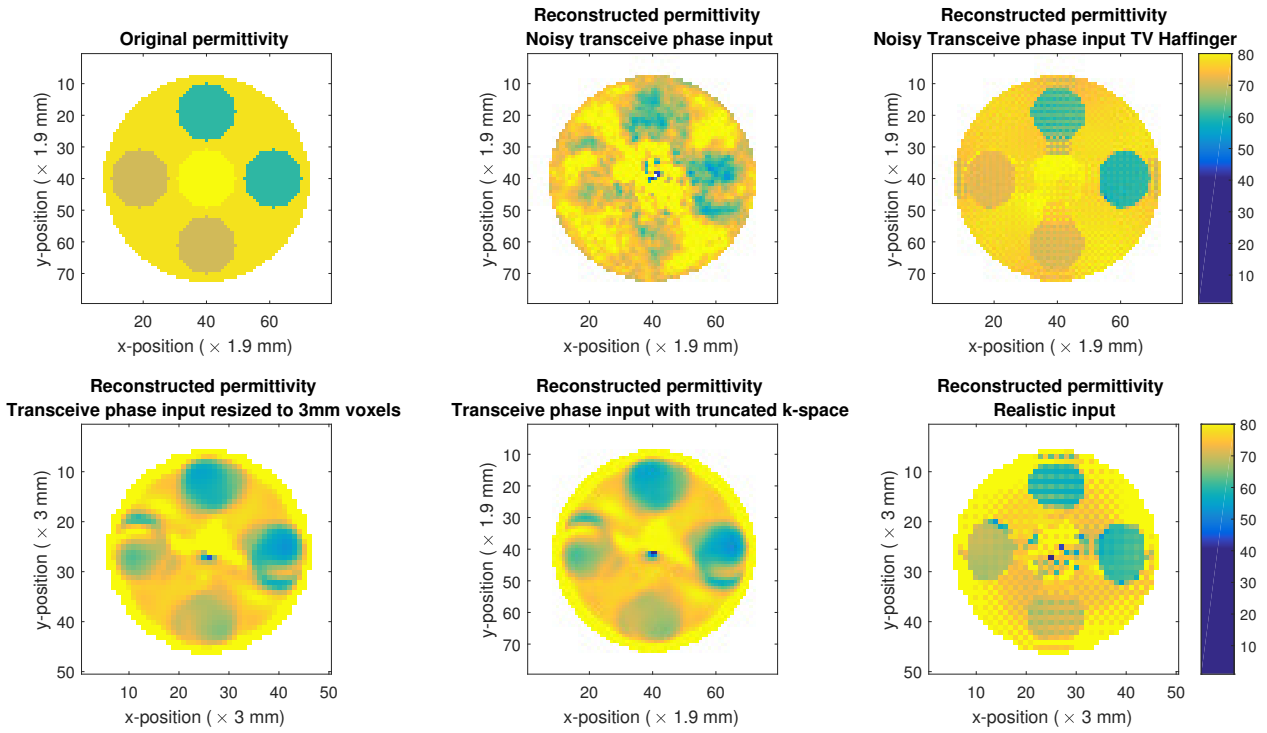

Figure A.10: Permittivity profiles of the complicated phantom, all reconstructed with the transceive phase. In the top row from left to right are the original profile, the noisy input reconstruction and the TV regularized reconstruction. In the bottom row are the rereconstructions with the resized voxels, k-space truncation and the most realistic scenario.

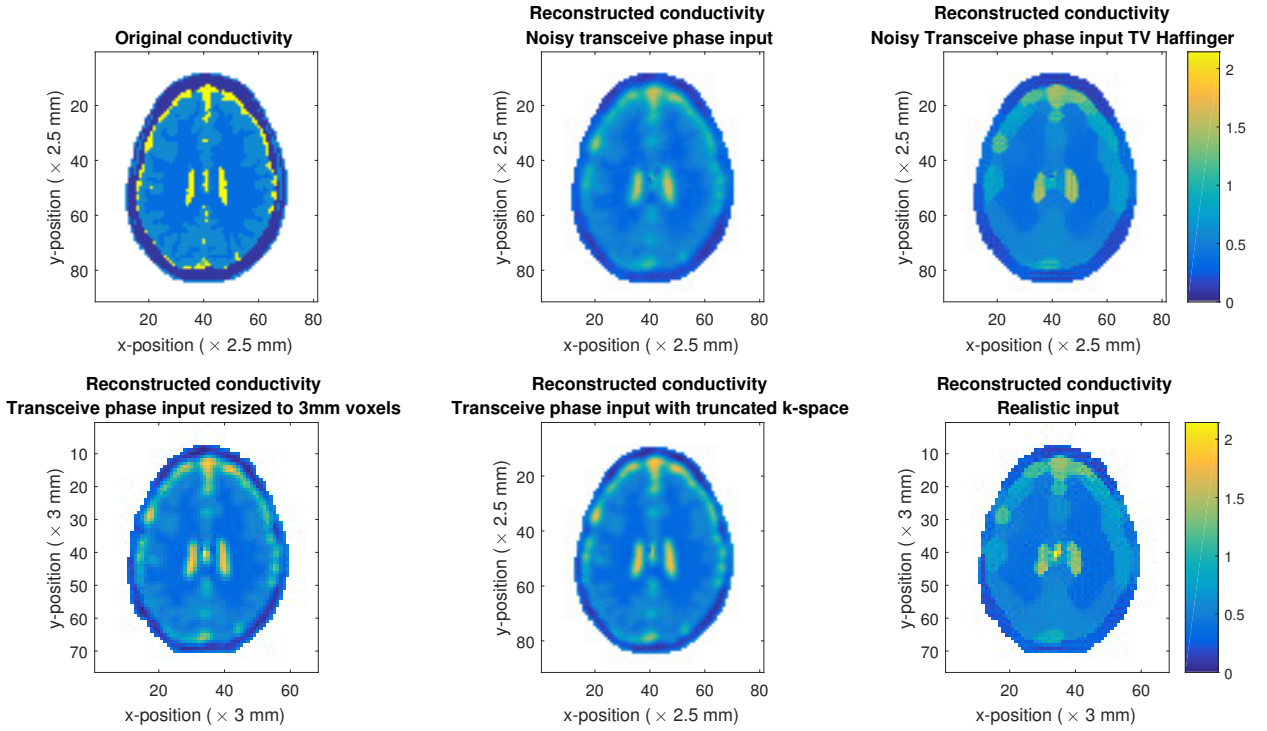

Figure A.11: Conductivity profiles of Ella's brain slice, all reconstructed with the transceive phase. In the top row from left to right are the original profile, the noisy input reconstruction and the TV regularized reconstruction. In the bottom row are the rereconstructions with the resized voxels, k-space truncation and the most realistic scenario.

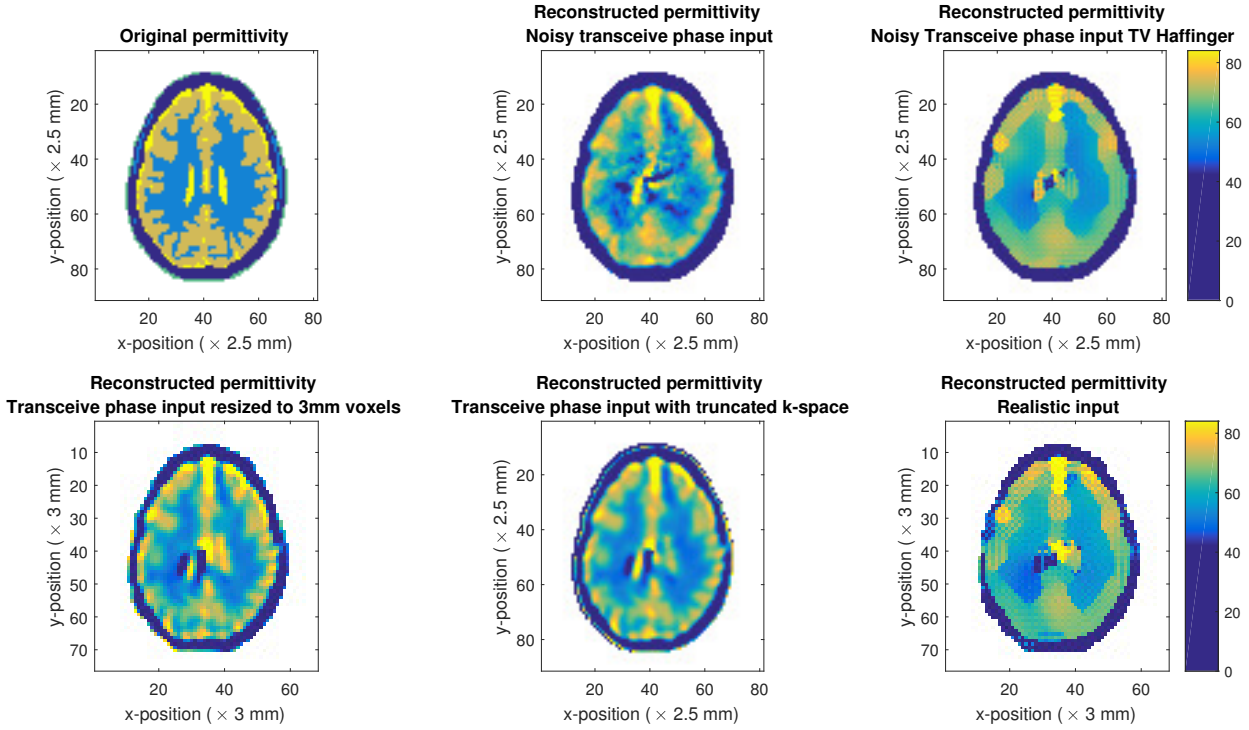

Figure A.12: Permittivity profiles of Ella's brain slice, all reconstructed with the transceive phase. In the top row from left to right are the original profile, the noisy input reconstruction and the TV regularized reconstruction. In the bottom row are the rereconstructions with the resized voxels, k-space truncation and the most realistic scenario.

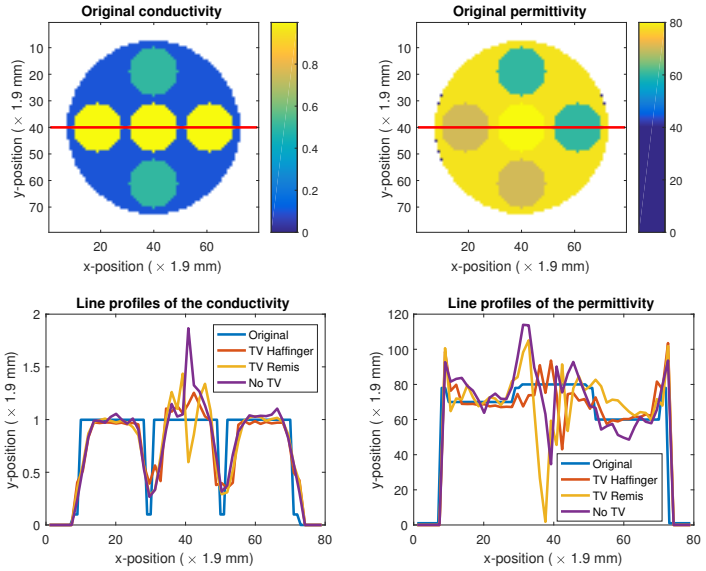

Figure A.13: The line profiles of the complicated phantom. The red line in the original images show where the profile was examined.

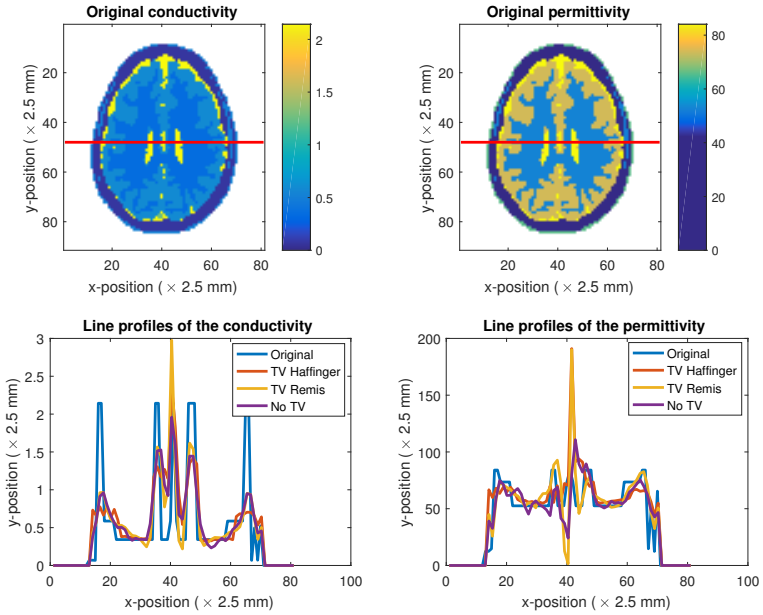

Figure A.14: The line profiles of Ella. The red line in the original images show where the profile was examined.

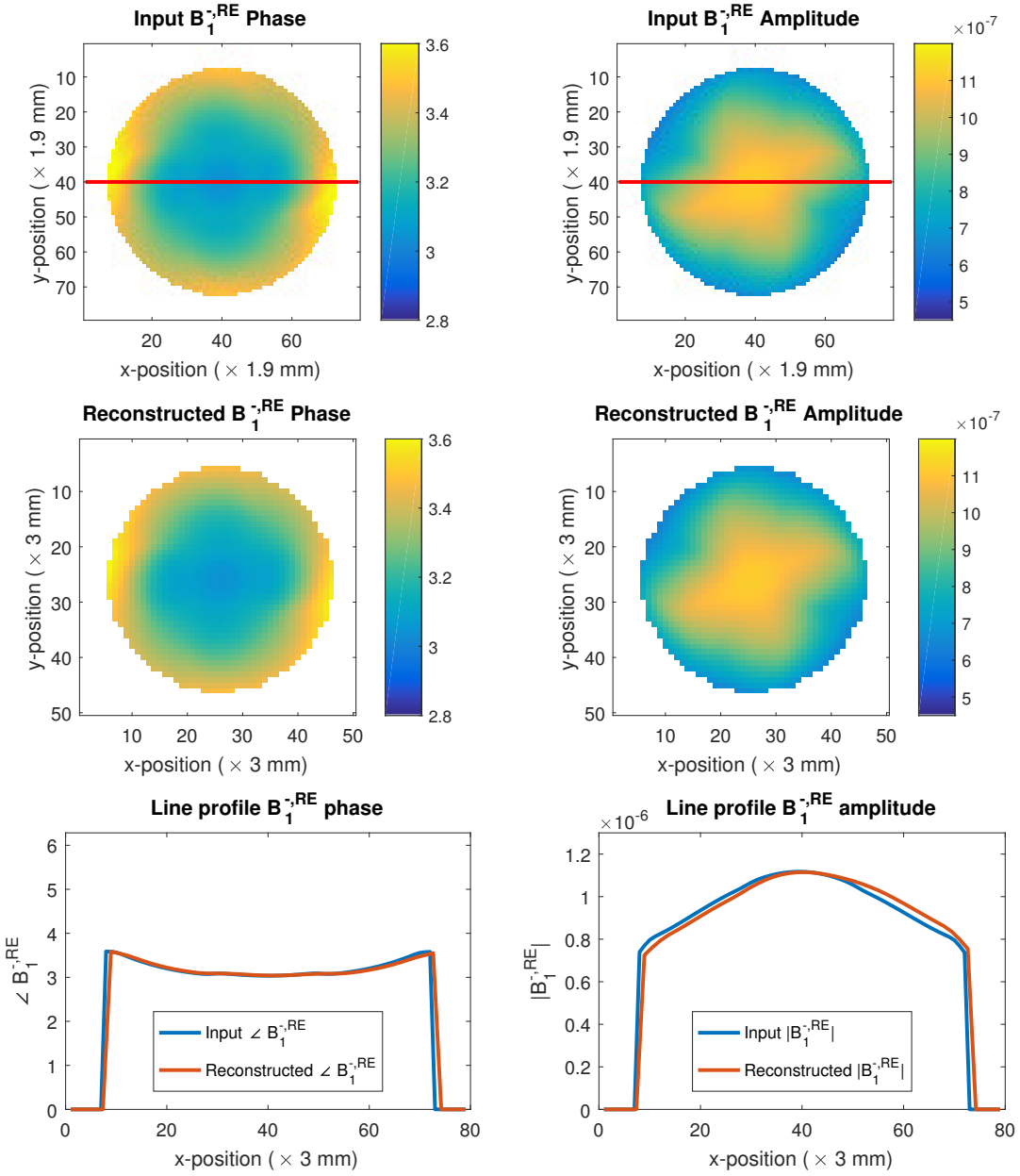

Figure A.15: The $B_1^{-,RE}$ reconstruction for the complicated phantom.

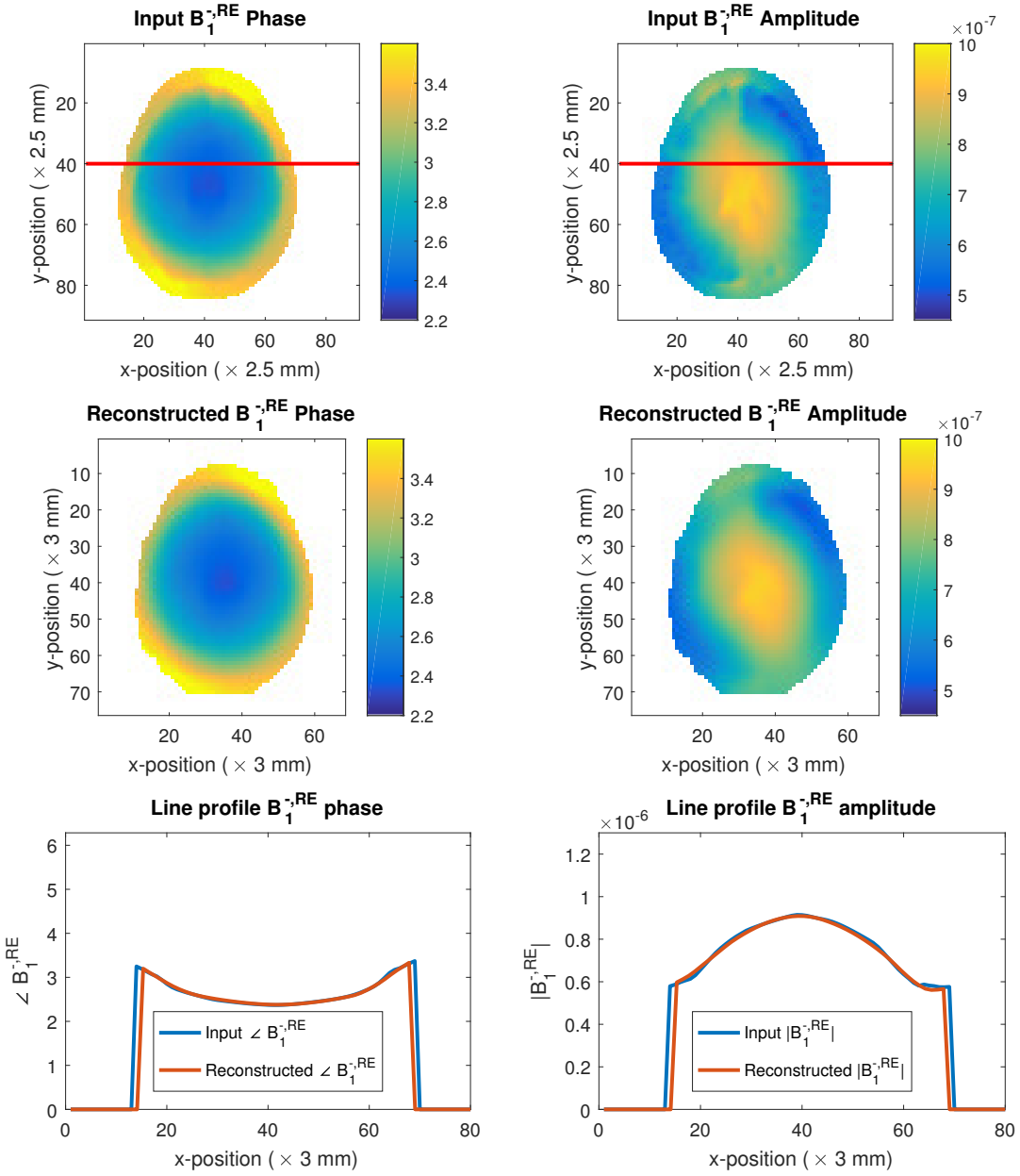

Figure A.16: The $B_1^{-,RE}$ reconstruction for Ella.